NTNU

Norwegian University of
Science and Technology

Corrosion Fatigue of Extruded AA6082 Aluminium Alloy

The effects of Surface Roughness: Machined, Punched, and Counter Trimmed Surfaces

Gaute Tomassen Lindstad

Materials Science and Engineering
Submission date: June 2017
Supervisor: Hans Jørgen Roven, IMA
Co-supervisor: Ola Jensrud, IMA

Norwegian University of Science and Technology
Department of Materials Science and Engineering

Preface

This report is the result of a master`s thesis done at the Department of Materials Science and Engineering at the Norwegian University of Science and Technology (NTNU), during the spring of 2017. The aim of this thesis was to investigate how shaping techniques affect corrosion fatigue properties of a AA6082 aluminium alloy. This thesis is further work on a specialization project executed during the fall of 2016 by the author.

I would like to thank my supervisor, Professor Hans Jørgen Roven, for inspiration and guidance through this master`s thesis work. I would also like to express my gratitude to Pål Christian Skaret for assistance at the MTS laboratory and developing the chamber used in the corrosion fatigue testing. Further I would like to thank Trygve Lindahl Schanche for assistance with topography analysis, and my co-supervisors: Professor II Ola Jensrud and Dr. Ketill Olav Pedersen. Final thanks go to Lars Lodgaard and Benteler for supplying the material used and much appreciated guidance.

I declare that this master`s thesis is done independently and in accordance with the regulations at NTNU.

Trondheim, June 2017

Gaute T. Lindstad

Abstract

The aim of this master's thesis is to investigate the corrosion fatigue properties of an extruded AA6082 alloy. Surface roughness deeply affects fatigue and corrosion fatigue. Surface roughness depends on the shaping process. Three shaping processes have been studied: machining, punching, and counter trimming. Counter trimming is a two-punch process, with the second punch coming from the opposite direction to the first punch. These shaping processes have very different surfaces and surface roughness. Corrosion fatigue tests has been executed with constant amplitude loading, R = 0.1, and with samples submerged in a 5wt% NaCl water solution.

Every sample which were punched or counter trimmed, and tested in saltwater, were optically scanned prior to testing. The topography and surface roughness are therefore thoroughly accounted for. To account for fracture initiation, the minimum of four samples from each process were studied in SEM. Some additional samples tested in air were investigated in SEM as well. Corrosion rates, temperature, and humidity were also accounted for.

The fatigue and corrosion fatigue life ranked as following: Machined > Counter trimmed > Punched. The difference between the processes were reduced when tested in saltwater. Fractography showed that the wounds created during punching and counter trimming were responsible for fracture initiation. For the machined series, the corners between the extruded and machined edge were responsible. The fracture surfaces had clearly visible grain boundaries in SEM. This was attributed to corrosion.

The machined surface showed a far superior surface roughness, with very low Ra, Rt, Rz, and Rv values. Rv proved to be very accurate predicting which side of a sample would have fracture initiation. Topography also showed that the punching parameters used for the samples tested in this thesis were not ideal. Using the difference in corrosion rates between the different surfaces, the increase in surface area due to punching and counter trimming was determined. Compared to the machined surface, the punched and counter trimmed surface had an increase of surface area equal to a factor of 2.55 and 2.41, respectively.

Sammendrag

Utmatting og korrosjonsutmatting blir sterkt påvirket av overflateruhet. Målet med denne diplomoppgaven har vært å studere korrosjonsutmatting-egenskapene til en ekstrudert AA6082 legering. Effekten på overflateruheten fra tre formingsteknikker har blitt studert. Disse teknikkene er: Maskinering, stansing og dobbelstansing. Dobbelstansing består av å stanse en gang, så snu materialet, og stanse en gang til. Metodene gir veldig forskjellige overflater. Korrosjonsutmatting-testingen ble gjort med konstant last-amplitude, R = 0.1, og med prøvene neddykket i saltvann (5wt% NaCl).

Før testing i saltvann ble alle de stansede og dobbelstansede prøvene skannet med en optiskskanner. Noen maskinerte prøver var skannet for å lage overflateruhet gjennomsnitt. Overflateruheten og topografien til prøvene har derfor blitt nøyde vurdert. SEM ble brukt for å finne bruddinitiering. Minimum fire prøver fra hver prosess ble studert. Noen ekstra prøver som ble testet i luft ble også studert i SEM. Korrosjonshastigheten, temperaturen og fuktigheten under testing, ble også vurdert.

Levetiden i både utmatting og korrosjonsutmatting rangerer som følgende: Maskinert > Dobbelstanset > Stanset. Forskjellen i levetid imellom prosessene minsket når man testet i saltvann. Fraktografi analysen viste at sårene lagd under stansing initierte tretthetsbruddene. For de maskinerte prøvene, var det hjørnet imellom den ekstruderte overflaten og den maskinerte kanten som initierte brudd. Fraktografien viste også at korngrensene hadde blitt korrodert til en så høy grad at de var klart synlig i SEM.

Overflateruheten til de maskinerte prøvene var langt bedre enn de stanset og dobbelstanset prøvene. De maskinerte prøvene hadde veldig lave Ra, Rt, Rz og Rv verdier. Rv, som er et mål på dypeste dal, viste seg å være svært nøyaktig i å forutse siden som ville ha bruddinitiering. Topografianalysen viste også at stanseparameterne brukt på prøvene testet i denne diplomoppgaven ikke var optimale. Forskjellen i korrosjonshastigheten imellom de tre typene, ble brukt til å regne ut hvor mye ekstra overflate areal som ble lagd på grunn av stansing og dobbelstansing. Sammenlignet med den maskinerte overflaten, økte stansing overflaten med en faktor på 2.55 og dobbelstansing med en faktor på 2.41.

Table of Contents

1. Introduction

Because of its unpredictable nature, fatigue fracture and failure can result in severe damage. Be it related to health or economy. Fatigue studies has been conducted for more than 150years and is still being studied because of its massive impact on the industry [1]. Studies from the 1990s revealed that fracture costs were equal to 4% of the GNP (Gross National Product) in both the USA and Europe. In eighty percent of these cases, fatigue was involved [2].

Corrosive environments amplify the rate at which fatigue fracture occur. First in 1971 was an international conference held to review this type of fatigue [3]. There are many environments which feature a corrosive environment. Any type of structure close to the sea, or cars driving on a salted road during the winter, are exposed to corrosive environments.

In many industries, and especially the car-industry, the use of aluminium has increased greatly in recent history. From 1995 until 2007, the use of aluminium in cars increased by 23%. This is mainly to fulfill the desire of reducing CO2 emission through weight reduction [4]. As aluminium can be used in almost any part of a car, the necessity to study the fatigue and corrosion fatigue properties of aluminium alloys used in for example suspensions are evident.

Stamping is a very efficient and well established shape process used in automotive industry [5]. Punching, which is a type of stamping, usually creates a surface with a smooth zone and a rough zone [5, 6]. As surface roughness impacts fatigue life [7, 8], it is important to study the fatigue behavior of a punched surface, especially if it is to be used in an automotive industry.

2. Theory

2.1 Aluminium

Aluminium (Al) has a density of 2.7g/mm^3 (1/3 the density of steel) placing it in the light metal category [9]. The weight reduction advantage and good corrosion resistance, make aluminium a suitable construction material. Production of one kilogram aluminium consumes 45kWh electricity and release 12kg CO_2. Recycling aluminium only requires 5% of that energy and releases only 5% of the CO_2 [4]. The energy spent producing aluminium is therefore not considered lost, but rather saved inside the material. Aluminium wrought alloys are divided into eight series. The first number indicating the primary alloying element, and the three next digits signifying the specific alloy. This study is only concerned with the 6xxx-series.

2.1.1 The 6xxx-series

The 6000-series have magnesium(Mg) and silicon(Si) as its primary alloying elements [8]. The 6082-alloy has a composition of 0.6-1.2Wt% Mg and 0.7-1.3Wt% Si [10]. Other common alloying elements for the 6000-series are: Manganese, chromium and cobber [11]. The 6xxx-series is a heat treatable alloy [12], meaning it can achieve greater strength through a controlled heat treatment. It is widely used in the automotive industry because of its combination of strength and good formability [8, 12].

2.2 Hardening of the 6xxx-series

As the 6xxx-series is a heat treatable alloy, it can have greatly increased strength through controlled heat treatments [12]. The complete heat treatment process is shown in Figure 1.

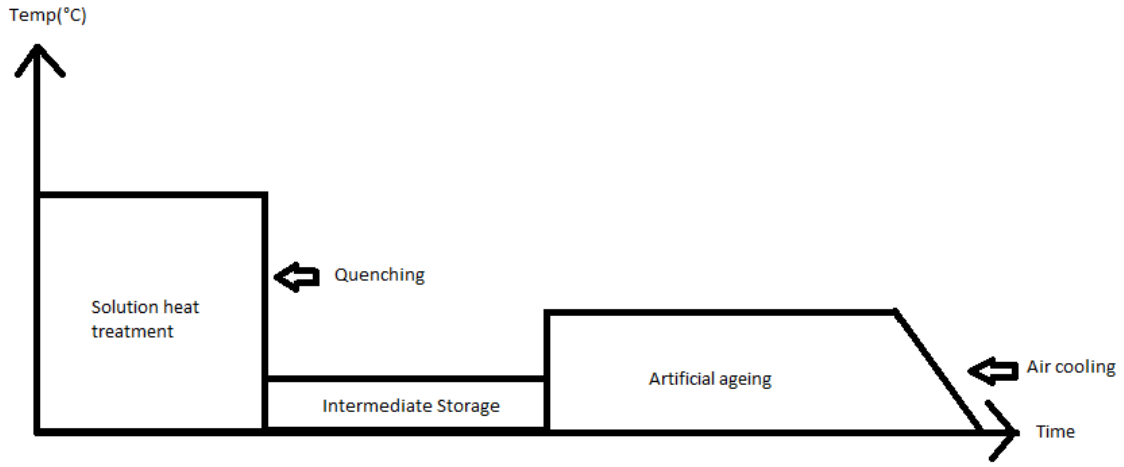

Figure 1: A general illustration of the heat treatment of an aluminium 6xxx alloy. Y-axis showing temperature, X-axis showing time.

It is common to first perform a solution heat treatment. With this initial heat treatment, you aim to create a single phase solid solution with all the solute atoms. This is done by raising the temperature to a relatively high temperature (e.g. 500-550°C) and letting all the atoms settle in the desired phase. In the case of aluminium it is the α-phase. It is important to leave the material at the elevated temperature sufficiently long to achieve a homogenous single phase. This is followed by quenching to create a super saturated solid solution (ssss) [9]. This is

illustrated in Figure 2, where the material with concentration C_0 is raised to the temperature T_1. When a homogenous single α-phase is achieved, it is quenched to T_0.

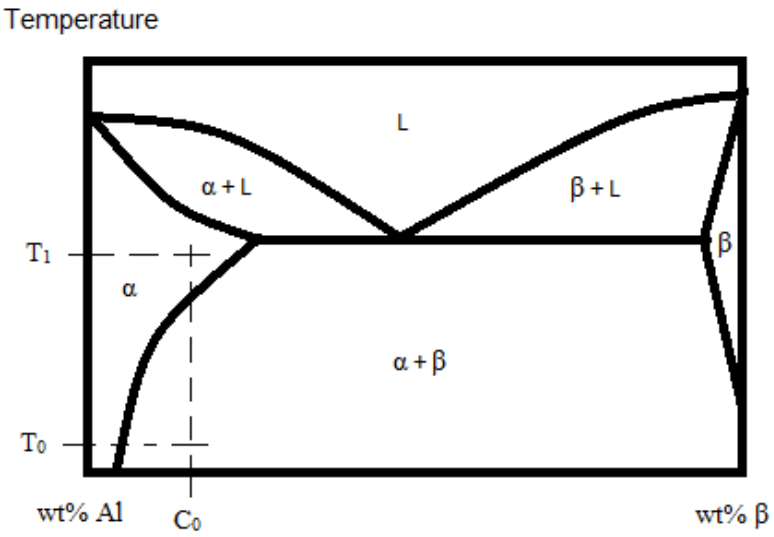

Figure 2: Hypothetical phase diagram for aluminium, illustrating the solution heat treatment of material with concentration C_0. The α and β signifies two different solid phases, and L signifies a liquid phase. Adapted from [9].

The following heat treatment consists of heating the material to an intermediate temperature (e.g. 140-185°C) and keeping it there for a given time. This will prompt the creation of small precipitates inside the original phase. Size and composition of these particles will be a function of temperature and time. This is either referred to as artificial hardening (AA) or precipitation hardening [9]. It is also possible to perform this procedure at room temperature, but the process would take too long for industrial applications. Aging at room temperature is called *natural aging*. Figure 3 shows an illustration of how hardness varies with time.

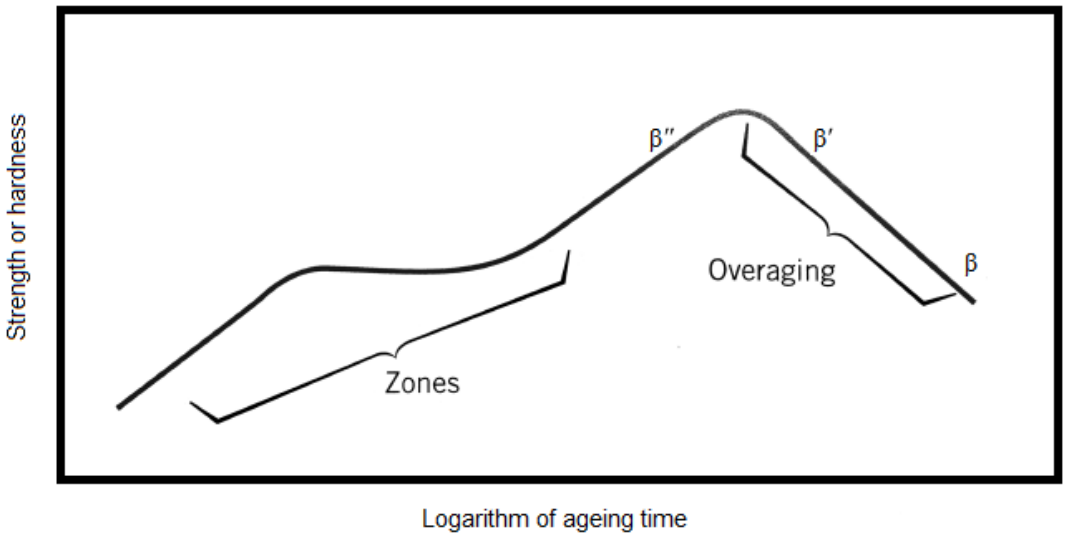

Figure 3: Schematic diagram showing strength and hardness as a function of the logarithm of aging time, at a given temperature. Zones referring to Guinier-preston zones and overaging showing the decrease in strength due to too long aging. Adapted from [9].

During artificial aging, the AA6082 alloy goes through these steps (illustrated in Figure 3):

Over saturated α-phase → GP1 → β'' → β'(Mg_2Si) → β(Mg_2Si) [11].

-GP1: Guinier-preston zones; possible spheres of Mg and Si.

-B'': Monocline and partly coherent needle shaped in the <100>-direction.

-B': Mg2Si which is hexagonal and partly coherent rods.

-B: Mg2Si which is cubical and is shaped as incoherent squared plates.

After artificial aging, it is possible to achieve a yield strength of (Rp_{02}) 190-360MPa, ultimate tensile strength (UTS/R_m) of 220-390MPa and an elongation in heated state of 12-17%. At peak hardness, you have a combination of β'' and β'. The combination of being easily extruded, having good strength, good corrosion resistance, and good fatigue properties has made it a widely used Al-alloy [11]. It is possible to leave the material at the elevated temperature for too long. This leads to what is called *overaging.* Overaging reduces material hardness as shown in Figure 3.

2.2.1 Temper states

A designation system exists to describe the state of aged materials. Temper states are very common for describing aluminium. Temper-state designations for aluminium are described in Table 1. The most relevant temper state is T6.

Table 1: Table showing the temper states of aluminium, inspired by [13].

Temper state	Description
T1	Cooled from an elevated temperature-shaping treatment and naturally aged.
T2	Cooled from an elevated temperature-shaping process, cold worked, and naturally aged.
T3	Solution heat treated, cold worked, and naturally aged.
T4	Solution heat treated and naturally aged.
T5	Cooled from an elevated temperature-shaping process and artificially aged to peak hardness.
T6	Solution heat treated and artificially aged to peak hardness.
T7	Solution heat treated and overaged or stabilized.
T8	Solution heat treated, cold worked, and artificially aged.
T9	Solution heat treated, artificially aged, and cold worked.

2.2.2 Intermediate storage of the 6xxx-series

Intermediate storage is the time in between the solution heat treatment and the artificial aging. A significant portion of the AlMgSi-alloy strength comes from the precipitation hardening. Studies show that if AlMgSi-alloys are allowed to undergo natural aging before artificial aging, they will form clusters of Mg and Si atoms. These clusters have shown to inhibit the formation of β''-precipitates [12], thus slowing down the overall hardening kinetics. A 60-minute intermediate storage time can lead to a drop of 50MPa in yield strength [12]. However, natural aging has proven to be superior to artificial aging when it comes to fatigue properties. In a study done by Marte Brynjulfsen at NTNU on the AA6082 alloy, the T6-state ended up having the poorest fatigue properties even though it had the best ultimate tensile

strength. The study showed that the T4-state had the best fatigue properties. This improvement in fatigue properties was attributed to superior ability to be work hardened (GP-zones were superior to β`` and β) [14].

2.3 Fatigue

Fatigue is failure in material due to cyclic stress. This differs from a regular fracture, because the stresses applied can be far below the yield strength. It is important to distinguish between high-cycle and low-cycle fatigue. Low-cycle fatigue involves a significant portion of plastic deformation, and fracture occurs after a relatively low number of cycles. In high-cycle fatigue however, the fracture tend to be much more instant and unexpected [15], and occurs after a relatively high number of cycles. Fatigue is generally considered a three-step process. First step is crack initiation or nucleation. Second step is fatigue crack propagation. The last step is overload failure. The steps are illustrated in Figure 4. This will be explained in more detail in section 2.6.3 Fatigue fracture.

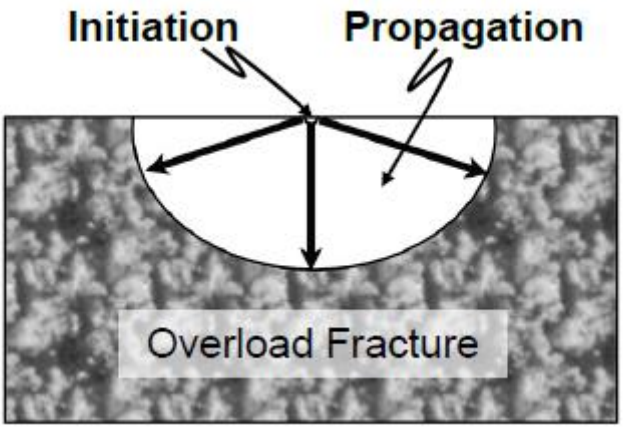

Figure 4: Shows the steps of fatigue failure. It begins at the initiation point and propagates until it experiences overload failure. Taken from [8].

Figure 5 is an illustration of why fatigue occurs. A collection of grains with different orientation (with regard to the slip plane) are presented. The middle grain, marked A, has an orientation that is parallel to maximum shear stress. When exposed to a sufficiently large cyclic load, this grain will experience plastic deformation, or slip as it is also called. The other grains with less tension due to their orientation, may only experience elastic deformation. The grain marked A will therefore be pushing on the surrounding grains. Even though it is only a weak push leading to a slight disorder of the surrounding grains, it will add up over time. After a sufficient number of cycles, the rest of the grains will experience plastic deformation as well [15].

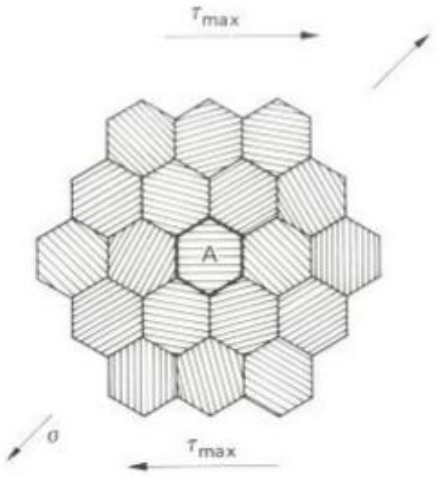

Figure 5: Showing a crystal with different orientated slip planes.τ_{max} and σ signify maximum shear stress direction and tension direction, respectively. The middle grain, marked A, has its slip planes parallel with the maximum shear stress. Taken from [15].

In Figure 6(a), σ_2 signifies the yield strength of grain A which is clearly lower than the yield strength for the whole collection of grains σ_1. Figure 6(b) shows the cyclic load of A, and how it behaves with both plastic- and elastic-deformation during the cyclic loads.

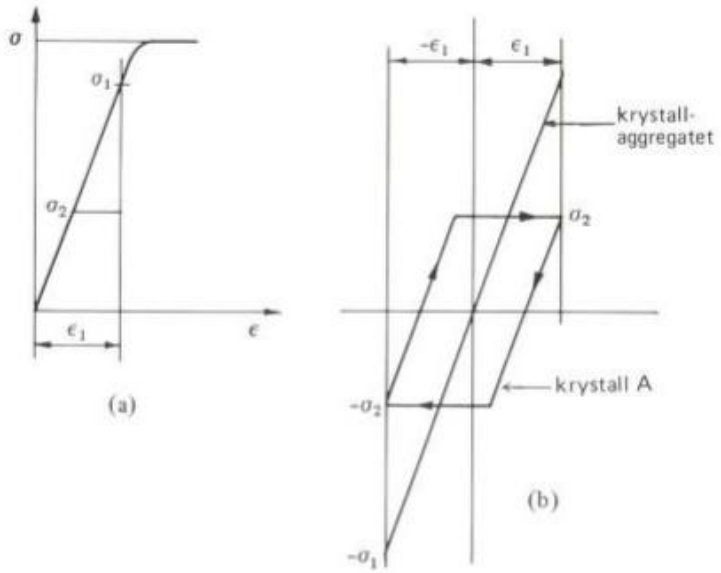

Figure 6: (a) Shows how the collection of grains in Figure 5 as a group have yield strength of σ_1, but grain A have a lower yield strength equal to σ_2. (b) Shows how the deformation changes when the load changes from positive to negative, and how A has both an elastic and plastic component. Taken from [15].

2.3.1 Analyzing fatigue

There are three main analyzing paths of fatigue [2].

Stress-based approach: Based on the effective (accounting for grooves, holes etc.) average stress that the relevant area is exposed to. Considered as the traditional way of studying fatigue [2].

Strain-based approach: Uses a more detailed understanding of local yielding in the material whilst undergoing a cyclic load.

Fracture mechanics approach: Uses fracture mechanics theory to explain the crack growth.

The stress-based approach will be used in this study, in the form of a S-N curve. The last approach mentioned, was also used in the form of fractography to locate fracture initiation sites. Both will be explained in more detail in the following sections.

2.3.2 Cyclic loading and basic definitions

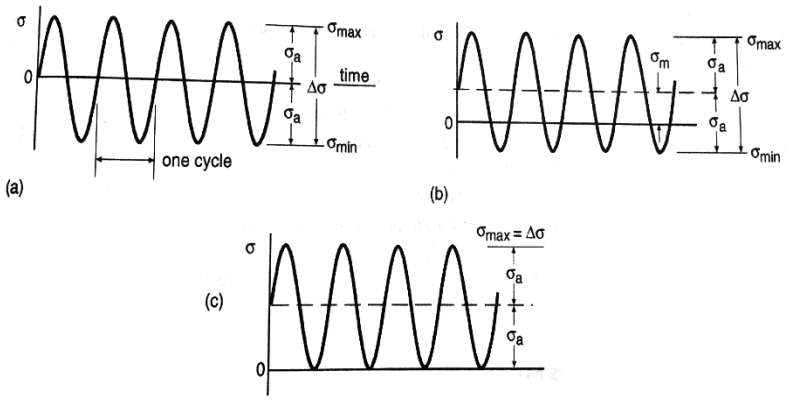

Figure 7: Constant amplitude cyclic loading with different mean stresses. Y-axis signifies the stress (σ) and X-axis time. Δσ, σ_{max}, σ_{min} and σ_a are stress range, maximum stress, minimum stress, and stress amplitude, respectively. (a) shows σ_m = 0, (b) has a nonzero mean stress σ_m and (c) has σ_{min}= 0. Taken from [2].

Stress range: $$\Delta\sigma = \sigma_{max} - \sigma_{min} \quad (1)$$

Mean stress: $$\sigma_m = \frac{\sigma_{max} + \sigma_{min}}{2} \quad (2)$$

Stress amplitude: $$\sigma_a = \frac{\Delta\sigma}{2} \quad (3)$$

Maximum stress: $$\sigma_{max} = \sigma_m + \sigma_a \quad (4)$$

Minimum stress: $$\sigma_{min} = \sigma_m - \sigma_a \quad (5)$$

Stress ratio: $$R = \frac{\sigma_{min}}{\sigma_{max}} \quad (6)$$

Amplitude ratio: $$A = \frac{\sigma_a}{\sigma_m} \quad (7)$$

Figure 7 show how the equations above relate. Using equation 6, the stress ratio *R*, is equal to -1 when $\sigma_{min} = -\sigma_{max}$ (Figure 7(a)). This is referred to as *completely reversed cycling*. When R = 0 or σ_{min} = 0 (Figure 7(c)) it is referred to as *zero-to-tension cycling [2]*. The mean stress can be zero when the cyclic stress is symmetric around the x-axis. An increase in the stress ratio, causes growth rates to increase [2, 16].

2.3.3 S-N curve

It is important to distinguish between a point stress, σ, and nominal stress, S [2]. Nominal stress is what is commonly used and is defined in equation 8. It can be equal to the point stress in certain instances.

$$S = \frac{P}{A} \tag{8}$$

Where A is the cross-sectional area, and P the force applied. In equation 1-7, σ can be denoted S (both are stresses). It is written with σ because it is conventional to do so.

A material can only survive a certain number of cycles at a given stress amplitude before failure. The number of cycles until failure, N_f, is referred to as a materials fatigue life. In general, higher stress amplitude yield shorter fatigue life. Samples tested in high-cycle fatigue at different stress amplitudes, are used to create a stress-cycle curve (S-N curve). An example of such a curve is shown in Figure 8. It shows a material that has a *fatigue limit*, which is minimum stress amplitude necessary to achieve failure. Below this stress amplitude, N_f should in theory become infinitely large. This is where the graph goes horizontally.

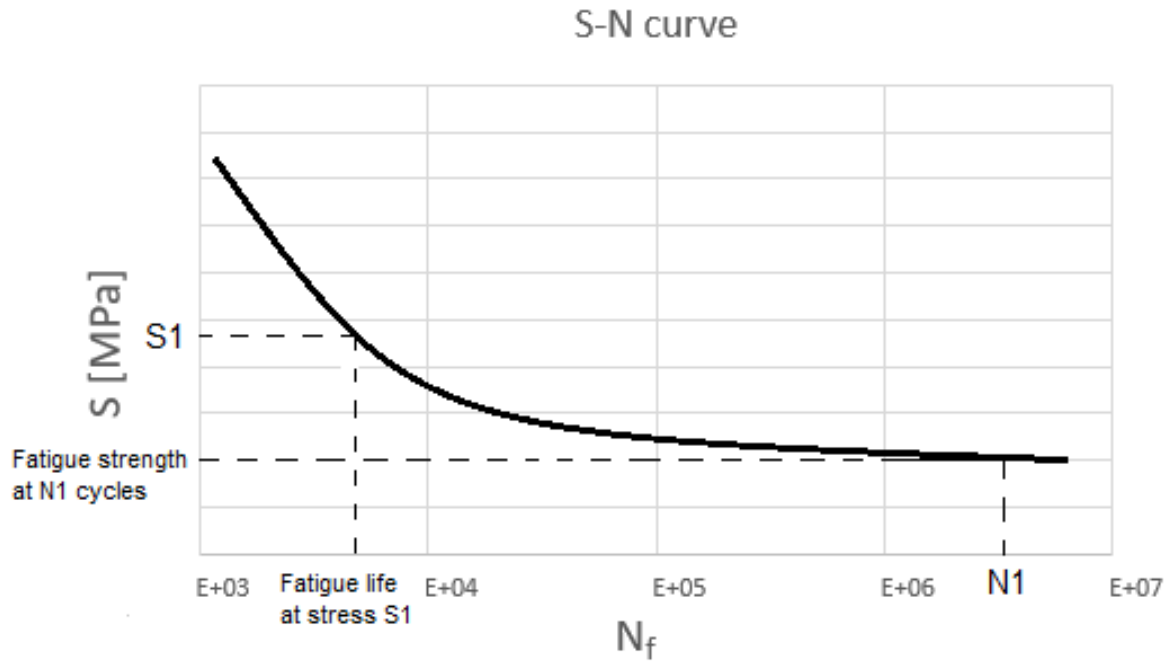

Figure 8: Shows a S-N curve for a non-specific material. S and N_f are stress amplitude and fatigue life, respectively. S1 signifies the stress amplitude or fatigue strength and the connected dashed line leads to the corresponding fatigue life. N1 shows a fatigue life and the connected dashed line leads to the fatigue strength. Made by the author.

2.3.4 Surface roughness effect on fatigue

Surface topography is a crucial factor on fatigue life. Smoother surfaces in general improve resistance against fatigue, suggesting machining is superior to stamping. However, it is possible to introduce residual stresses through machining that have an negative effect on resistance against fatigue [2]. Through methods like electropolishing you can drastically increase fatigue life by smoothing the surface [7]. Surface scratches or similar surface discrepancies, will have locally enhanced stress concentrations, and is therefore likely to become the crack initiation site. It is the *weakest link*, or so to speak. Scratches or defects in

this manner have a greater negative impact on fatigue life if they are orientated perpendicularly to the tension direction. This is because it yields the greatest stress concentration [17], which corresponds well with the theory in the previous section explaining why fatigue happens. Removal of the recrystallized layer surrounding a fibrous core material as the extruded AA6082 samples used in this study, has also proven to greatly improve fatigue life [2].

2.3.5 Smith, Watson, and Topper (SWT) equation

SWT equation is an equation that takes in account the mean stress (eq. 2). This allows for fatigue data tested with, for example, R = -1 to be compared with data tested with R = 0.1. There are several equations developed to account for the mean stress. SWT is frequently employed and is the one used in this study. Eq. 9 shows how Nf can be calculated [2].

$$Nf = \frac{1}{2}\left(\frac{\sigma_{max}}{\sigma`_f} * \sqrt{\frac{1-R}{2}}\right)^{\frac{1}{b}} \tag{9}$$

Here Nf is fatigue life, σ_{max} = max stress, $\sigma`_f$ = material constant, R = stress ratio, b = fatigue strength exponent. How *b* is calculated is shown in Figure 9. It needs a straight trend in a log – log S-N curve to be calculated.

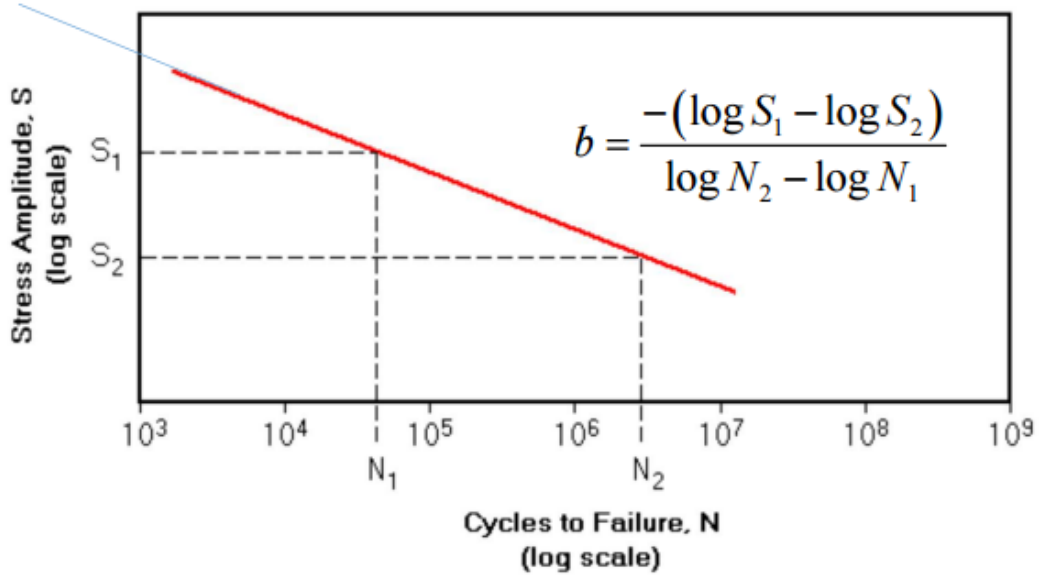

Figure 9: Shows how b – fatigue strength (Basquin) exponent can be calculated from a log-log S-N curve. Taken from lecture notes in subject "TMM4195 - Fatigue design", lectured at NTNU.

2.4 Punching

Punching is a type of stamping-process used to cut or create a hole in a sheet metal [5]. Figure 10 shows the process of punching.

It can be considered a three-stage process. The first step is named “penetration stage”. It is shown in Figure 10(a). Here the punch starts to force its way through the metal. A fracture will start to propagate from the punch, and another crack will propagate from the die. This is illustrated in Figure 11. Optimally these will meet and form a continuous crack. This stage

ends when there is a continuous fracture from the die to the punch. The second stage, shown in Figure 10(b), is named the “fraction stage”. Here the punch has successfully cut out the blank, and the blank is loose from the material. The third stage, shown in Figure 10(c), is the “return stage”. Here the punch is pulled back out. Because the material is in direct contact with the punch, a hold (shown in green, with springs holding it back) must be applied to hold the material from being pulled with the punch. The force necessary to hold the material back in this stage, is significantly lower than the initial punching force. The cut zone denoted *b* is kept to a minimum to avoid unnecessary friction between the die surface and the blank.

It is important to note that this illustration is in 2D. In the real world, the punching can be in the centre of a material, creating a hole, and not two separate plates. Another process that punching is easily confused with is blanking. It is essentially the same process. The distinction is that in punching the piece cut out is waste. While in blanking, the piece cut out is the work [6].

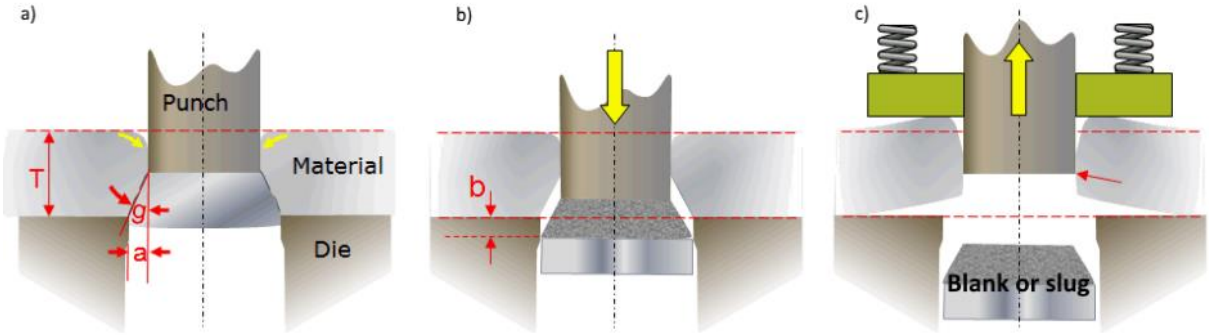

Figure 10: Illustration of the punching process. The punch is the tool used to create the hole, die is the hold holding the material up, blank or slug is the piece of material that is cut loose, T is the material thickness, g is the fracture angle, a is cutting or die clearance and b signifies the length of the cut zone of the die. a) "Penetration stage", from initial contact between punch and material until fracture. b) "Fraction stage", the blank is loose. c) "Return stage", the punch is pulled back out. Adapted from internal document belonging to Benteler.

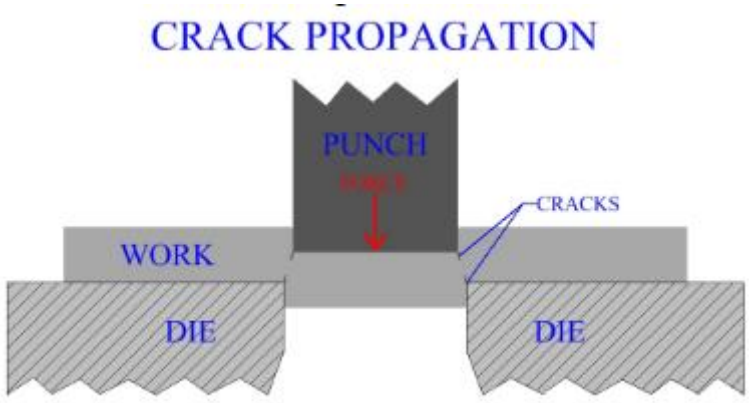

Figure 11: Two cracks propagating. One crack is propagating from the die, and another crack propagates from the punching tool. Work is the material being punched. Taken from [6].

2.4.1 Punched surface

Punching leads to an imperfect surface. Figure 12 shows the cut profile of both the sheet material (work) and the blank. The zones are opposite for the sheet material and the blank. Beginning at the top of the sheet material, you have the *rollover*. In the rollover-zone the material is curved with the punching direction creating a non-sharp edge. Following the rollover-zone is the *burnish zone*. It has a relatively smooth, straight, surface which is why it is often desired to have a long burnish zone Afterwards there is a fracture zone, which has rough surface. In the end, you have a *burr*. A burr is a little piece of material which is sticking out at the end of the material sheet. As mentioned earlier, the blank has the same zones only in the opposite order to the sheet material.

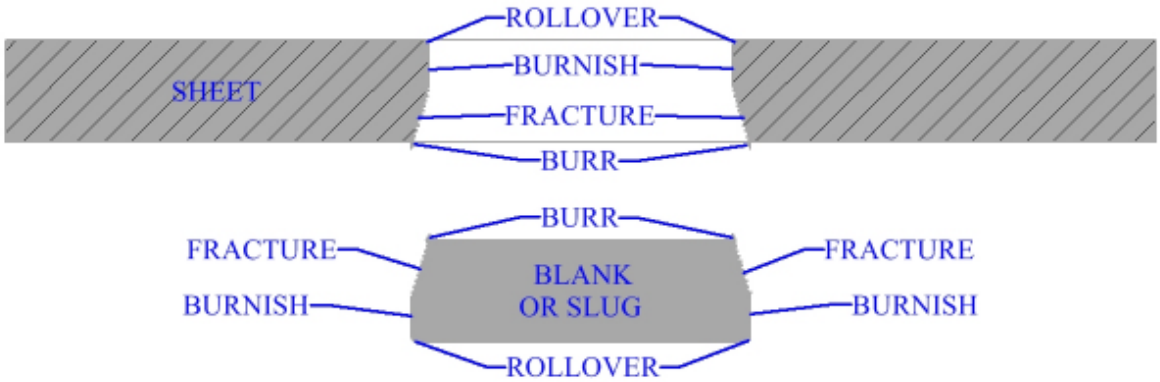

Figure 12: Cut profiles of the hole and the blank. Taken from [6].

2.4.2 Cutting clearance

Cutting clearance is shown in Figure 10, where it is denoted as *a*. It is the gap between the die and the punch. The cutting clearance has a great effect upon the quality of the cut [5, 6]. Different metals and alloys have different optimal parameters for cutting clearance (and other parameters such as punching force etc.).

A too wide clearance can cause the sheet metal to be drawn down into the gap between the die and the punch. This is shown in Figure 13. This can lead to fracture in the part of the material squeezed into the gap, which is rarely the desired cut. If the clearance is too narrow, the cracks propagating from the die and the punch will mismatch. Too narrow clearance is shown in Figure 14. This usually results in secondary shearing and a deformed edge surfaces. Cutting clearance is a function of sheet metal thickness and type of material. It can vary from 1% to 30% of sheet thickness [6].

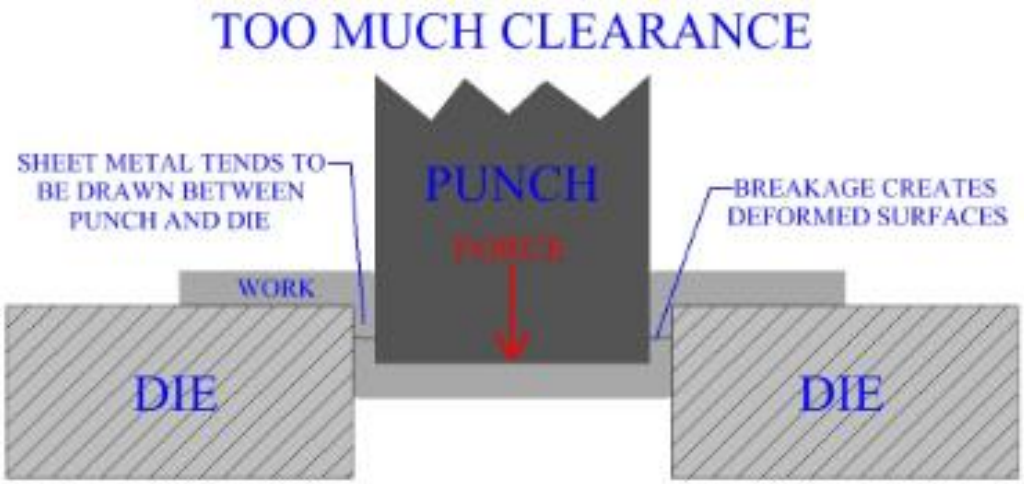

Figure 13: Effect of a too wide cutting clearance. Taken from [6].

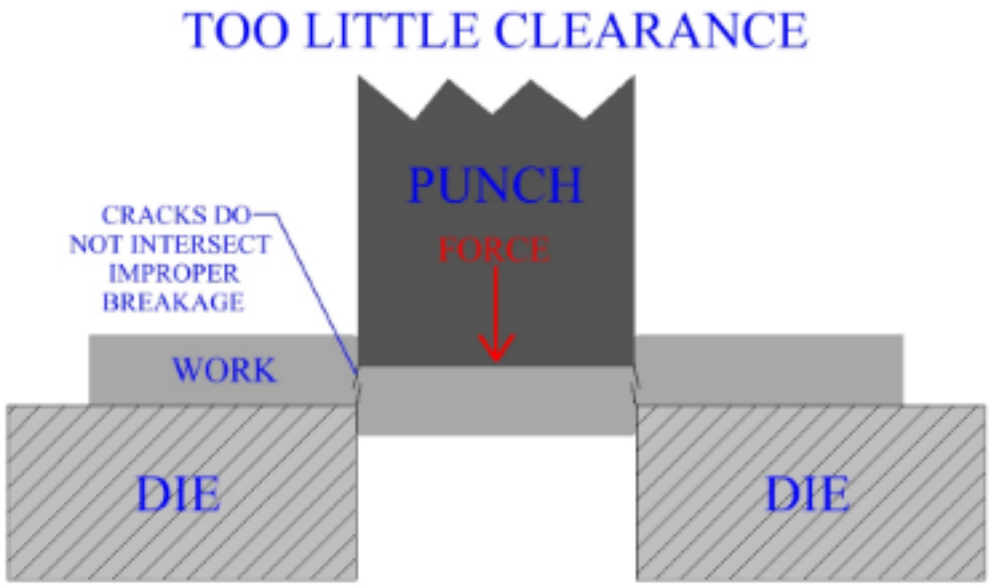

Figure 14: Effect of a too narrow cutting clearance. Taken from [6].

2.5 Scanning electron microscopy (SEM)

SEM is an excellent instrument for characterising material properties, including topography. SEM utilizes an electron beam to “light up” the sample surface. The beam can either be in stationary- or scanning-mode. Stationary mode means that the primary electron beam is stationary, while scanning mode means it is scanning over the surface. When the focused electron beam hits the sample surface, several types of signals are emitted: Secondary electrons, backscattered electrons, x-rays, Auger electrons and photons with varying energy levels. These signals can be interpreted to figure out among other things: chemical composition, crystallography, and topography [18]. SEM has an excellent depth perception, meaning it is a well-suited tool for studying fracture surfaces.

2.6 Fractography

There are several types of fractures; brittle-, ductile- and fatigue-fracture being the main categories. One of the best methods of studying a fracture is, as earlier mentioned, with the

use of SEM [18]. By studying the fracture surface, it is possible to determine what type of fracture has occurred. In this section, the three fracture types mentioned will be presented, with focus on fatigue fracture.

2.6.1 Ductile fracture

A ductile material usually exhibits ductile fractures under normal circumstances. This type of fracture occurs when a material in tension reaches an instability point, where the strain hardening of the material cannot keep up with the loss of cross-sectional area. This is when the infamous “necking” occurs. A ductile fracture is shown in Figure 15.

Ductile fractures are commonly observed in three stages [19].

1. Formation of a free surface at an inclusion or second-phase particle by either interface decohesion or particle cracking.
2. Growth of the void around the particle, by means for plastic strain and hydrostatic stress.
3. Coalescence of the growing void with adjacent voids.

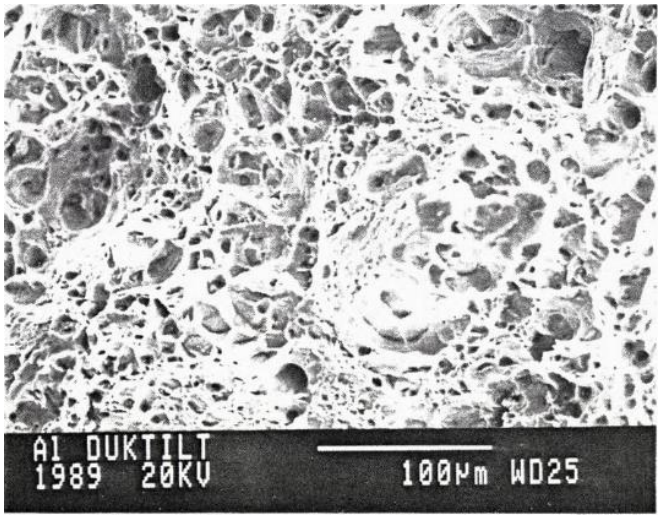

Figure 15: Ductile fracture surface of aluminium. The micrograph is taken in SEM. Taken from [18].

2.6.2 Brittle fracture

A brittle fracture is a rapid fracture. This type of fracture either grows alongside the grain boundaries, or along crystal planes. They are named inter-crystalline and trans-crystalline fracture, respectively. The mechanism for trans-crystalline brittle fracture is called “cleavage” [18, 19]. Such a fracture is shown in Figure 16.

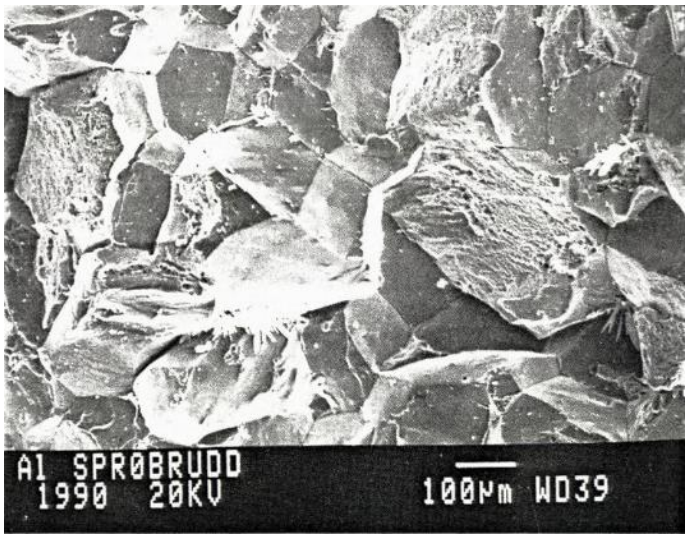

Figure 16: A brittle inter-crystalline cleavage fracture. Taken in SEM. Taken from [18].

2.6.3 Fatigue fracture

This section will deal with high-cycle fatigue fracture, as it is the relevant fatigue-type for this study. Fatigue is failure due to cyclic stress, as earlier mentioned. Fatigue fracture separates itself from the other fracture types, as it does not need to surpass the yield strength of the material. Tiny cracks and surface defects are frequent initiation points, because they yield greater local stresses. Other favourable orientated slip planes are also good initiation points. Every crack does not necessarily develop into a critical crack [18]. A fatigue crack usually develops in three stages [16, 18]:

1. Crack initiation and growth along slip-planes, often in a 45° angle to the applied tension direction. As the crack grows along certain crystal-planes, it can be confused with a cleavage fracture.
2. The crack changes its growth direction, from going along certain crystal-planes, to perpendicular to the tension direction.
3. Cross-section area has been greatly reduced, and the material can no longer withstand the tension. A transition over to either a ductile, brittle or combination fracture will then occur. This can also be called overload fracture.

Studying the fracture on a macroscopic level, it is possible to see these stages with the naked eye. They are then called “beach marks”. It is also possible to figure out the fracture initiation point with the naked eye [18]. However, this is not always possible. Therefore, SEM is used. On a microscopic level, it is possible to see “striations”. These are results of either one or possible several load cycles [18]. It is possible for fatigue to occur without striations [16]. In Figure 17, striations in an aluminium alloy can be seen. The length in between each striation tends to increase with crack length. By tracing them back to their origin, it is possible to discover the location of the crack initiation point. If the cyclic-frequency and length between striations is known, crack growth can be calculated.

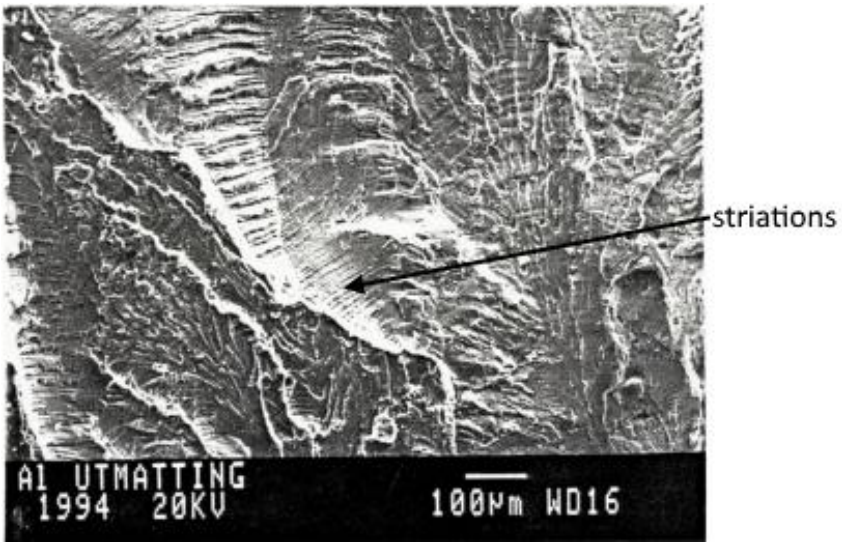

Figure 17: Striations in aluminium (from a helicopter rotor). Adapted from [18].

2.7 Corrosion and corrosion fatigue

Corrosion fatigue is the combination of fatigue and exposure to a chemical reactive environment [2, 3]. Together they have a greater effect on the material then they do separately. Corrosion fatigue can be quantified through S-N curves like regular fatigue. But the mechanisms behind corrosion fatigue is far more complex. There are mechanical, metallurgical, and chemistry components to corrosion fatigue. This corrosive effect on fatigue life effects a great deal of materials, aluminium included [3]. Corrosion is a time-dependent process. This makes the cyclic frequency important. A sample tested at 1Hz would be exposed to the corrosive medium ten times as long as a sample tested at 10Hz. The corrosive medium does not have to be aqueous like seawater, it can also be gaseous like moisture in air [2].

Corrosion affects the fatigue life from the very start. Before stage I fatigue cracks, the corrosion accelerates plastic deformation and slip processes. Slip step reversal (opposite slip direction following opposite load) can be stopped by any oxidation or adsorption [3]. This effect will accumulate and eventually fracture will occur due to embrittlement or general plastic collapse of the material. This means accelerated fracture initiation. Corrosion fatigue also greatly enhances fracture growth [2, 3].

2.7.1 Intergranular corrosion (IGC)

Intergranular corrosion can be defined as corrosion attacks that selectively targets the grain boundaries or the immediate surrounding area [20]. The surrounding grains or crystals are not corroded. The main IGC causes are: “Chemical segregation in grain boundary, depletion of passivating elements along the grain boundary region, and preferential precipitation of phases along the grain boundary…” [21]. In aluminium alloys, IGC susceptibility depends on; type of alloy, metallurgical structure, and temper states. It can be seen in most heat treatable aluminium alloys and is often related to copper depleted regions. IGC is considered to have a greater effect on fatigue life than pitting, because it results in sharper tips [20].

6xxx alloys do exhibit some susceptibility to IGC, though not as much as 2xxx and 7xxx alloys. The susceptibility of the 6xxx alloys comes from excessive amounts of silicon. The

extra silicon becomes insoluble and has a cathodic effect. The T6 temper state is more susceptible to IGC, especially in harsh chemical environments [20].

2.7.2 Pitting corrosion (Pitting)

The main defense of aluminium against corrosion is the protective oxide layer surrounding it. Any weak spot in this layer is a potential area for pitting corrosion. When the layer breaks down it will expose the material beneath it to corrosion. Pitting corrosion can be defined as localized corrosion attack on an open surface due to anions such as chlorides [21, 22]. There are many factors which influence pitting corrosion: environment, metal composition, potential, temperature, and surface condition [22]. Pitting resistance is known to have an effect on fatigue strength: "… widespread importance and relevance of pitting as the primary reason for severe losses of fatigue strength due to corrosion …" [3]. This is because pitting creates notches/defects which as earlier explained, creates localized stress concentrations.

Topography and surface roughness is one of the main focuses in this thesis. It is therefore important to note that: "In general, samples prepared with a rough surface finish are more susceptible to pitting…" [22].

2.7.3 Stress corrosion cracking (SCC)

SCC and corrosion fatigue are quite similar. Both are a combination of mechanical stress and corrosion reactions. As earlier explained, corrosion fatigue is due to cyclic stress. This is where they differ. Instead of cyclic stress, SCC is usually considered to come as a product of static stress. What materials that are susceptible to SCC depends on a great number of factors. What causes SCC varies from material to material, and alloy to alloy. Some of the most important factors are: type of corrosive environment, temperature, and type of alloy. An alloy can even be susceptible to SCC at one heat treatment and immune at another [22].

SCC also tends to initiate at surface flaws. The cracks can be so small that they are not visible to the naked eye. Both intergranular and trans granular propagation paths can be seen in fractography of this phenomenon. Sometimes at the same fracture surface [22].

2.7.4 Corrosion rate

Corrosion rate is the speed at which a corrosive medium corrodes a type of material. This is uniform corrosion. This can therefore be considered a measurement of a material`s corrosion resistance. Equation 10 shows how it is calculated. Corrosion rates are usually given in mm per year.

$$CR = \frac{87.6 * W}{A * D * T} \tag{10}$$

Where W = weight loss (mg), A = surface area (cm^2), D = density of the material (g/cm^3), T = time in corrosive medium (h), CR = corrosion rate (mm/y) [21, 23].

2.8 Surface roughness

Quantifying surface roughness can be done in several ways. There are mechanical and optical methods. Atomic force microscopy (AFM) is a common method where a sharp tip is traced along the surface while measuring the surface. This is a mechanical method. Optical methods, which are used in this study, has the advantage of being non-abrasive and scans large areas

relatively fast [24].

Using optical methods, you have two types of roughness measurements: profile roughness and areal roughness. Area roughness is also called surface texture. The first mentioned measures the difference over a line created in a certain direction. The latter is without direction, and measures the height differences over an area. This is a rather new technique. Profile roughness is commonly used. The differences between the two types of measurements are shown in Table 2. Table 3 shows the abbreviations and definitions of the surface roughness values used in this study.

Table 2: Comparison between profile roughness and surface texture roughness measurement. Inspired by Alicona InfiniteFocusSl manual.

Criterion	Profile roughness measurement	Surface texture measurement
Popularity	Well known	New
Background	ISO 4287, 4288	Surfstand book
Repeatability	Medium	High
Measured area	Small	Large
Result values	Ra, Rq, Rz	Sa, Sq, Sz
Surface structure	With direction	Without direction

Table 3: Abbreviations used to define surface roughness.

Abbreviation	Definition
Ra	Average roughness of profile
Rt	Maximum peak to valley height of roughness profile
Rz	Mean peak to valley height of roughness profile
Rv	Maximum valley height of roughness profile
Rmax	Maximum peak to valley height of roughness profile within a sampling length
Sa	Average height of selected area
Sz	Maximum height of selected area

Rq and Sq, which is the root mean square roughness of profile and selected area, respectively, are not used in this study. Rt, Rv and Rmax are more relevant for fatigue by their very definition. Most of the result values given in Table 3 have a self-explanatory definition. The equation for Ra, which is not self-explanatory, is shown in equation 11.

$$Ra = \frac{1}{l}\int_0^l |z(x)|dx \tag{11}$$

Where Z(x) = difference in height along the profile path (x), l = evaluation length.

Cut of wavelength (Lc) controls how much of the variance in altitude that should be filtered out. This makes it possible to measure surface roughness on a surface which is not flat but with a periodic shape. For example; the helical ridge on a screw. The helical ridge is the shape, with the correct Lc you can measure the roughness on the ridge. For this study, the

profiles can be considered random due to punched surfaces. A guide for choosing Lc based on Ra range is shown in Table 4.

Table 4: Showing Ra range corresponding to Lc and profile length for random profiles. Inspired by Alicona poster.

Ra range	Lc	Profile length
0µm - 0.02µm	80µm	0.4mm
0.02µm - 2µm	250µm	1.25mm
0.1µm - 2µm	800µm	4mm
2µm - 10µm	2500µm	12.5mm
10µm - 80µm	8000µm	40mm

3. Experimental

3.1 Hardening and shaping of samples

Both the hardening and shaping of the samples were executed by Benteler. The initial material was a plate with width, thickness, and length equal to 53x5.3x148mm, respectively. The desired dimensions after shaping are shown in Figure 18. Because of the shaping process, the samples had slight variations in the cross-section area and were measured individually. Please note that the "heads" were shortened, so that they would fit in the machinery.

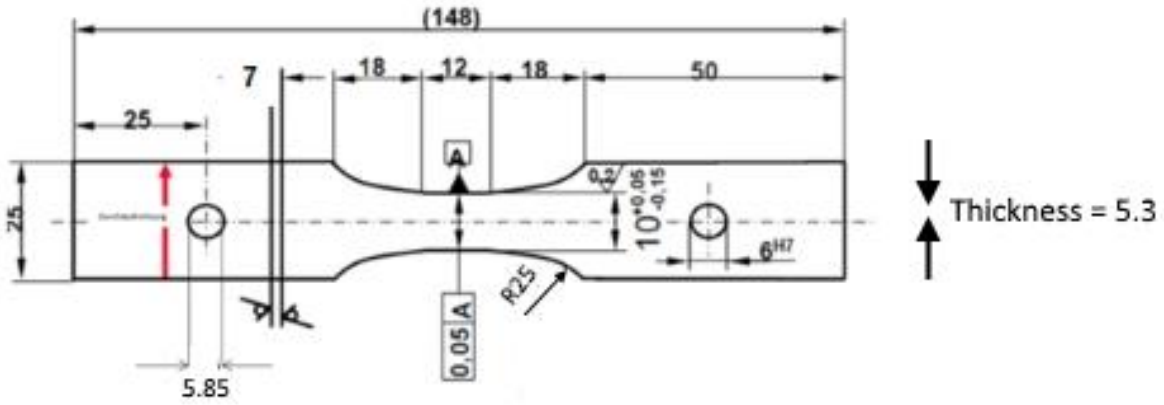

Figure 18: Desired dimensions for finished samples. All dimensions are in mm. Adapted from internal document belonging to Benteler.

All four series underwent the same heat-treatment. The process is shown in Figure 19. After solution heat treatment at 520°C, the samples were quenched to 20°C in water. Within ten minutes after quenching, the punching occurred. The A-series and D-series have a slightly different shaping process, which will be explained in the following subsections. The samples were then artificially aged and air cooled. Lastly, the irrelevant parts were cut off.

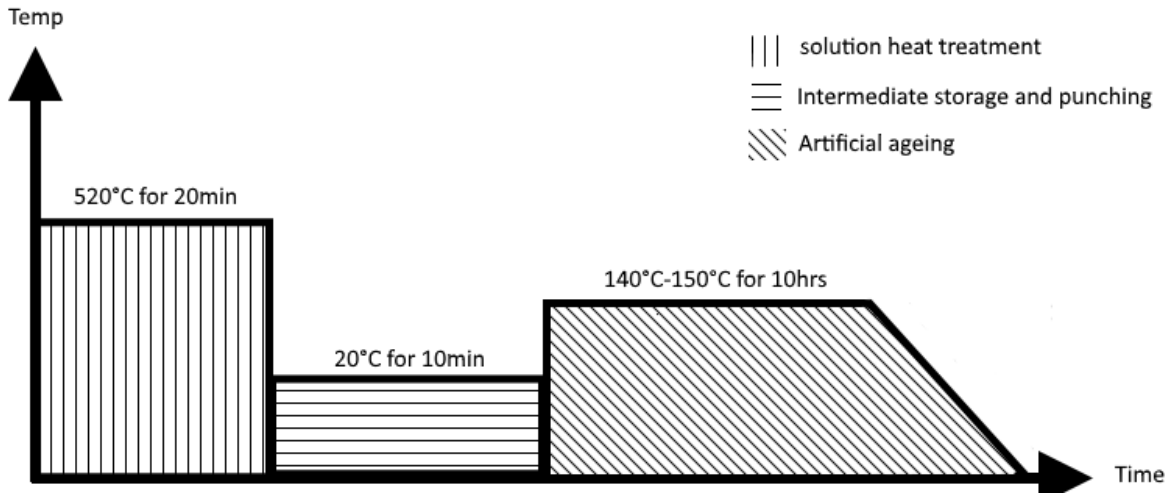

Figure 19: Heat treatment of the samples used. Made by the author.

3.1.1 Shaping processes

The A-series

Trim line and pilot holes for the A-series were not punched, but rather machined by milling. The milling occurred within the same timeframe as the punching. It was machined to the same dimensions as the punched samples.

The B- and C-series

Figure 20 show the shaping process of the B- and C-series. Step 1 consists of the initial plate undergoing solution heat treatment and quenching. In step 2, the samples were punched within ten minutes of quenching, and then put to artificial aging. In step 3, after aging, the samples were machined to specifications (irrelevant parts removed). B-series had a cutting clearance (2.4.2 Cutting clearance) equal to 0.16mm and the C-series had a cutting clearance equal to 0.42mm. This would mean that the cutting clearance relative to sheet thickness was equal to 3.02% and 7.92% for the B- and C-series, respectively. The C-series will not be tested in this study, but was tested in the specialization project.

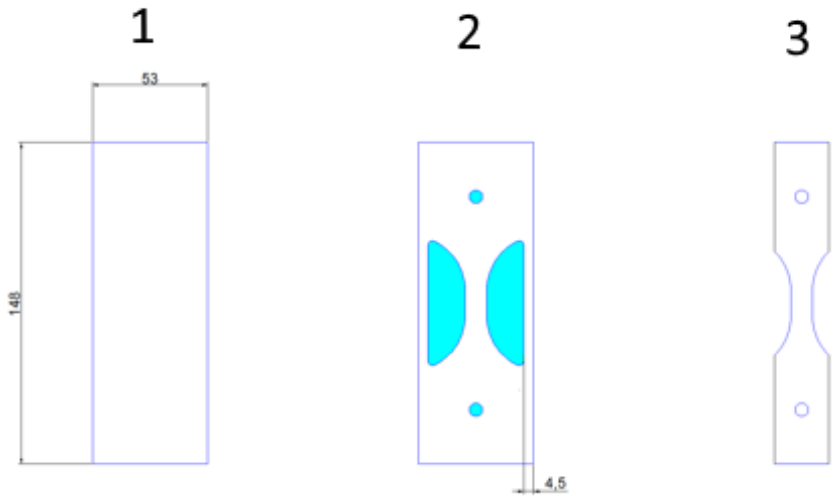

Figure 20: Shaping process of the D- and C-series. Step 1 shows the plate before punching. Step 2 shows the pilot holes and trim lines being punched. Step 3 shows the irrelevant parts cut off. Adapted from internal document belonging to Benteler.

D-series

The samples from the D-series were punched like the B- and C-series, but to slightly wider dimensions. After being punched from one direction the samples were turned around and punched from the other side to the correct dimensions.

3.1.2 Artificial ageing at 180°C

The desire was to find the artificial ageing curve with artificial ageing at 180°C, including T6 and T7. T7 was defined as the same hardness as the slightly underaged samples which were delivered by Benteler. The samples used for these tests were made by NTNU “Finmekanisk verksted” and had the dimensions shown in Figure 21. They were taken from a profile acquired from Benteler. These were made during the fall of 2016 and was stored at roomed temperature until they were used during the spring of 2017.

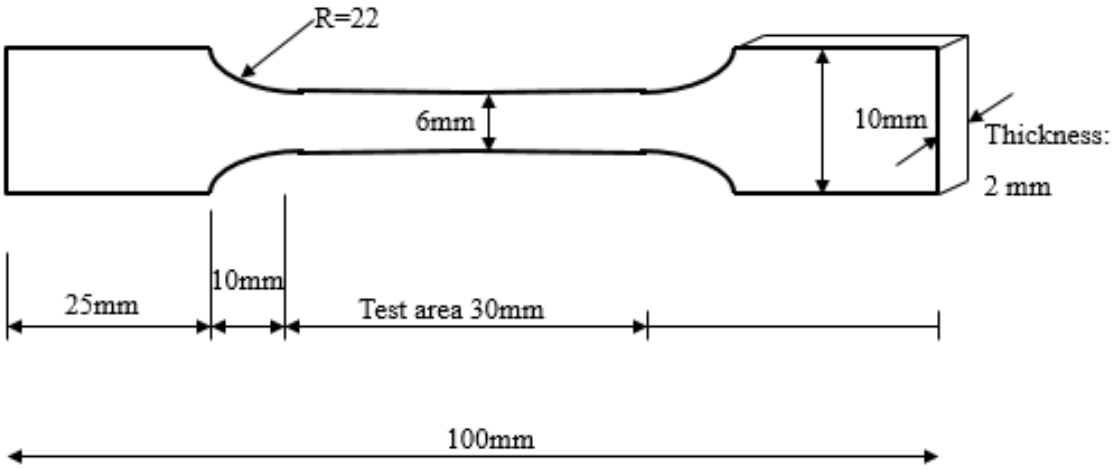

Figure 21: Schematics of samples used in tensile testing and artificial ageing.

The samples were first solution heat treated at 520°C in an air oven for 20min, before being quenched. A six-minute intermediate storage time occurred between quenching and artificial ageing. Then it was heat treated at 180°C in an oil bath. The oven and the oil bath was checked with a separate thermostat. The first sample, used to find a HV-aging curve, was taken out of the oil bath, quenched, then had its hardness measured. It was then put back in the oil bath and the process was repeated. This was used as an indicator for when to take the tensile tests out of the oil bath.

The tensile test samples were taken out at: 10min, 30min, 60min, 120min, 180min, 300min, 720min and 1440min (based on HV-findings). Three samples were heat treated at each time. Figure 22 shows the heat treatment process. The tensile testing machine was the same as for fatigue testing "*MTS 810 Hydraulic tensile testing machine 100kN*".

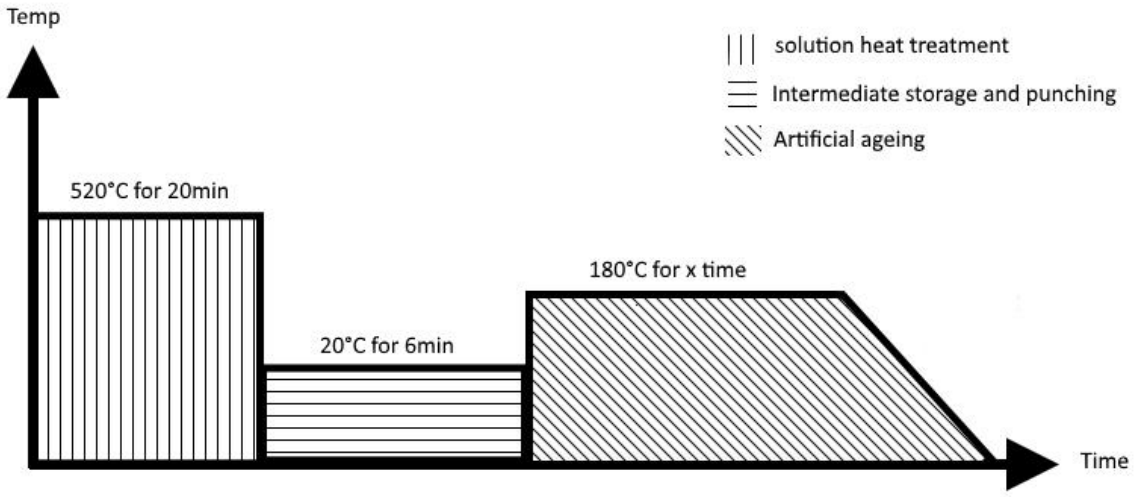

Figure 22: Heat treatment process for artificial ageing at 180°C. The x was chosen based upon when to take out the samples from the hardness measurements.

3.2 Preparation and analysis of samples in light microscope (LM)

One sample from each series that was not tested in fatigue, was used. The samples were cut using a *Struers Discotom-2* to suitable heights. They were then cast into epoxy to create a nice hold around the samples. The LM used was a *Leica MEF4M*. All the samples were prepared at the same time using *ATM Saphir 550*. Four programs were used to polish the samples. Each program can be seen in Table 5. The sample holder was washed when the sandpaper was changed, to avoid any remaining particles to get onto the finer sandpaper. The samples were also cleansed with use of water, ethanol, and very softly applied soap.

Table 5: Polishing program used for the samples used in LM (inspired by the "AKA-notes for Aluminium alloys" by Akasel).

Program	Type of paper	RPM	Polishing lubricant	Time	Force (per sample)
1	500-sandpaper	150	Water	2*30sec	15N
2	Largo/Largan 9μm	150	Diamaxx 9μm Poly	3min	20N
3	DiaDoublo 3μm Poly	150	Diamaxx 3μm Poly	2*2min	15N
4	Fumed Silica 0.2μm Alkaline	150	Fumed Silica	1min	10N

After polishing the samples were cleansed and anodized. Anodization happened in a 5% HBF_4 and 95% H_20 solution, for 90s per sample. Afterwards, LM was used to get micrographs of the grain structure. Polarization and λ-plate was used. They were manipulated until a good image appeared.

3.3 Topography

Every sample used in corrosion fatigue testing in the B- and D-series were scanned using *Alicona InfiniteFocusSl.* Scanning took place prior to testing. The scan was used to measure surface roughness of the individual samples and to characterize the topography. The optical scanner works by first selecting x-, y-, and z-coordinates. Then it takes numerous pictures at different x-, y- and z-coordinates to create a 3D-image of the surface. Alicona InifiniteFocusSl is based on focus variation. Meaning it chooses the pictures which are in focus to create the 3D-image. The vertical and horizontal resolution depends on how often the machine takes a picture. A 10x lens was used, which has the capability of a vertical resolution equal to 100nm. This was the resolution used for every sample scanned. The cut off wavelength (LC) was set to 8.000 mm.

Because of the way the scanner works, it can only detect changes in the vertical direction which are not optically blocked. The area shown in Figure 23 by a circle, would not be detected. This is illustrated by the arrows representing light, which would be reflected before reaching the bottom of the valley. This means that the depth registered may actually be an underestimated depth of the wounds.

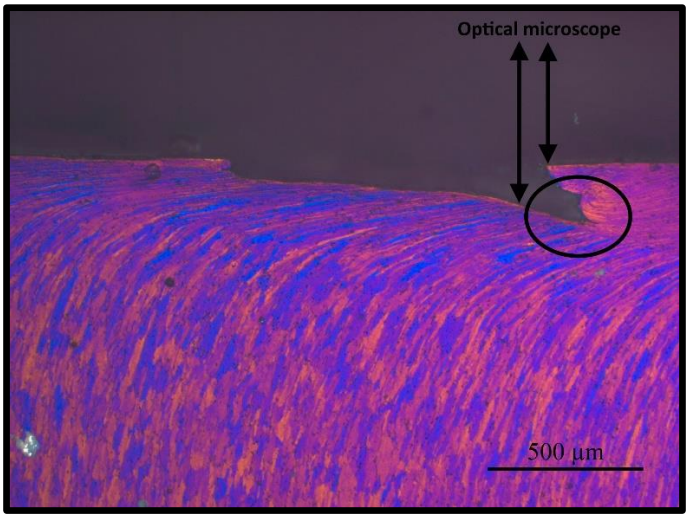

Figure 23: Grain structure surrounding a wound of a punched surfaces. The circle shows the area which would not be picked up by the optical microscope. The arrows signify how the light beams would be reflected.

The area of the samples which were scanned is shown in Figure 24. This is the so called “test area”. This is where the samples have the smallest cross-section area. It is also the area which was measured to calculate the force for fatigue testing. This area (with a good margin) was submerged in saltwater during testing. Every scanned sample caught a little of the curvature, to make sure it got the whole test area.

Figure 24: Photo showing the area which was scanned.

Surface roughness was measured by taking the average of 2000 measurements in the test area of the sample. This is shown in Figure 25. Both sides were scanned. The fracture path for some samples were recreated with 10 measurements checking for elevated local surface roughness.

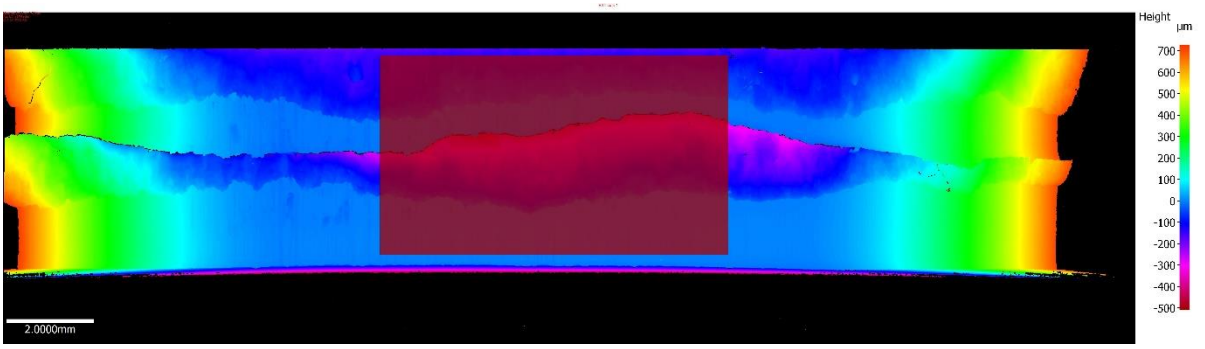

Figure 25: A height filtered photo of B14 showing how the surface roughness was measured. The red area represents 2000 separate lines measuring surface roughness. The average of these lines was used. In this case the measurement started at the bottom of the red lines. That is because the top is where the sample was flat and the local reference plane was set to 0.

When measuring areal roughness, a section within the test area was chosen as shown in Figure 26. After choosing the area and switching from primary to roughness filter, the local reference plane was once again redefined in the flat area. In this figure, it would be the top part which is flat.

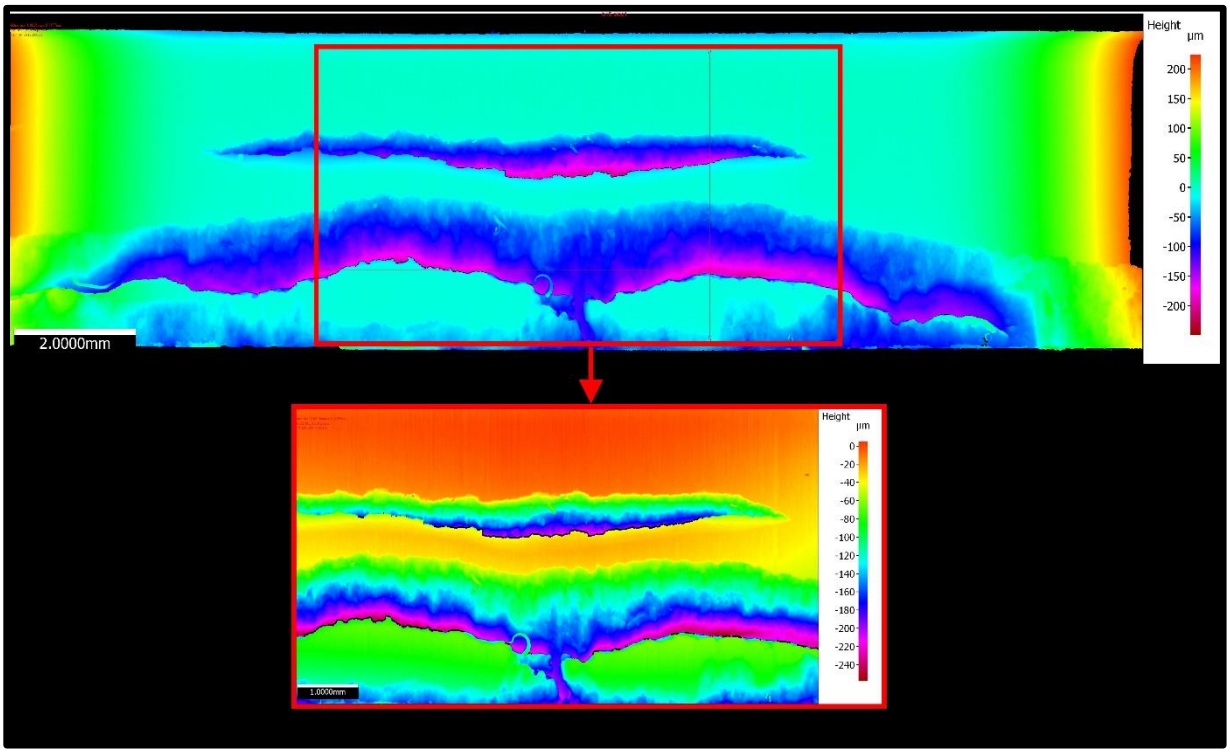

Figure 26: Showing how the areal roughness was chosen.

3.4 Corrosion fatigue testing

The “MTS 810 Hydraulic tensile testing machine 100kN” has no built-in function to perform corrosion fatigue testing while samples are submerged in an aqueous solution. It was necessary to design a chamber which could safely contain the saltwater without spilling during testing. The initial design and the updated versions are shown in the following subsection. Though there were some problems with the corrosion fatigue testing of the A-series, the chamber proved itself both simple to use and efficient.

3.4.1 Chamber design

The design was simple. It would be separated into two parts; a disc and a chamber made out of aluminium and plexiglass, respectively. The disc would be joined with the sample using silicone (*Pattex Easy Silicone* was used). Then the disc would be joined with the chamber using either silicone or a type of glue. Since the discs were made from aluminium and were easy/cheap to make, several of them were made straight away. This allowed for several samples to be cast at one time. The number of chambers, which were far more time consuming to make, were kept to a minimum. The machine and samples were measured to design a chamber which would fit in the machinery. It would also allow for the whole test area to be submerged in saltwater. In Figure 27 you can see the initial design. In Figure 28 you can see how the samples were cast to the disc using silicone. Figure 29 shows how it looked after being mounted to the chamber.

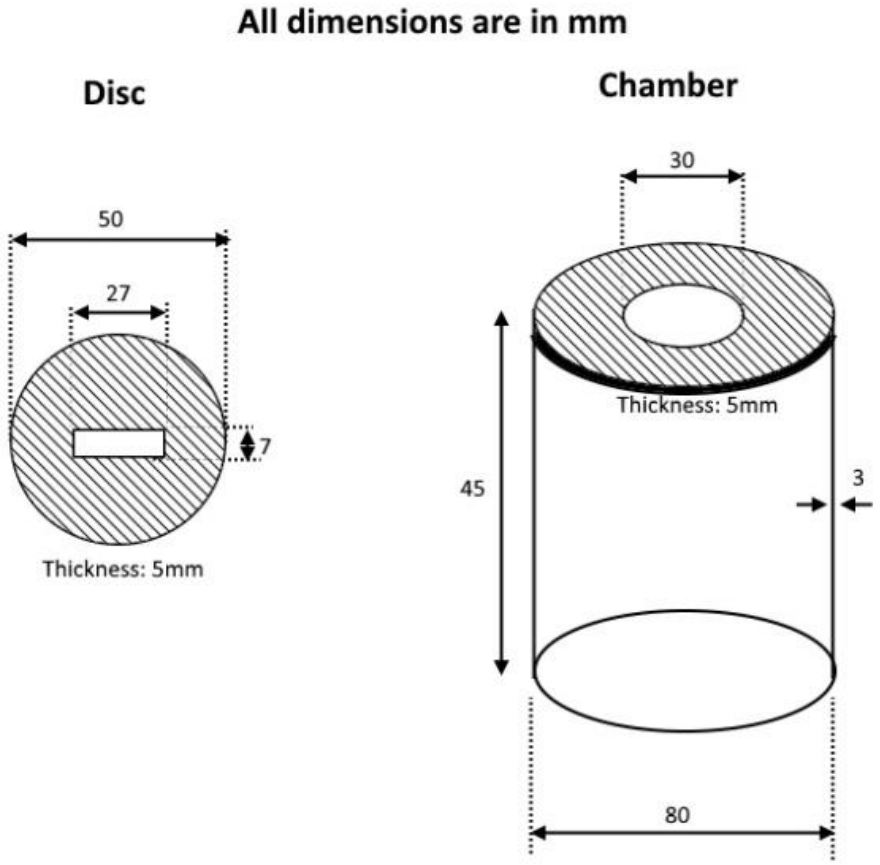

Figure 27: Schematics of the prototype chamber and discs

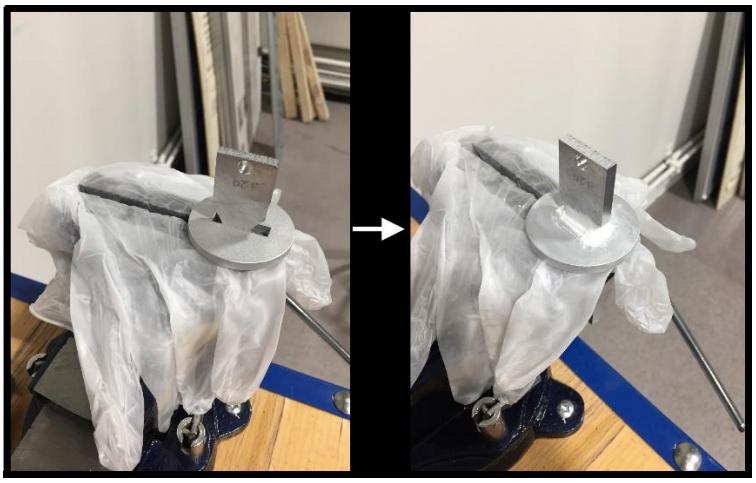

Figure 28: Casting process of the samples to the discs using silicone.

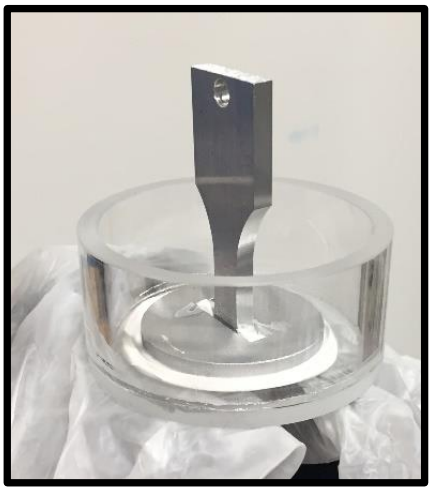

Figure 29: Sample with disc mounted to the first chamber.

Casting the samples to discs proved to work very well. But the first chamber did not give the samples more than the minimum of grip area needed (2/3 of the head). The grip area is shown in Figure 30. The samples tested (A-series) kept having fractures outside the test area with this set up. It was thought that more grip would solve the problem. There was also an attempt to use glue instead of silicone to attach the disc to the chamber. This proved to stick so well that the chamber almost broke trying to separate the two after testing. Therefore, silicone was use for mounting the disc to the chamber as well.

A new chamber was designed with bigger dimensions to get more grip. This would allow the walls of the chamber to go slightly up the angled sides of the machinery. In Figure 30 you can see the angled area of the machinery, and how the chamber was set up in the machinery. In the figure, you can see the machine being above the chamber with a good margin. This is because when fastening the samples, the gripping blocks stay at the same altitude but the machine goes upwards. Meaning every mm possible was used when fastening it.

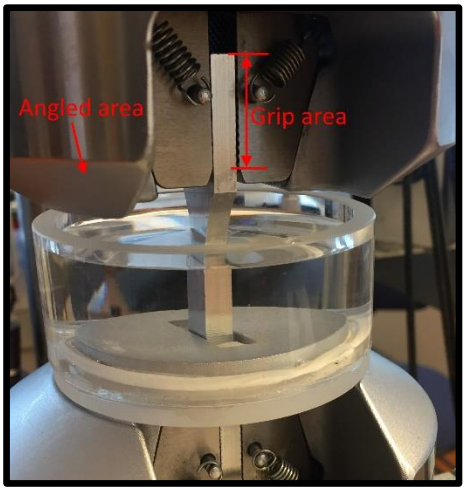

Figure 30: Second chamber set up in the machine.

The A-series kept having fractures outside the test area with the second chamber as well. A third chamber with sufficient radius to go around the machinery was made. This chamber also had thinner discs and a thinner bottom to get 3-4 extra mm of grip. This chamber can be seen in Figure 31.

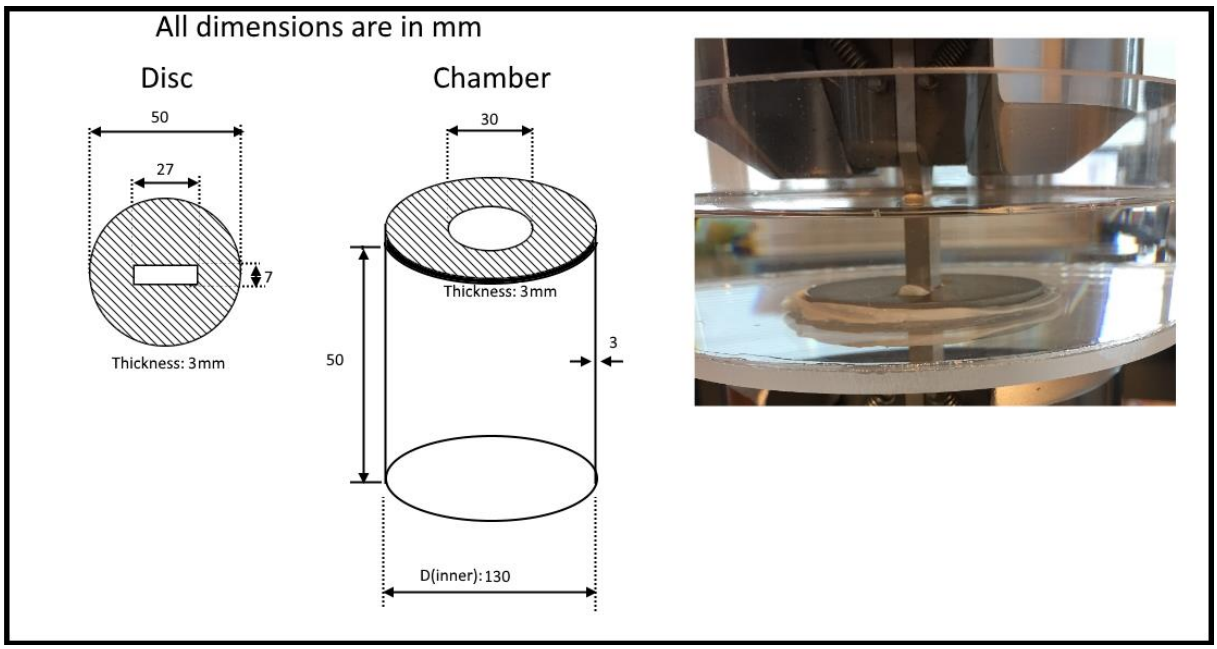

Figure 31: Schematics for the third chamber and photo of chamber in use.

The problem of fracture outside the test area persisted. With this chamber, it was certain that the grip area was more than sufficient. Both the B- and D-series had fractures inside the test area with the second and third chamber.

An attempt was made to reduce the cross-section area even further through polishing. This was an undesired technique because it would affect the edges. Several samples were attempted with this technique. The thickness was reduced with as much as 0.1mm. This did not solve the problem and was cast away for another solution.

A new approach to solve the problem, became to smoothen the curved part of the samples with a 1200 sandpaper. It did not affect the edges in the test area, and was therefore superior to the previous approach. This would reduce any local stress concentrations due to machine defects outside the test area. Thankfully, this worked. The second chamber was retested with this method, and it worked there as well. Sadly, it did not work a 100% of the time. Some samples still failed outside the test area. This was probably due to uneven smoothening. But, it worked with enough samples to create an S-N curve. The second and third chamber was both used as they showed no difference in results. Both have sufficient grip area and can submerge the test area with saltwater.

3.4.2 Cleansing of the samples and chamber

Sample cleansing:
Every sample was first cleansed in acetone in an ultrasonic bath for two minutes. Afterwards the samples were dipped in water to get most of the acetone off. Then they were cleansed with ethanol. They were then dried and sealed inside unused plastic bags. The samples were handled with plastic gloves during and after cleansing to avoid new contaminations.

Disc cleansing:
The discs were cleansed in the same way as the samples for each time they were used. It was necessary to remove the leftover silicon in between tests. This was done mainly by using the backend of a “snap-off” utility knife. The acetone removed the remaining bits of silicone. This were done for two reasons; Silicon does not stick well to old silicon and to create the most similar conditions for every test.

Chamber cleansing:
The chambers were made from plexiglass. Plexiglass breaks down in both acetone and ethanol. Therefore, the chambers were cleansed (wearing gloves) with soap and thoroughly flushed with distilled water. The silicon leftovers on the chamber were easily removed in water.

3.5 Corrosion rate

The goal was to measure the weight loss of a sample in the 5 wt% NaCl solution. One sample from the A-, B-, and D-series were chosen. These were first scanned to discover the surface roughness, and then carefully measured. The surface area for each sample was calculated through sectioning the samples. Figure 32 shows how the samples were sectioned (picture of a B-series sample). One part is not shown, which is the end parts on both sides. These were taken in account. *B1* and *B2* stands for the corresponding *T1* and *T2* below the sample. These were individually calculated because of different lengths on the different sides of the samples. In the mid-section, some assumptions were made. Symmetry was assumed for the *MT1* and *MT2*, and the M1 + M + M2 part could be multiplied by 4 taken in account the other sides (below and the side facing away from the camera). Also, the curved area (MT1 and MT2) with the middle part (MT) was assumed to follow the schematics shown in Figure 18. The thickness was measured. The surface area and calculations for each part can be seen in Appendix D: Corrosion rate calculations.

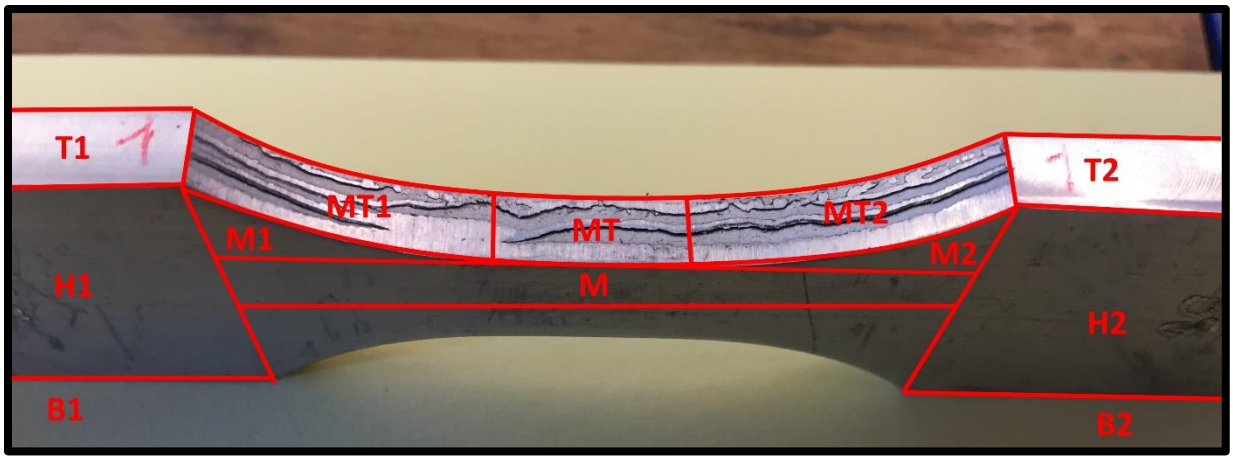

Figure 32: Showing how the samples were sectioned to calculate the surface area of the samples.

Each sample was cleansed with acetone to remove fat. Afterwards they were all individually put in 69% HNO3 solution, for 5min, to see if there were any weight change just due to the acid. The weight after exposure to the acid was used as initial weight. It showed a very slight difference. This was probably due to loose particles.

Every sample was left in the saltwater for ca 1 day before taken out for weighing. The cleansing process was done through 12.5 min in 69% HNO3 and cleansed with water and ethanol afterwards, before drying of in air. The first time this was done, the samples were left in the acid for 10min, weighed, then put back in the acid for 5min. There was a change of 0.2mg in one of the samples (the rest remained the same) with the extra 5 min. Therefore, 12.5min was thought to be sufficient time in the acid. The saltwater was changed out in between each measurement to ensure the most similar testing conditions. Testing ended after one week.

3.6 Fractography (SEM)

Every sample studied in the SEM (16 in total) was first carefully pulled apart using the same tensile machine. They were then cut to a suitable height (1-2cm) being careful not to damage the fractured surface. The sample name was engraved carefully so that the samples could not be mistaken. Thereafter they were cleansed with soap applied very softly and flushed in water. To remove any fat stains that might be on it, every sample was left for 5minutes in acetone. The acetone was flushed off with water and ethanol before being dried off. To minimize any contaminations in form of dust particles, the samples were kept in clean aluminium foil sheets. The samples were mounted in the SEM as shown in Figure 33. The SEM used was “Zeiss Supra, 55 VP”, and the accelerating voltage was set to 10kV. The sample order was written down, and recognizable characteristics were noted so that it was possible to identify the sample while using the SEM.

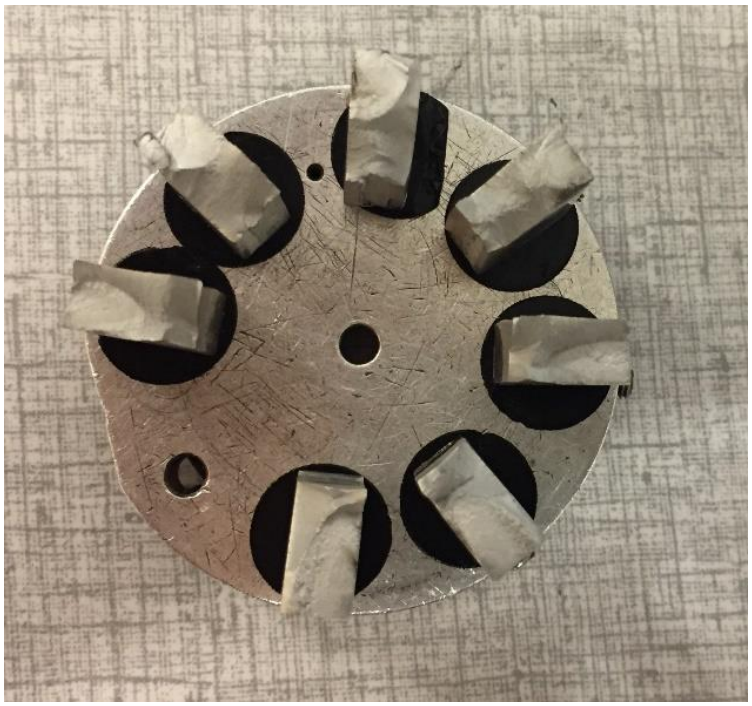

Figure 33: Mounting of samples before used in SEM analysis.

4. Results

4.1 Samples

Chemical analysis of the samples used, performed by Sintef Raufoss, is shown in Table 6. A tensile test performed by Benteler of the samples are shown in Figure 34. This represents every series at is made from the same material and heat-treated the same way. There was a shortage of B- and D-series samples (these were made in Germany and could not easily be resupplied), which is why they were not given their own tensile test. They would also be deeply affected by the flawed surfaces. Average yield strength and ultimate tensile strength is 336.5MPa and 382MPa, respectively.

Table 6: Chemical analysis of the AA6082 alloy executed by Sintef Raufoss. The measured values are in wt%.

SINTEF Raufoss manufacturing

	Fe	Si	Cu	Mg	Cr	Mn	Zn	Zr	Ti	Ni
Measured	0,18	0,89	0,00	0,57	0,13	0,56	0,04	0,00	0,02	0,00
U(95%)	0,0058	0,0091	0,0012	0,0074	0,0046	0,0141	0,0005	0,0005	0,0011	0,0016

Expanded uncertainty (U95%) with a confidence interval (k=2) is based on the calibration uncertainty and the repeatability of the machine, iSparc 8880

Results:

Legends	Nr	Specimen id.	S0 mm²	L0 mm	Rp 0,2 MPa	Rm MPa	Ag %	A %	HV10
	1	1	53,1	41,1	340	384	5,1	9,0	116
	2	2	53,6	41,3	333	380	5,1	9,1	117

Series graph:

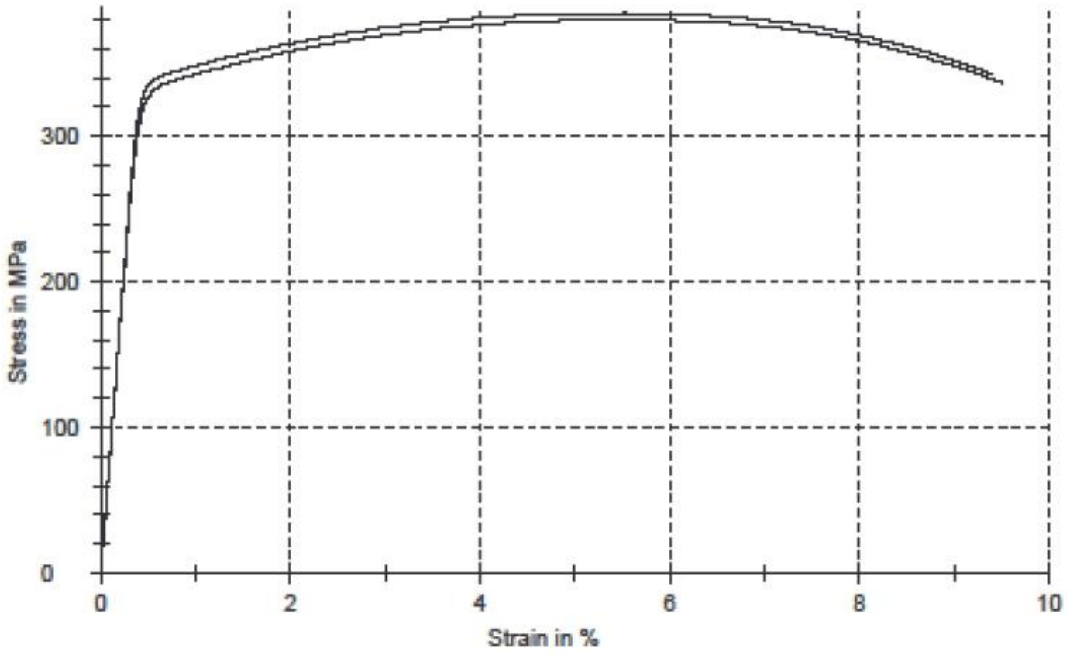

Figure 34: Tensile test data of two samples from the A-series. Test performed by Benteler.

4.2 Microstructure

All the samples have been extruded and have the exact same fibrous structure before the shaping process. Which means that in the middle of every sample they look the same. In every micrograph in this section the extrusion direction is perpendicular to the picture (coming out of picture). However, due to the different shaping processes we have different grain structures at the punched/machined edges. Figure 35, Figure 36, and Figure 37 shows the grain structure after machining, punching and counter trimming, respectively. The punching (and counter trimming) has a severe effect on the grain structure, and a great deal of deformation occurs.

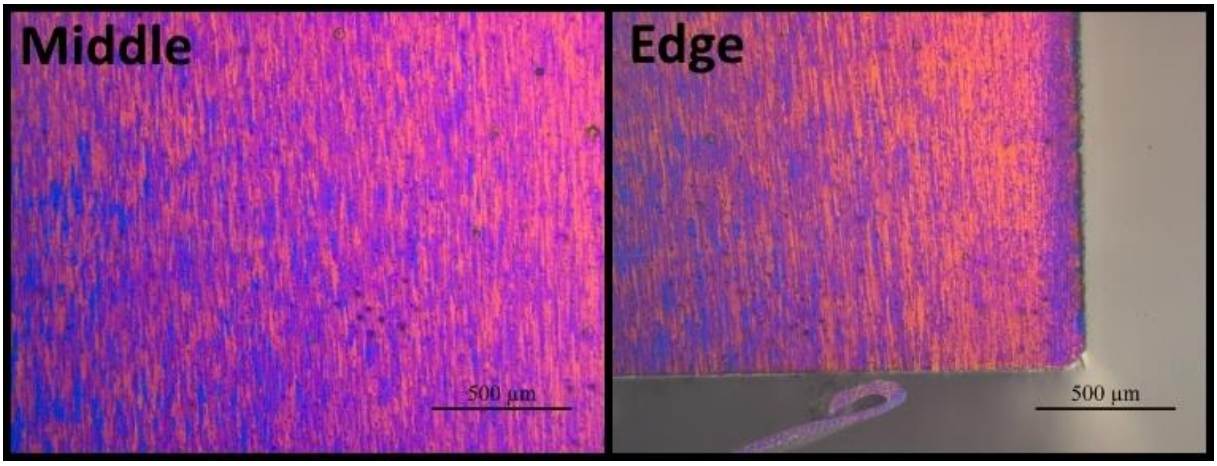

Figure 35: Grain structure of the middle (which is the same in every series) to the left, and the edge of a machined sample (A-series) to the right. It is the bottom part of the "Edge"-micrograph which is corresponding to the punched edges.

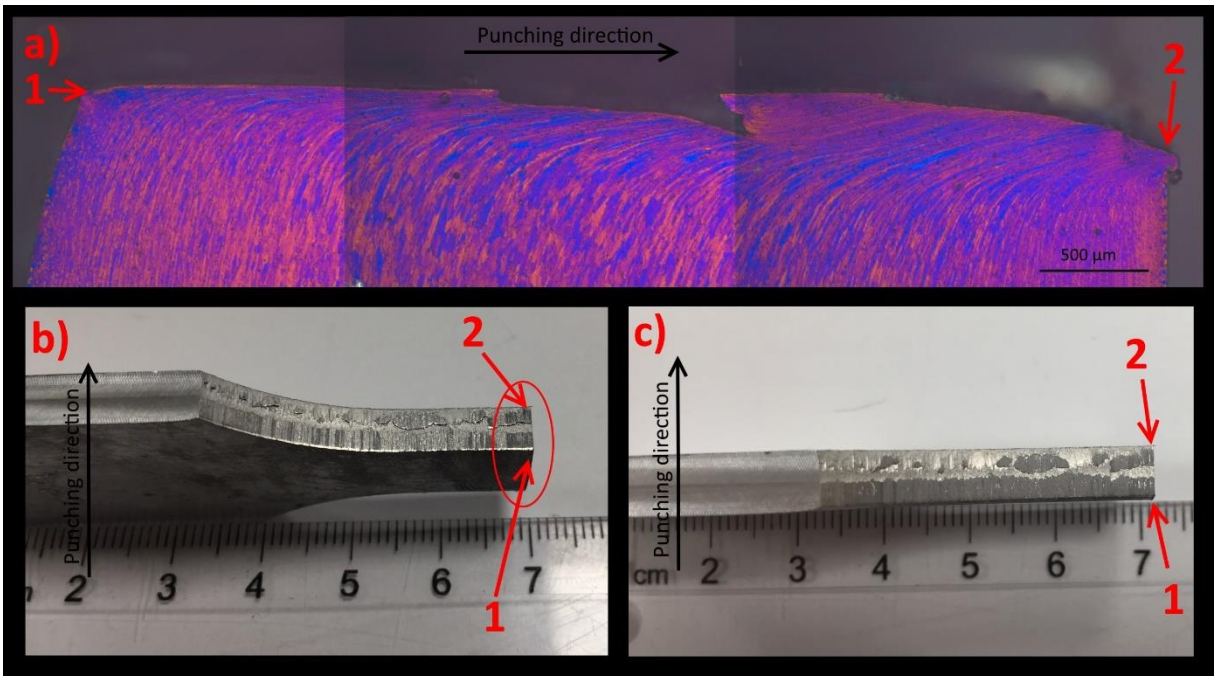

Figure 36: Grain structure after punching (B-series). Point 1 and 2 are the same in micrograph denoted by a, and the pictures b and c. In the micrograph (a) the grains have been pulled with the punching direction.

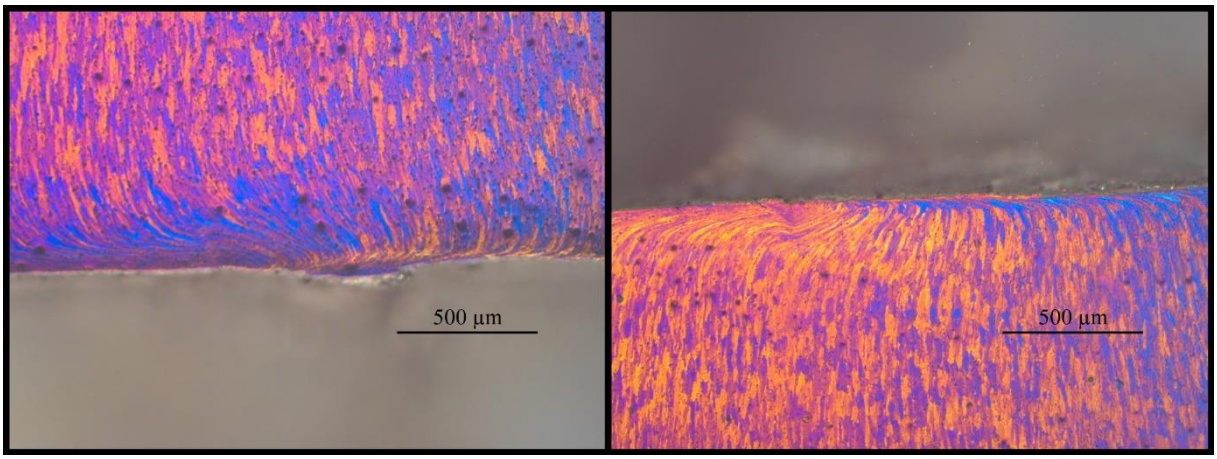

Figure 37: Grain structure of a counter trimmed surface (D-series). The grains were first pulled with the first punch towards one direction, then pulled the other way around with the second punch.

4.3 Topography and surface roughness

The A-series (machined) did not have all its corrosion fatigue tested samples scanned prior to testing. This was because the surface roughness and topography only had small variations, and scanning small variations is time consuming. Six samples were measured to find a trustworthy average of that series. Every sample tested in corrosion fatigue in the B- and D-series were scanned prior to testing. Table 3 shows the definitions of the surface roughness values used. More topographies can be seen in Appendix A: Topography.

4.3.1 A-series

As mentioned, the A-series showed very little variance in surface roughness. An unfiltered and a height filtered photo of the A-series are shown in Figure 38. The middle part, which is purple in color in the filtered surface, is the test area. This is where the sample is flat and at its thinnest. The height elevation on both sides is where the curvature starts and continues to the "head" of the sample.

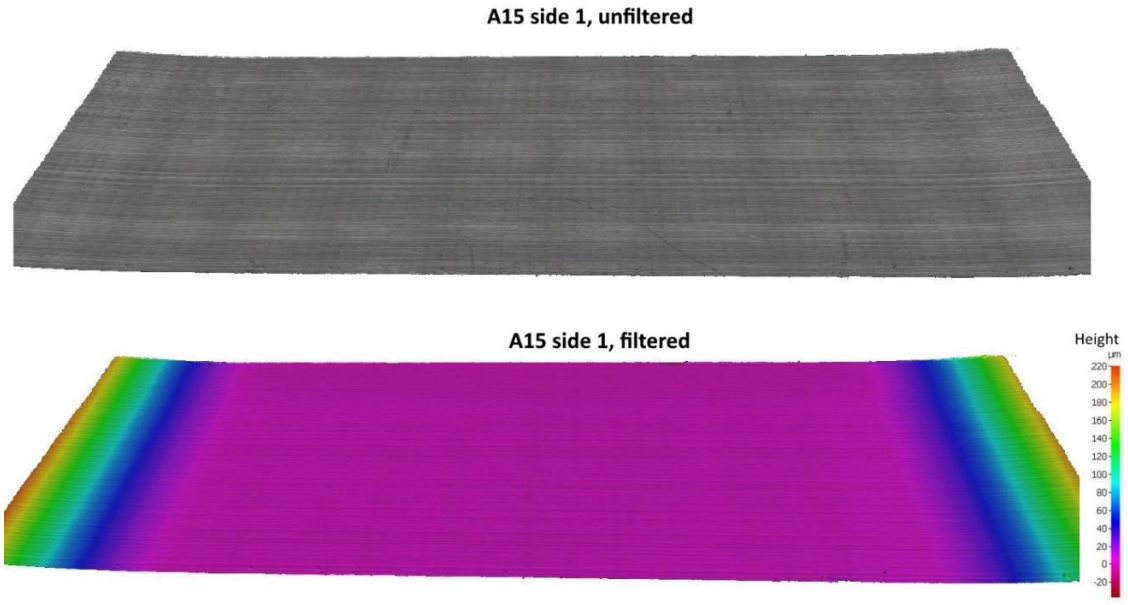

Figure 38: A 3D view of the machined edge in the A-series of sample A15. Top picture showing an unfiltered photo and the bottom photo showing a height filtered photo. The scale bar is in µm.

Figure 39 shows the profiles of an A-series sample. It represents the average of 2000 measurements and show how the surface varies in height. Please note that the roughness profile does not begin at 0 (x-axis) as the primary profile does. This is due to the nature of calculating roughness. As it is possible to see from these profiles, the A-series only has a difference ranging over five µm. Compared to the B- and D-series, it is a very small difference in height.

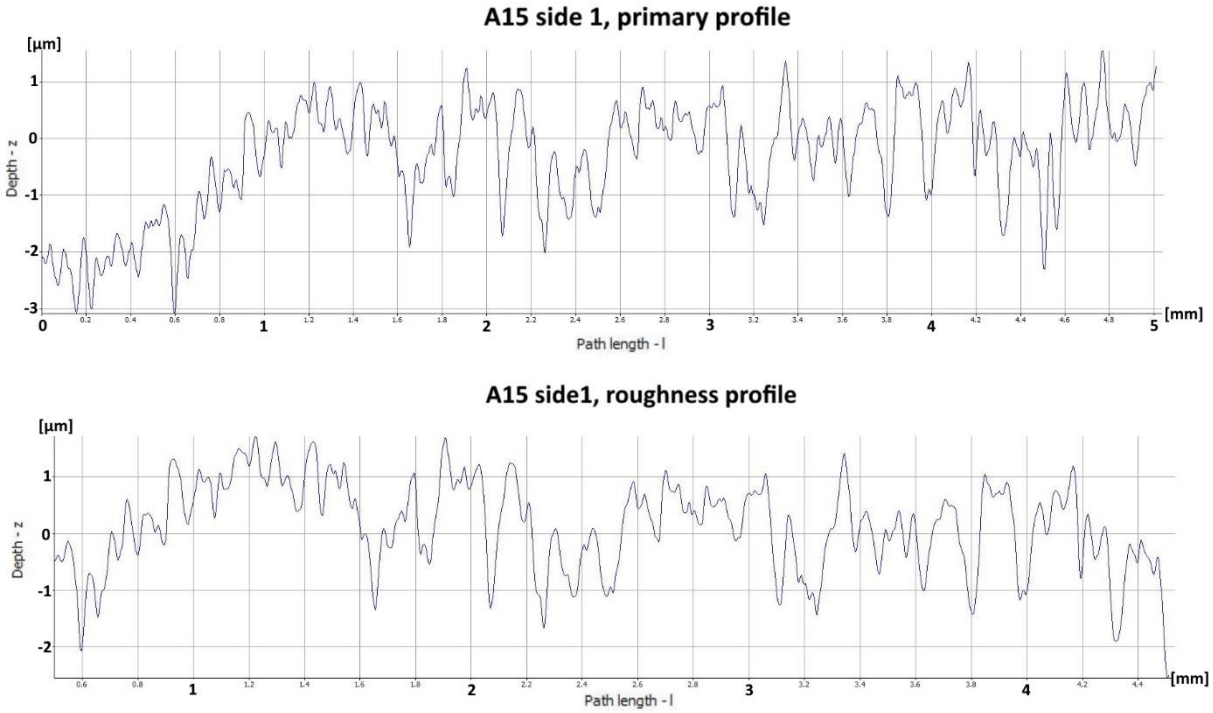

Figure 39: Describes the profiles of the A15 sample. The X-axis is the path length, meaning the length of the measurement, and the Y-axis is the depth, meaning variations in the Z-direction (height) on that path. The X-axis is in mm and the Y-axis is in µm.

Figure 40 shows the part chosen to calculate the areal roughness. You can clearly see a square like pattern in height differences. Green here signifies one positive µm and blue one negative µm. The top part of the photo is lower than the bottom part, which is the same as in the primary profile.

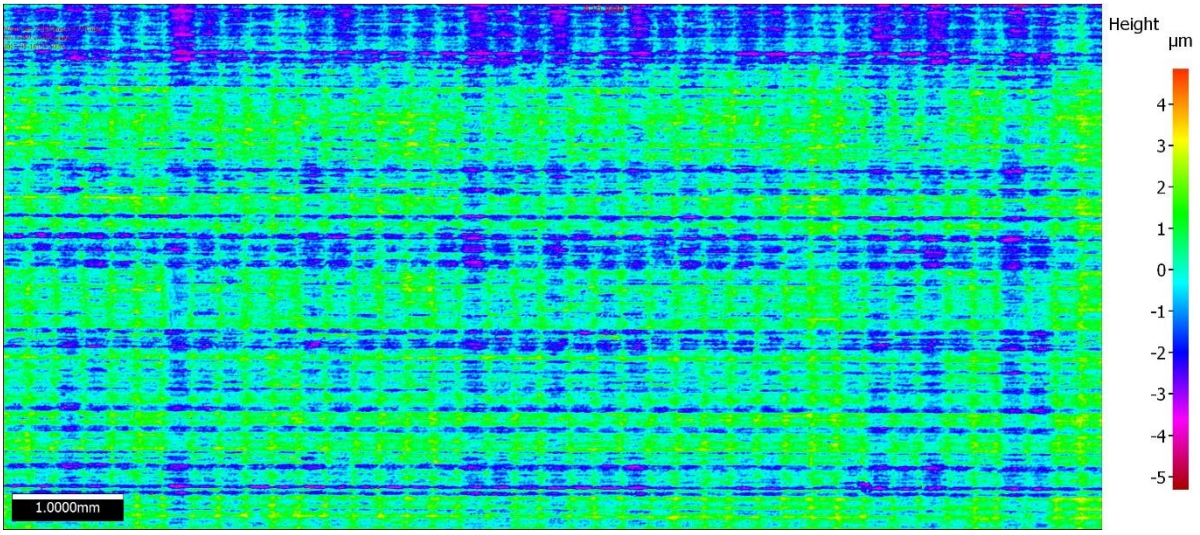

Figure 40: Areal roughness section for A15.

In Table 7 the resulting data for the A-series is displayed. As earlier mentioned, only six samples were scanned. The values are much lower than the values seen for the B- and D-series.

Table 7: Surface roughness values for the A-series.

Sample	Ra [µm]	Rt [µm]	Rz [µm]	Rmax [µm]	Rv [µm]	Rt/Rz	Sa[µm]	Sz[µm]
A13 side 1	0.690	5.3	3.8	4.4	3.1	1.4	0.964	39.9
A13 side 2	0.663	5.2	3.6	4.2	2.8	1.4	0.929	54.3
A15 side 1	0.655	4.3	3.3	3.8	2.6	1.3	0.916	10.2
A15 side 2	0.664	4.4	3.4	4.1	2.6	1.3	0.974	19.5
A20 side 1	0.737	5.5	3.8	5.2	3.4	1.4	0.938	11.1
A20 side 2	0.594	4.8	3.2	3.9	2.8	1.5	1.032	26.5
AA8 side 1	0.833	5.8	3	4.3	2.1	1.9	1.276	13
AA8 side 2	0.940	6.6	3	4.4	2.2	2.2	0.930	17.3
AA13 side 1	0.566	4.2	1.9	3.6	1.1	2.2	1.115	44.2
AA13 side 2	0.657	3.6	1.8	3.0	1.2	2.0	0.995	51.8
AA16 side 1	0.491	4.6	3.0	4.5	0.9	1.5	0.966	45.7
AA16 side 2	0.406	4.6	2.0	4.2	0.6	2.3	0.650	26.5
Average	**0.658**	**4.9**	**3.0**	**4.1**	**2.1**	**1.7**	**1.0**	**30.0**
stdev	**0.142**	**0.8**	**0.7**	**0.5**	**0.9**	**0.4**	**0.1**	**16.4**

4.3.2 B-series

The B-series, unlike the A-series, showed a great number of different surfaces. The two sides on one sample varied from each other and samples varied from other samples. One sample is shown in Figure 41.

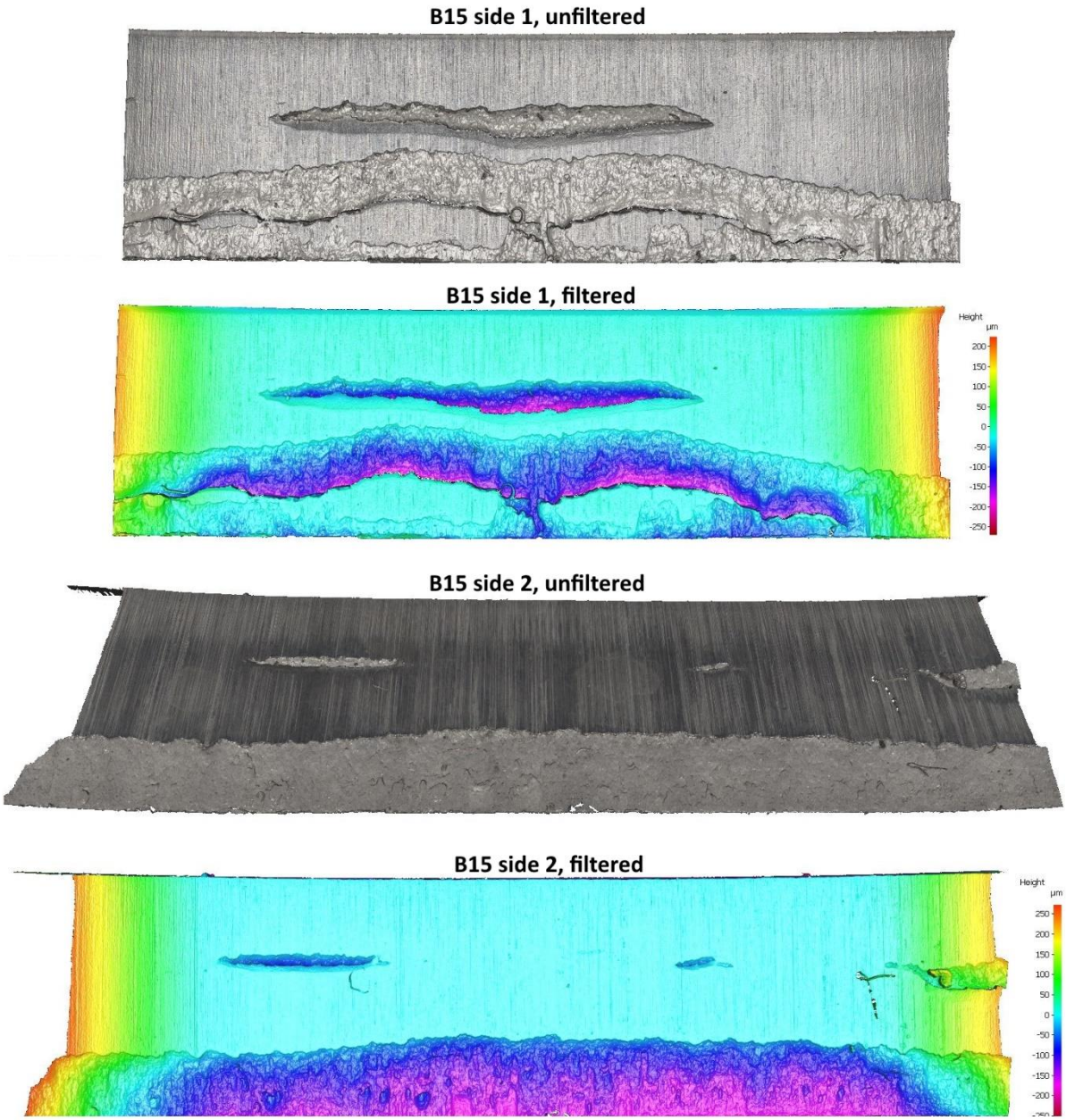

Figure 41: Photos showing the different topographies of sample B15, representing the B-series.

The corresponding profiles for B15 side 1 is shown in Figure 42. As seen by the primary profile, the second wound goes as deep as 120 µm. This is the average depth of this wound taken by 2000 individual measurements. Meaning the wound might be deeper than 120 µm at certain locations. Remember that the wounds can be even deeper than what the profiles can register as well (3.3 Topography).

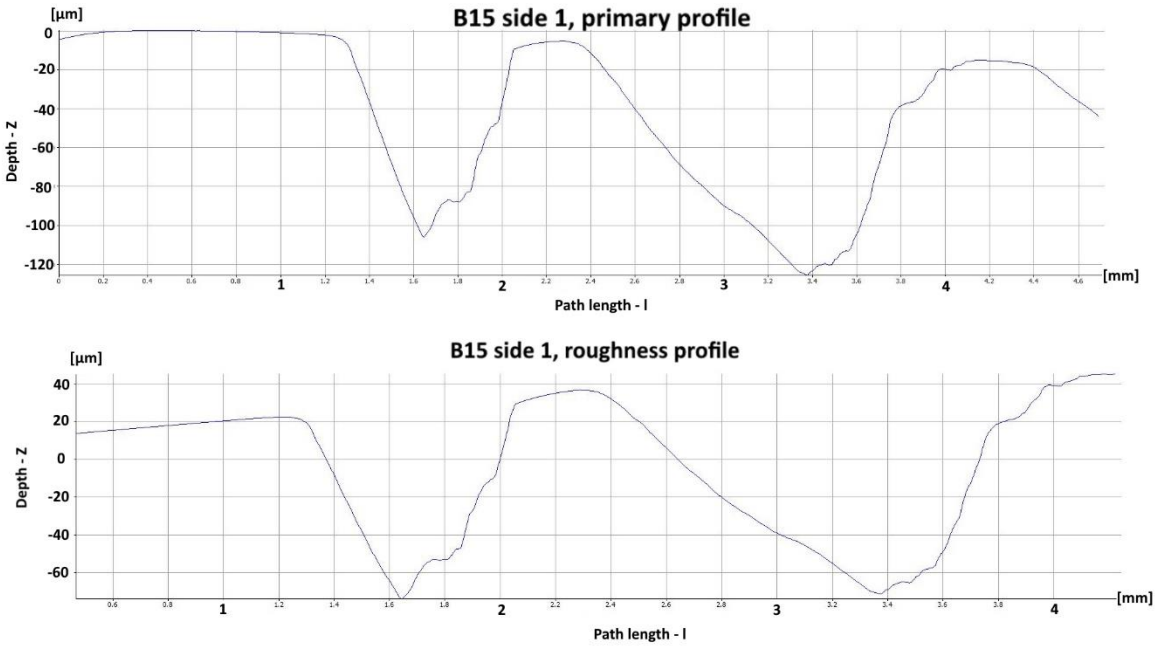

Figure 42: Profiles of sample B15 side 1. The X-axis is the path length, meaning the length of the measurement, and the Y-axis is the depth, meaning variations in the Z-direction (height) on that path. The X-axis is in mm and the Y-axis is in µm.

Figure 43 shows the area chosen to calculate areal roughness. The top part was chosen as a reference plane, as it was the flattest area. It is possible to see certain areas which reach -200 µm in depth judging by the color. Judging by this photo, it is also likely that the wounds continued even further and deeper. That is because there is a black line around the green part, suggesting the machine had problems finding the difference in height at that spot.

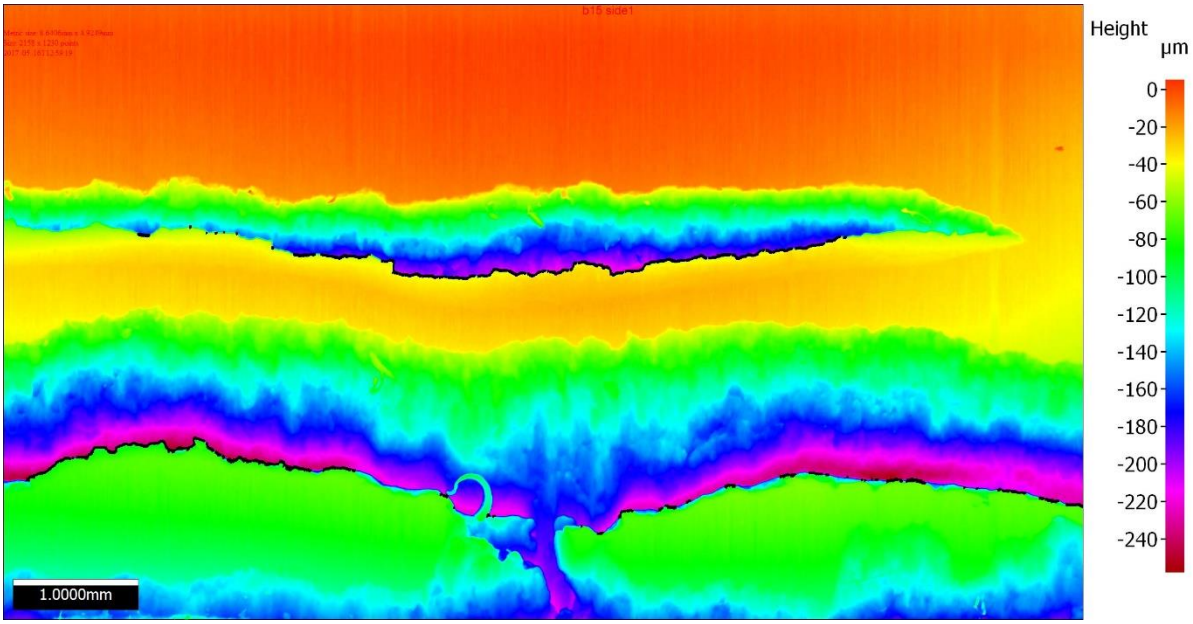

Figure 43: Areal roughness section of B15.

The fracture for this specific sample has been recreated. An illustration of where the fracture propagated is shown in Figure 44. This illustration is also used to measure the surface roughness on this exact path.

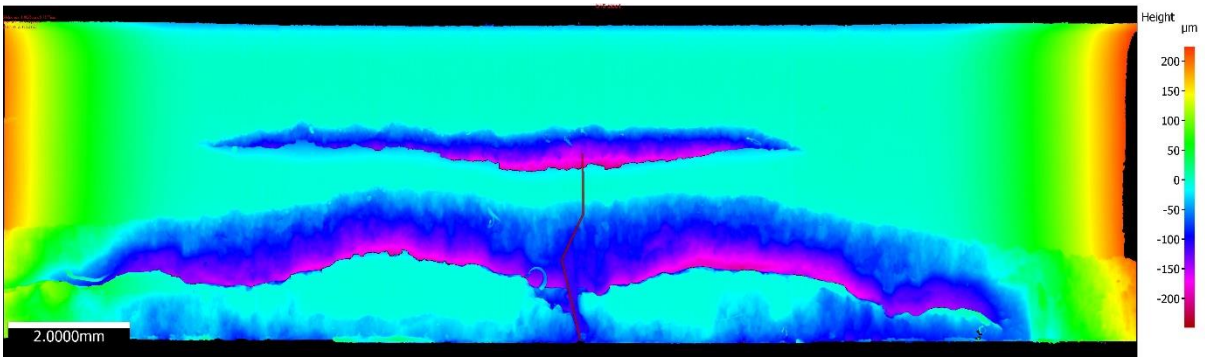

Figure 44: Fracture propagation path for sample B15. The propagation is shown as a red line. This red line is 10 new measurements, measuring the surface roughness on this exact path.

Table 8 show the data for every sample tested in saltwater for the B-series. It also includes the fatigue life, max stress, and which side fracture occurred. Table 9 shows the data which corresponds to the surface roughness on the fracture propagation path. Figure 45 shows how Rv varied as a function of fatigue life.

Table 8: Surface roughness data for the B-series. Green indicates the side which had fracture initiation.

Sample	σ_a [MPa]	Nf (cycles)	Ra [µm]	Rt [µm]	Rz [µm]	Rmax [µm]	Rv [µm]	Rt/Rz	Sa[µm]	Sz[µm]
B6 side 1	72	104449	32.3	133.7	66.3	132.4	103.9	2.0	77.1	321.2
B6 side 2	72	104449	14.5	64.8	23.3	64.8	29.9	2.8	20.2	227.7
B14 side 1	72	94639	63.8	240.1	112.4	240.1	146.3	2.1	163.7	524.7
B14 side 2	72	94639	41.7	174	66.3	122.9	122.9	2.6	97.3	339.3
B21 side 1	72	122401	13.1	79.4	33.2	76	29.0	2.4	25.8	356.8
B21 side 2	72	122401	39.1	161.5	66.3	116	116.0	2.4	97.8	302
B25 side 1	72	159411	18.2	78.5	38.4	65.1	50.0	2.0	52.8	242.3
B25 side 2	72	159411	20.4	83.4	30.7	51.5	31.7	2.7	18.3	234.3
B31 side 1	72	90029	51.7	186.3	71.8	140.2	140.2	2.6	114.8	362.5
B31 side 2	72	90029	27.4	111.9	40.4	68.3	47.9	2.8	24.6	183.9
B18 side 1	99	38264	24.6	102	41.2	56	41.7	2.5	22.4	165.2
B18 side 2	99	38264	40.4	163.1	101.3	159.8	120.3	1.6	101.6	362.8
B19 side 1	99	38794	26.7	146.4	62.6	140	112.9	2.3	90.5	313.3
B19 side 2	99	38794	28.2	147.3	50.5	106.1	85.8	2.9	21.1	171.7
B23 side 1	99	45903	38.8	158.6	90.8	158.6	116.7	1.7	89.9	262.2
B23 side 2	99	45903	28.9	129.5	54.2	95.7	74.9	2.4	60.1	366.6
B26 side 1	99	38226	37.1	112.3	57.4	97.9	78.4	2.0	87.8	301.3
B26 side 2	99	38226	21.4	93.9	31.1	57.9	41.8	3.0	21.3	206
B32 side 1	99	38508	41	173.9	102.6	173.8	135.6	1.7	81.7	263.8
B32 side 2	99	38508	26.8	105.9	40.9	65.6	47.2	2.6	29.2	221.6
Average:			**31.8**	**132.3**	**59.1**	**109.4**	**83.7**	**2.4**	**64.9**	**286.5**
Stdev:			**12.6**	**44.4**	**26.1**	**49.6**	**41.1**	**0.4**	**41.3**	**86.8**

Table 9: Local fracture surface roughness and the whole side surface roughness data. For the B-series

Sample (overall)			Local (fracture path)		Difference (Local - sample)	
Sample	**Rmax [µm]**	**Rv [µm]**	**Rmax [µm]**	**Rv [µm]**	**Rmax [µm]**	**Rv [µm]**
B6 side 1	132.4	103.9	157.7	136.0	25.3	32.1
B14 side 2	122.9	122.9	210.3	150.4	87.4	27.5
B21 side 2	116	116.0	155.9	128.2	39.9	12.1
B25 side 1	65.1	50.0	Could not be found			
B31 side 1	140.2	140.2	127.7	68.8	-12.5	-71.4
B18 side 2	159.8	120.3	Could not be found			
B19 side 1	140	112.9	176.7	137.2	36.7	24.3
B23 side 1	158.6	116.7	61.2	31.9	-97.4	-84.8
B26 side 2	57.9	41.8	Could not be found			
B32 side 1	173.8	135.6	180.4	153.8	6.6	18.1

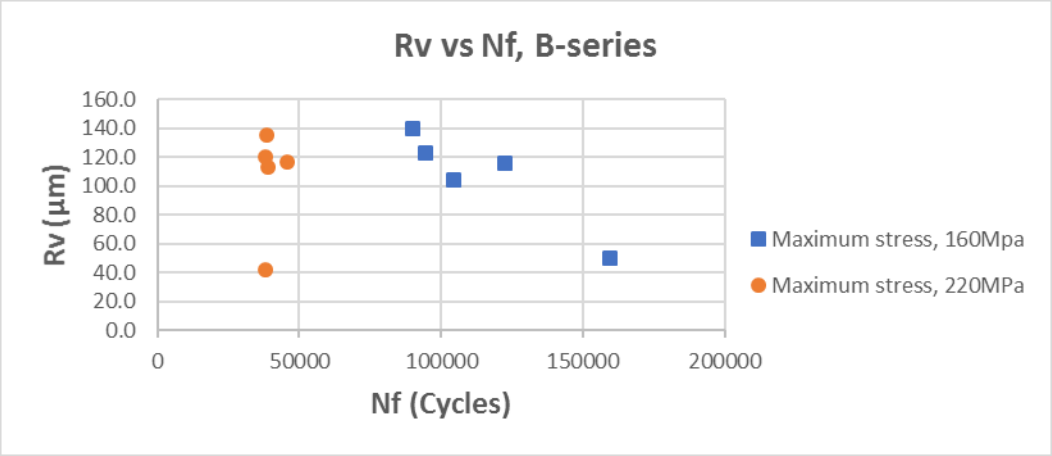

Figure 45: Showing Rv as a function of Nf for the B-series.

4.3.3 D-series

The D-series (counter trimmed) also showed a unique variety of surfaces. An example of the D-series topography is shown in Figure 46. Please note that this is only one of many different topographies for this series.

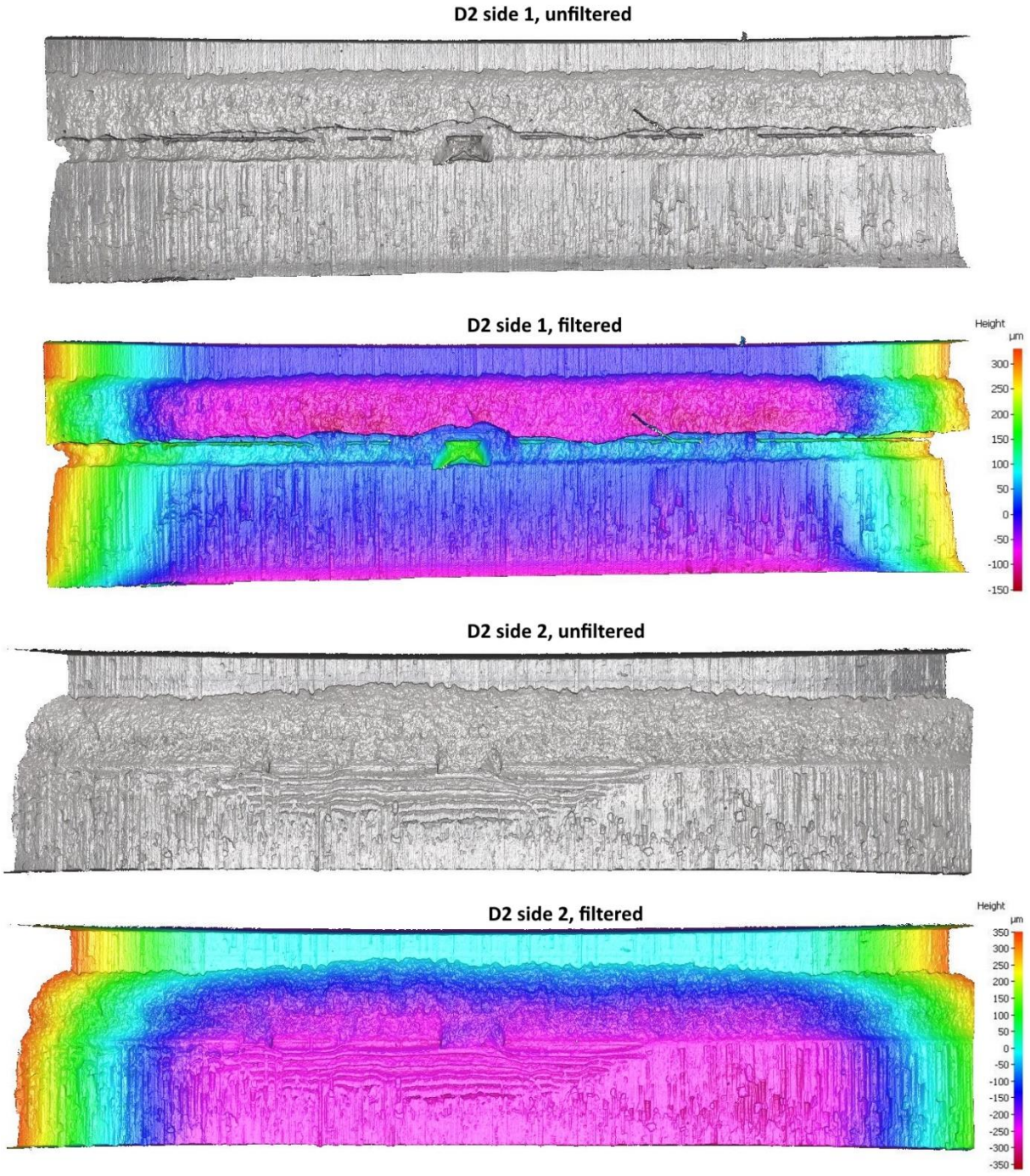

Figure 46: Photos showing the different topographies of sample D2, representing the D-series.

The corresponding profiles for D2 side 1 are shown in Figure 47. As seen by the primary profile and the photo above, the D-series can have a higher peak in the middle of the counter trimmed surface.

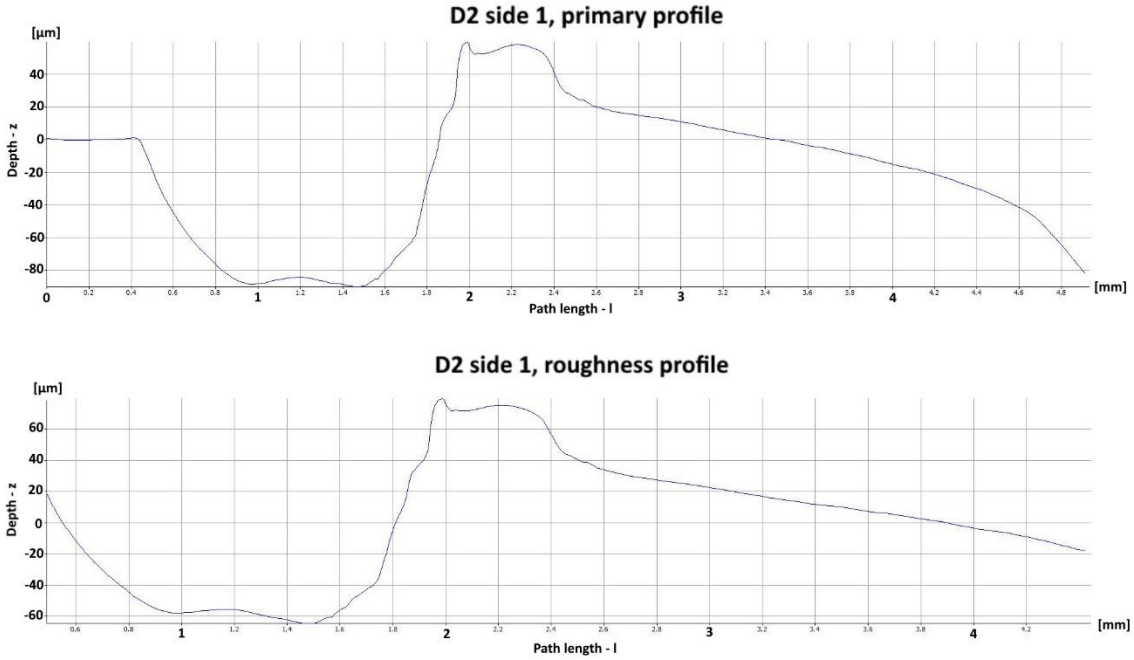

Figure 47: The corresponding profiles for D2 side 1, representing the D-series.

Figure 48 shows the section used to calculate areal roughness for the D2 sample. Here the height difference is even more apparent.

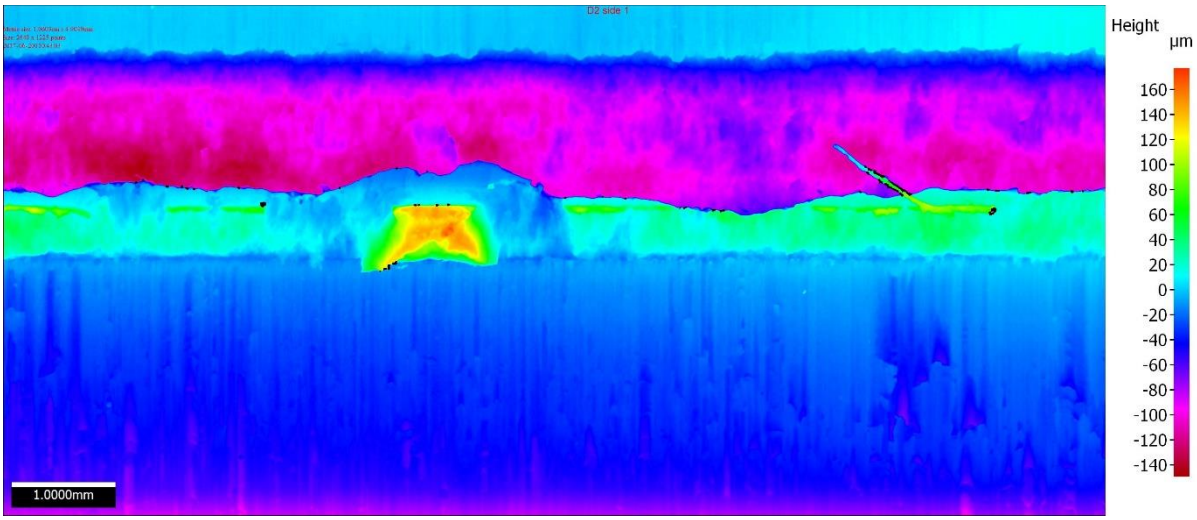

Figure 48: Areal roughness section for D-2.

The D-series had several fractures occurring directly at the end of the test area as shown in Figure 49. These were accepted as within the test area. Some however was perfectly in the middle. The height filtered photos of D2 side 1 shows there is a peak almost 150 µm above the reference plane. A large amount of material must have accumulated at this location during shaping.

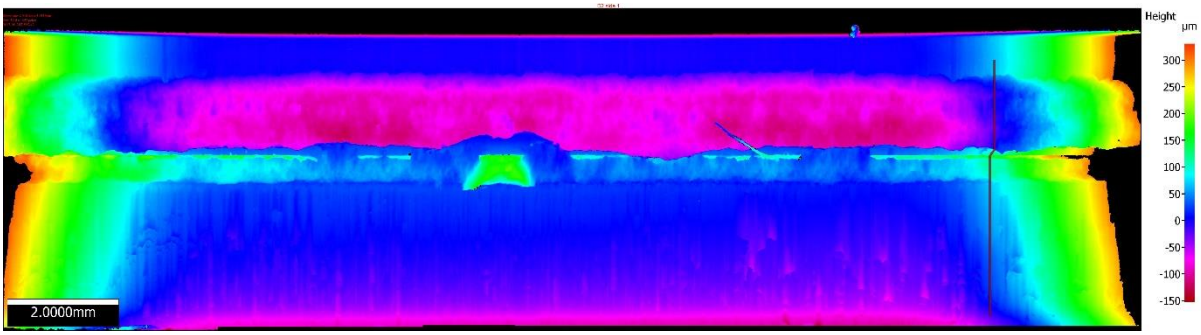

Figure 49: Fracture propagation path for sample D2. The propagation is shown as a red line. This red line is 10 new measurements, measuring the surface roughness on this exact path.

Table 10 and Table 11 shows the surface roughness data for the D-series. Though still having a lot higher surface roughness than the A-series, the extra punch seem to have improved its surface roughness compared to the B-series. Figure 50 shows how Rv varied as a function of fatigue life.

Table 10: Surface roughness data for the D-series. Green indicates the side which had fracture initiation.

Sample	σ_a [MPa]	Nf [cycles]	Ra [µm]	Rt [µm]	Rz [µm]	Rmax [µm]	Rv [µm]	Rt/Rz	Sa[µm]	Sz[µm]
D5 side 1	72	145308	19.9	94.5	37.9	94.5	48.3	2.5	142.4	338.3
D5 side 2	72	145308	17.4	85.3	36.8	72.1	36.0	2.3	143.1	299.7
D17 side 1	72	152601	16.4	84.3	41.4	77.7	48.8	2.0	22.2	239.1
D17 side 2	72	152601	17.4	63.7	32.8	57.4	37.6	1.9	121.1	261.5
D24 side 1	72	186642	25.4	109.4	46.6	95.5	51.1	2.3	28.6	180.2
D24 side 2	72	186642	30.2	122.3	52.2	72	58.1	2.3	252.9	505.4
D26 side 1	72	169710	29.3	133.4	55.5	121.6	69.1	2.4	44.9	201.2
D26 side 2	72	169710	27.3	112.9	51.1	96.9	44.2	2.2	231.9	463.4
D34 side 1	72	177364	26.8	106.2	48	71.7	48.4	2.2	286.7	606.6
D34 side 2	72	177364	32.1	131.6	56	109.3	59.9	2.4	40.2	270.2
D2 side 1	99	51795	33.4	144	62.9	144	64.5	2.3	33.2	317.4
D2 side 2	99	51795	28.8	117.7	52	78.5	53.7	2.3	276.7	562.9
D7 side 1	99	52200	17	86.9	43.8	86.9	49.7	2.0	126.6	266.5
D7 side 2	99	52200	18	92.7	48	89.8	49.4	1.9	152.6	341.9
D30 side 1	99	58990	28.8	126.7	45.6	101.1	46.9	2.8	31	276.7
D30 side 2	99	58990	22.7	96.8	44.1	57.3	46.0	2.2	233.7	490.3
D32 side 1	99	57014	20.7	83.1	37.8	71.5	37.8	2.2	76.1	326.9
D32 side 2	99	57014	20	92.7	40.3	72.4	38.6	2.3	236.3	482.6
D39 side 1	99	48170	25.3	115.6	69.1	115.6	52.9	1.7	122.6	250.6
D39 side 2	99	48170	16	84.5	42.3	84.2	48.8	2.0	93.5	282.7
Average:			**23.6**	**104.2**	**47.2**	**88.5**	**49.5**	**2.2**	**134.8**	**348.2**
Stdev:			**5.7**	**21.0**	**9.1**	**22.0**	**8.8**	**0.2**	**90.2**	**124.4**

Table 11: Local fracture surface roughness and the whole side surface roughness data for the D-series

Sample (overall)			Local (fracture path)		Difference (Local - Sample)	
Sample	**Rmax [µm]**	**Rv [µm]**	**Rmax [µm]**	**Rv [µm]**	**Rmax [µm]**	**Rv [µm]**
D5 side 1	94.5	48.3	140.5	81.9	46.0	33.6
D17 side 1	77.7	48.8	68.9	46.4	-8.8	-2.4
D24 side 1	95.5	51.1	78.0	49.5	-17.5	-1.5
D26 side 1	121.6	69.1	112.8	62.9	-8.8	-6.2
D34 side 2	109.3	59.9	Could not be found			
D2 side 1	144	64.5	182.0	60.5	38.0	-4.0
D7 side 2	89.8	49.4	59.1	36.7	-30.7	-12.6
D30 side 1	101.1	46.9	Could not be found			
D34 side 1	71.7	48.4				
D32 side 2	72.4	38.6	47.5	47.5	-24.9	9.0
D39 side 1	115.6	52.9	150.0	49.5	34.4	-3.4

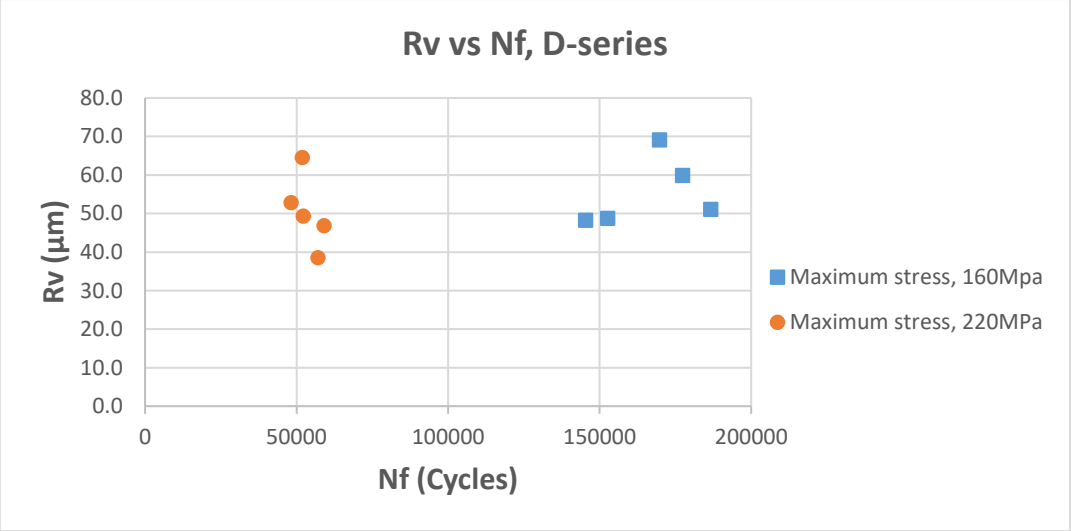

Figure 50: Showing Rv as a function of Nf for the D-series.

4.4 Corrosion fatigue results

The cross-section area of all the samples were individually measured. Every sample was submerged in a 5wt% NaCl solution and tested with R = 0,1. Figure 51 shows the S-N curve for the different series tested in corrosion fatigue. The A-series showed a superior fatigue life in saltwater than the B- and D-series. The B- and D-series however, had far better spread. Subsections 4.4.1-4.4.3 will show each series individually with reference tests in both air and distilled water. The raw data and standard deviation can be seen in Appendix B: Fatigue data. Every point in every graph in this section represents one test.

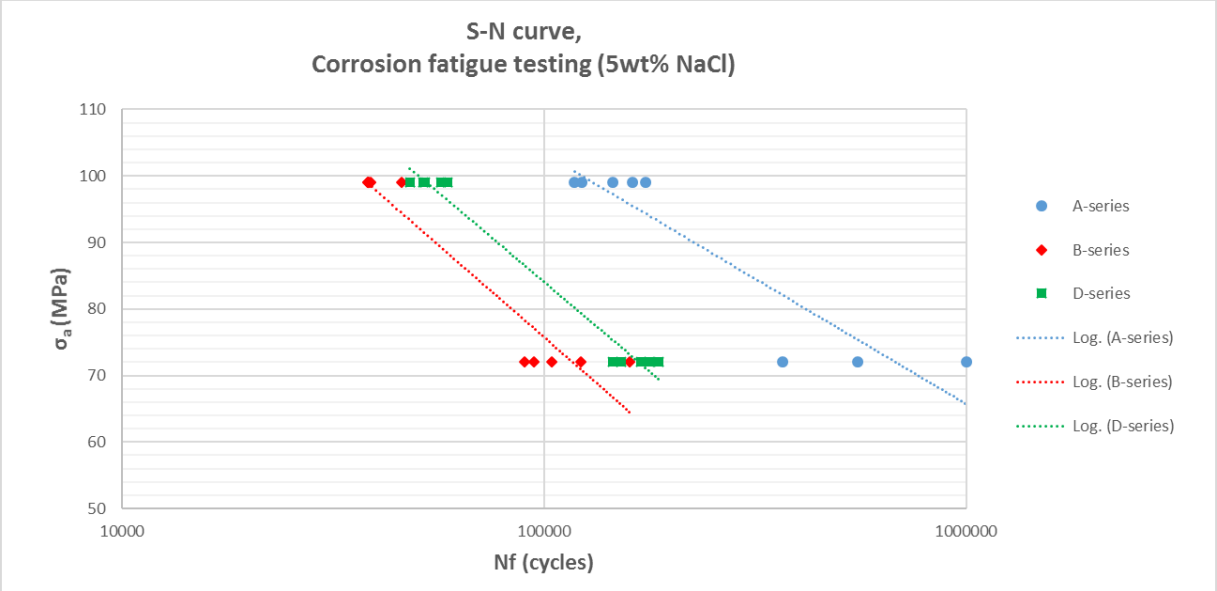

Figure 51: S-N curve for samples from each series tested in 5wt% NaCl with logarithmic trendline. Please not that Y-axis is linear, while the X-axis is logarithmic.

Figure 52 and Figure 53 you can see how the series compared in air and distilled water, respectively.

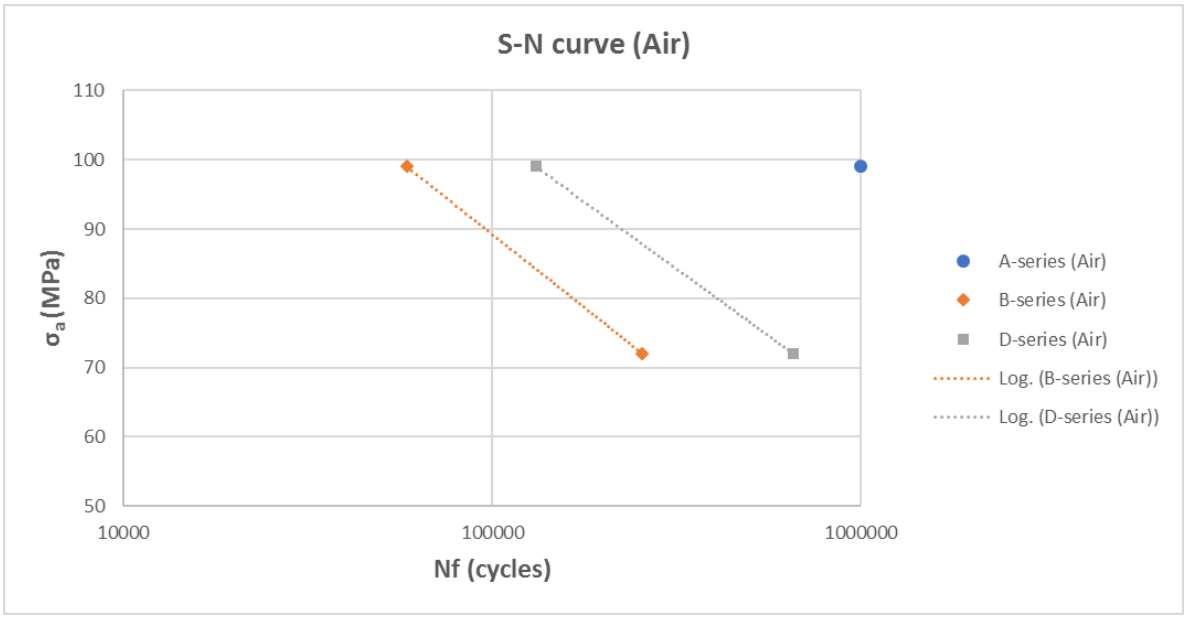

Figure 52: S-N curve for samples from each series tested in air with a logarithmic trendline.

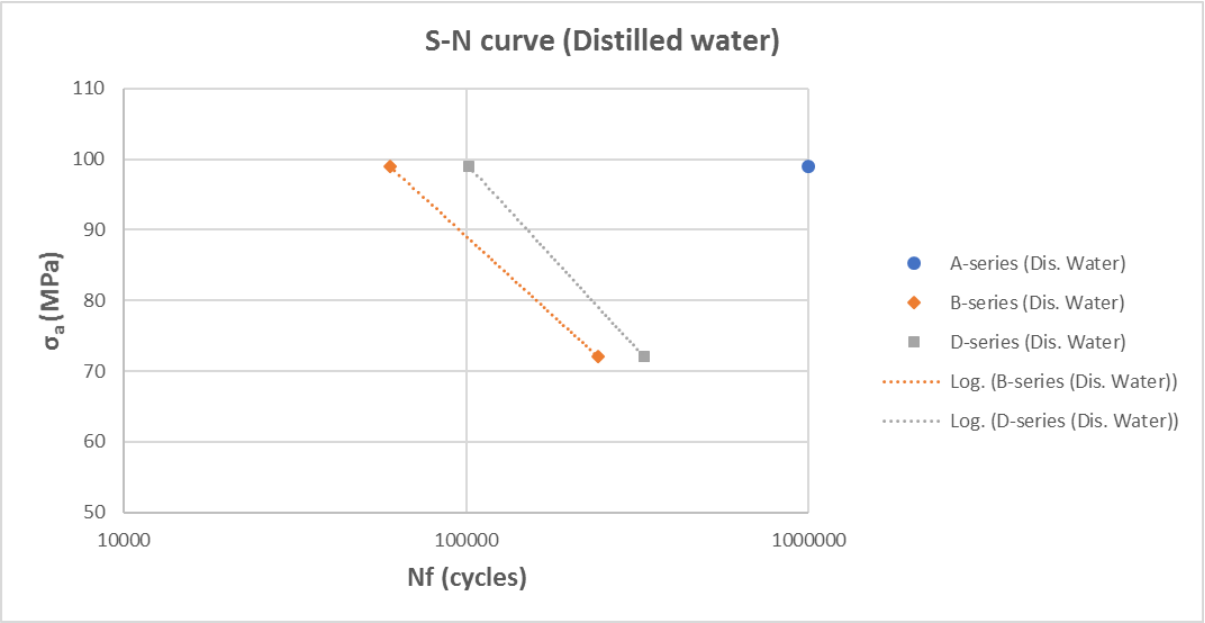

Figure 53: S-N curve for samples from each series tested in distilled water with a logarithmic trendline.

This master`s thesis is further work on a specialization project conducted by the author with the same material and samples. Figure 54 shows the S-N curve created during the specialization project. Keep in mind that these tests were all conducted in air and with R = -1. Here the C-series is also represented. It was punched like the B-series but with a different cutting clearance (0.16mm and 0.42mm for the B-series and C-series, respectively). By using SWT it was possible to estimate how the R = -1 data would behave with R = 0.1 (see 2.3.5 Smith, Watson, and Topper (SWT) equation). SWT estimates are shown in Figure 55. The stress amplitudes tested are 220MPa, 180MPa, and 160MPa. In relation to this thesis work, the maximum stress was equal to 220MPa and 160MPa just as with these samples, but the stress amplitude was 99MPa and 72MPa. The plot is log-log in Figure 54. The trendlines are linear in this log-log plot, which is a requirement for using Basquin equation.

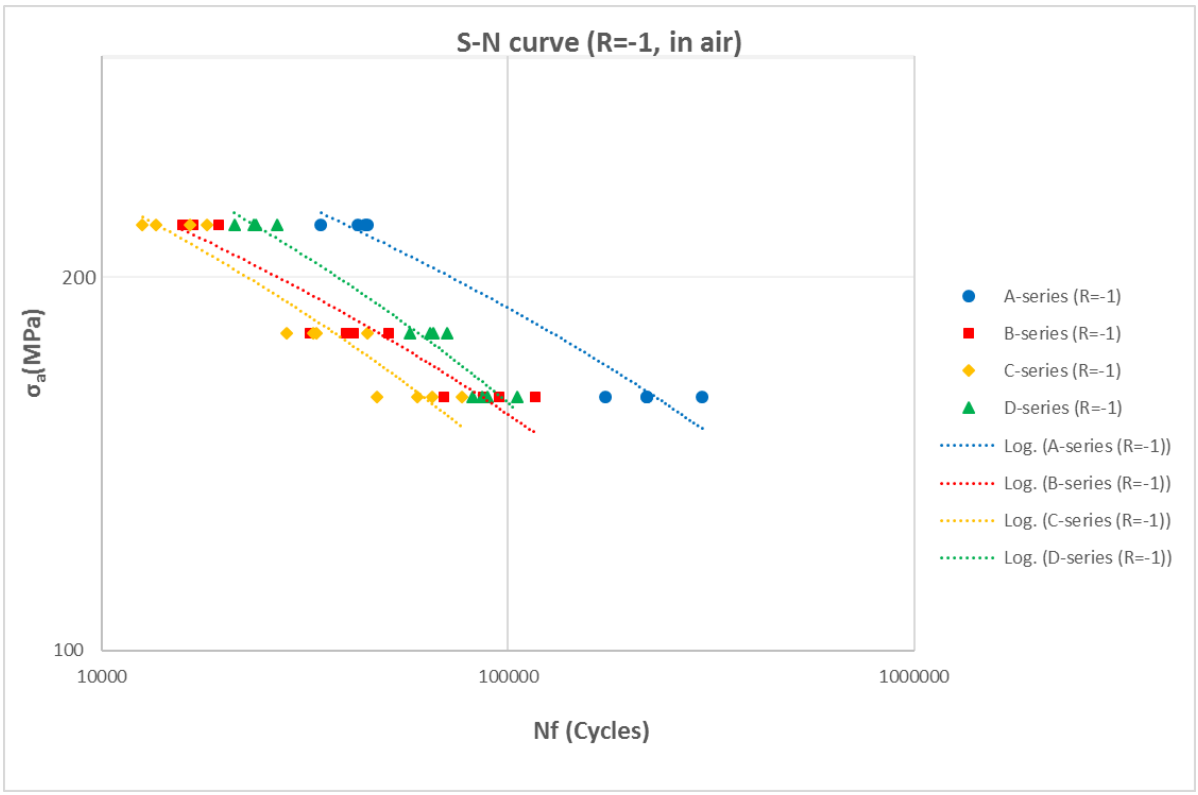

Figure 54: Results from specialization project conducted by the author. All the series are tested in air, with R = -1 and at 10hz. This graph is a log-log plot to show its linearity.

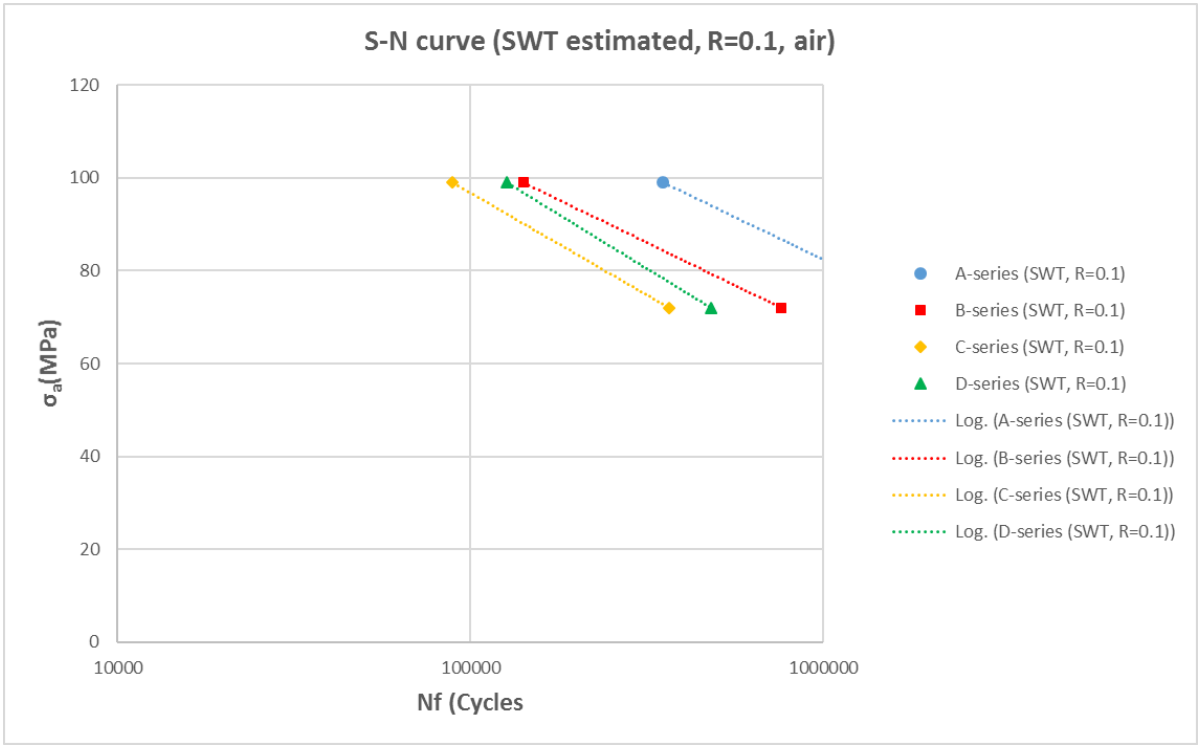

Figure 55: Estimates for fatigue life at R = 0.1 using the data from the specialization project which was tested at R = -1. Estimates calculated through SWT.

4.4.1 A-series

The A-series, which was machined, had the best fatigue life of the series tested. Samples tested in air and distilled water both reached runout at the stress amplitude equal to 99MPa, as seen in Figure 56. One sample tested in saltwater reached runout at 160MPa. A 0,3 Hz test was not run because of the time necessary to do such a test.

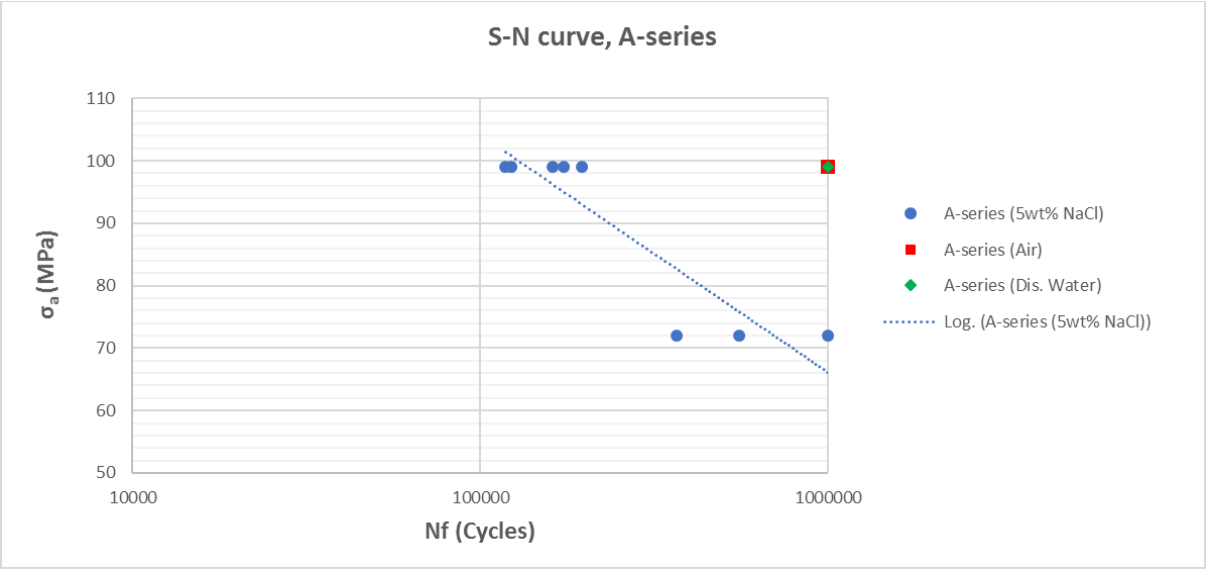

Figure 56: S-N curve for the A-series. Blue signifies the sample tested in saltwater, red and green represents tests run in air and distilled water, respectively.

4.4.2 B-series

The B-series, which was punched, showed the worst fatigue life (Nf) of the series tested. But it also had the best spread (meaning the smallest variations). Four tested samples had a fatigue life in between 38 000 and 39 000 cycles, which is remarkable similar. This is seen in Figure 57. The B-series showed no difference in samples tested in air and distilled water. The sample tested at 0,3Hz showed a very similar fatigue life to the 5Hz tested samples.

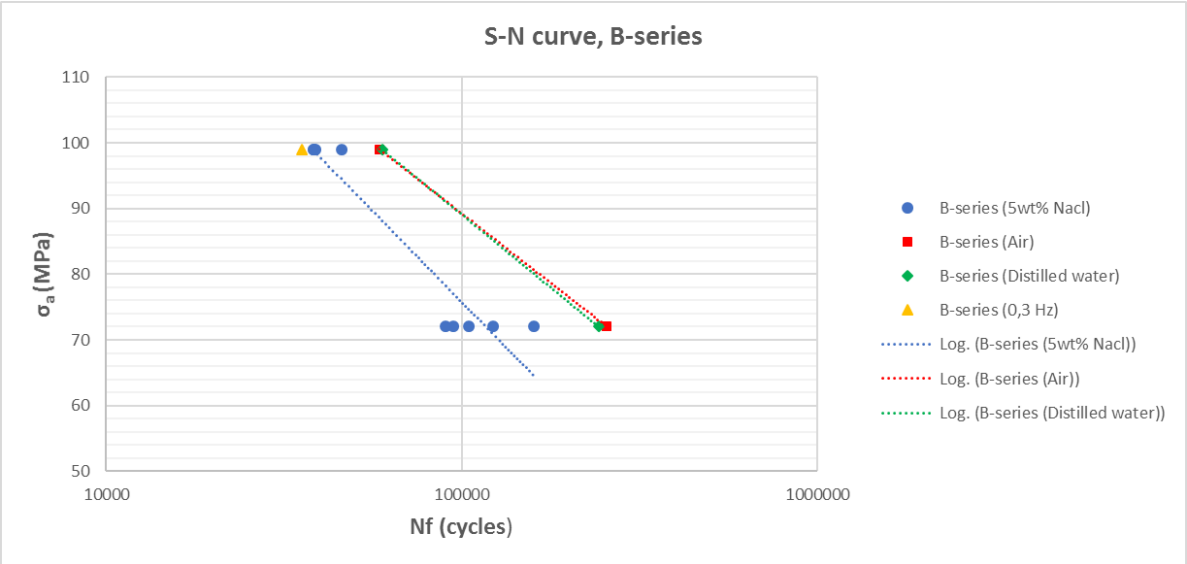

Figure 57: S-N curve for the B-series. Blue signifies the sample tested in saltwater, red, green, and yellow represents tests run in air, distilled water and at 0,3Hz, respectively.

4.4.3 D-series

The D-series, which was counter-trimmed (punched from both sides), showed improved fatigue life from the regular punched series. It is shown in Figure 58. The spread was also quite good, with reasonable similar fatigue life at both stress levels. Unlike the B-series, there was a significant difference in the sample tested in air and distilled water. The sample tested at 0,3Hz showed an improved fatigue life, even though it was submerged in the saltwater for a longer time.

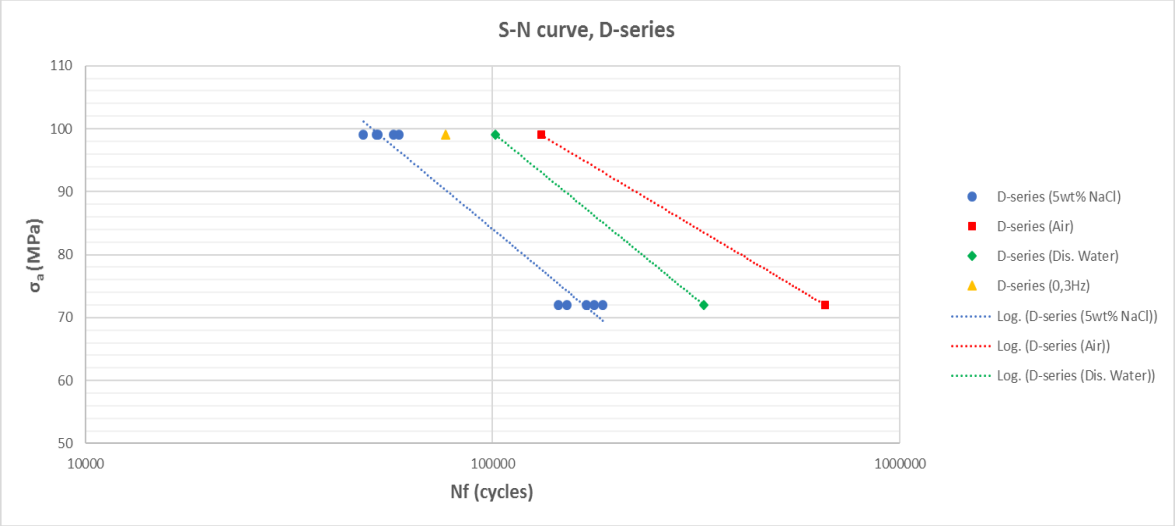

Figure 58: S-N curve for the D-series. Blue signifies the sample tested in saltwater, red, green, and yellow represents tests run in air, distilled water and at 0,3Hz, respectively.

4.4.4 Corrosion fatigue: Observations

Many samples had air bubbles stuck on the surface after pouring the saltwater in the chamber, as seen in Figure 59. These big bubbles usually disappeared during testing. The rate at which they disappeared varied. This was attributed to the flask which was used to pour saltwater in the chamber. Some small bubbles were seen on the surface late in testing as well. These were not seen in the beginning. A regular camera was not able to take pictures of them, meaning they are not shown in a figure.

Figure 59: Air bubbles on surface due to how the saltwater was poured in.

D7 was filmed in slow motion as fracture initiation was happening. Air bubbles were clearly coming from the fracture. It was possible to see the fracture grow cycle for cycle, and the fracture opening increasing for each cycle. Figure 60 shows a picture from the film. These air bubbles were tiny and new ones appeared for each cycle.

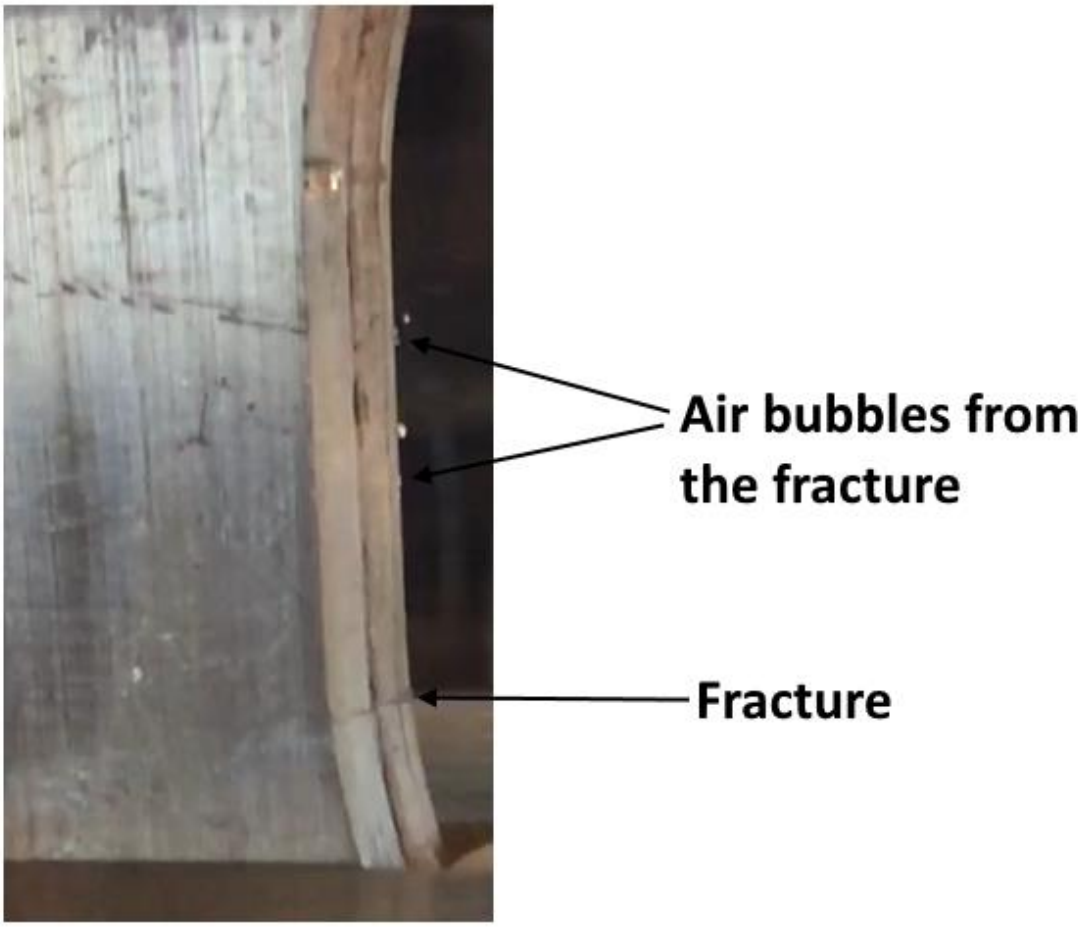

Figure 60: Showing air bubbles coming for the fracture. New bubbles appeared for each cycle.

4.5 Corrosion rate

The corrosion rates were calculated from the data shown in Figure 61. The initial weight difference is mainly due to the different sizes of the heads of the samples. Every sample was individually measured to find its specific surface area. These calculations did not take in account the rough surfaces of the B- and D-series. It assumed a smooth surface like the A-series. The corrosion rates are displayed in Table 12. The A-series stands out with a lower corrosion rate than the two others. As mentioned, the A-series has a smoother surface meaning it would have less surface area than the B- and D-series. The first five measurements, which was weighed with one day intervals, seem to be losing weight in linear manner. However, the 6^{th} measurement, which was weighed after seven days, seem to break this linearity. Both the 5^{th} and 6^{th} measurements were used to calculate two separate corrosion rates. Aluminium has a density of $2.7 g/cm^3$. The AA6082 alloy is slightly heavier, and a density of $2.71 g/cm^3$ was used for these calculations. This was based on knowledge from Benteler. Table 13 shows how the surface roughness changed for these samples.

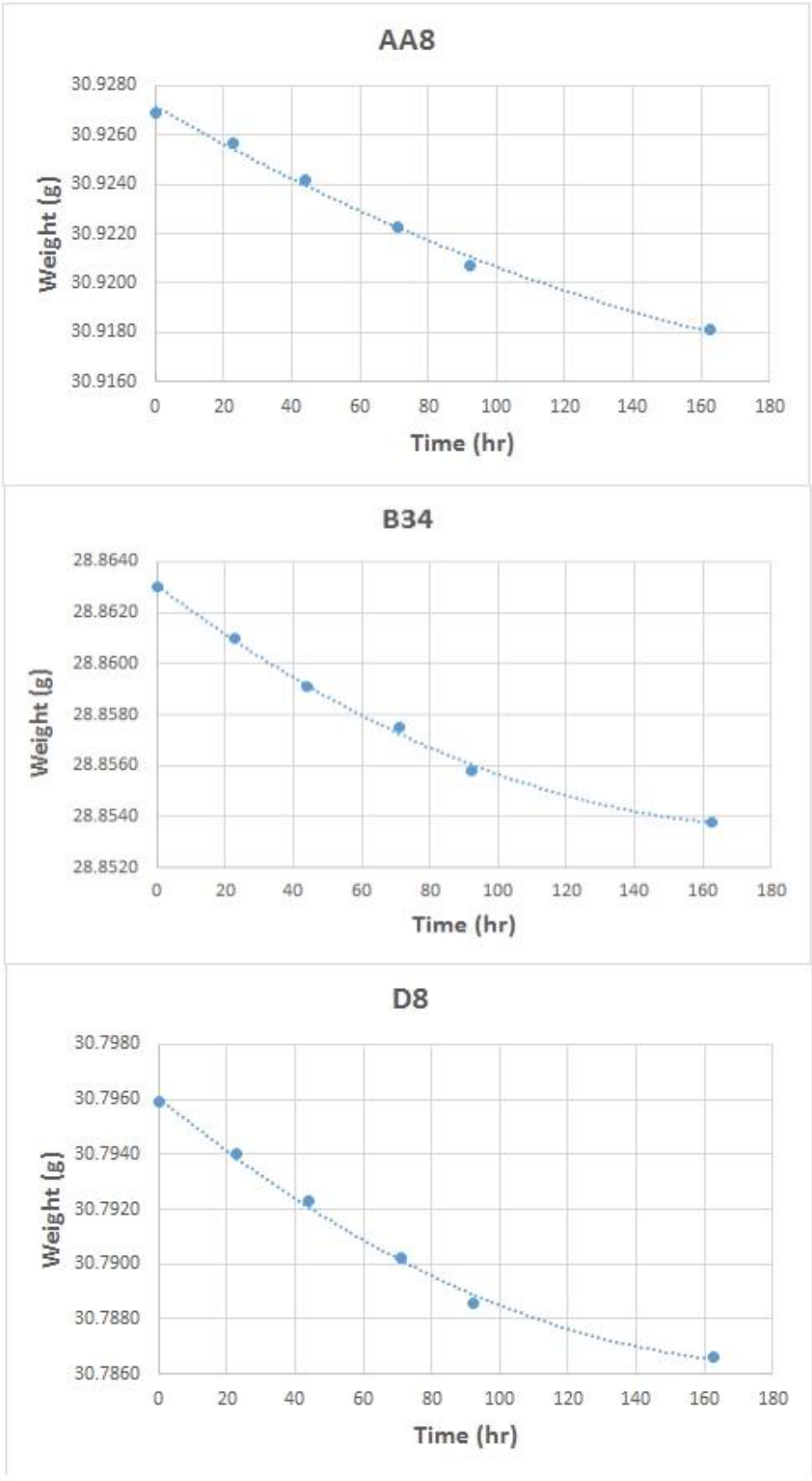

Figure 61: Weight loss due to exposure to 5wt% NaCl. The anti-static weight used had a tolerance of 0.1mg.

Table 12: Corrosion rates calculate from measured area with the assumption of smooth sides where punching occurred.

	AA8 (mm/yr)	B34 (mm/yr)	D8 (mm/yr)
Corrosion rate (linear area)	**0.0359**	**0.0428**	**0.0418**
Corrosion rate (last measurement)	**0.0289**	**0.0311**	**0.0302**

Table 13: Shows how the surface roughness values changed over one week in the saltwater. There is a general loss for all values. One value is clearly faulty; AA8 Side 1 Sz.

Before:	Ra [µm]	Rt [µm]	Rz [µm]	Rmax [µm	Rv [µm]	Rt/Rz	Sa[µm]	Sz[µm]
AA8 side 1	0.833	5.8	3	4.3	2.1	1.9	1.3	13
AA8 side 2	0.94	6.6	3	4.4	2.2	2.2	0.93	17.3
After:								
AA8 side 1	0.6129	3.3	2.3	2.9	1.5	1.4	1.4	44.9
AA8 side 2	0.8697	3.8	2.5	3.1	2.0	1.5	1.0	16.3
Before:								
B34 side 1	13	54.7	27.6	44.4	32.3	2.0	18	265.7
B34 side 2	12.2	55.3	19.1	55.3	25.6	2.9	15.8	169.2
After:								
B34 side 1	12.4	55.7	25.6	45.9	33.7	2.2	21.4	259.8
B34 side 2	12.3	54.5	19.0	54.5	25.3	2.9	16.5	168.5
Before								
D8 side 1	27.7	110.5	46.3	72.5	48.1	2.4	35.8	244
D8 side 2	30.8	121.1	54	80.2	55.5	2.2	241.9	481
After								
D8 side 1	27.4	107.8	44.9	67.8	45.8	2.4	29.1	221.8
D8 side 2	30.7	118.4	53.5	79.5	52.9	2.2	241.7	470.7

4.6 Fractography

Every series had four samples which were tested in saltwater investigated in SEM. Two samples which were fatigue tested with a stress amplitude equal to 99MPa and two at 72MPa. Some additional samples were investigated; two which were tested in air and one which was removed immediately after fracture initiation.

Because of the unpredictability of fatigue, the time from fracture initiation until removal of the sample from the saltwater is undetermined for most of the samples. The amount of corrosion may therefore vary from sample to sample. A sample (D7) which was immediately removed after fracture, was therefore studied. Fracture initiation were believed to be found for every sample. All overview micrographs in SEM were taken at 8x and three extra micrographs were taken at the fracture initiation site at 50x, 200x and 600x. Further enhancement did in general not give any further information. Some extra micrographs were taken to show specific characteristics of the fracture when suitable. Appendix C: SEM micrographs shows more micrographs from all series.

4.6.1 A-series (SEM)

The A-series had without exception, in the four samples studied, fracture initiation in a corner. A corner being where the machined side (which would otherwise be punched) and the top or

bottom (extruded surface) of the sample meet. For this series, the overview micrograph as shown in Figure 62, proved the most useful as it had clear beachmarks indicating the corner. Further enhancement did show some fracture propagation lines, as seen in Figure 63. Figure 64 shows some effects the corrosive environment could have on the A-series.

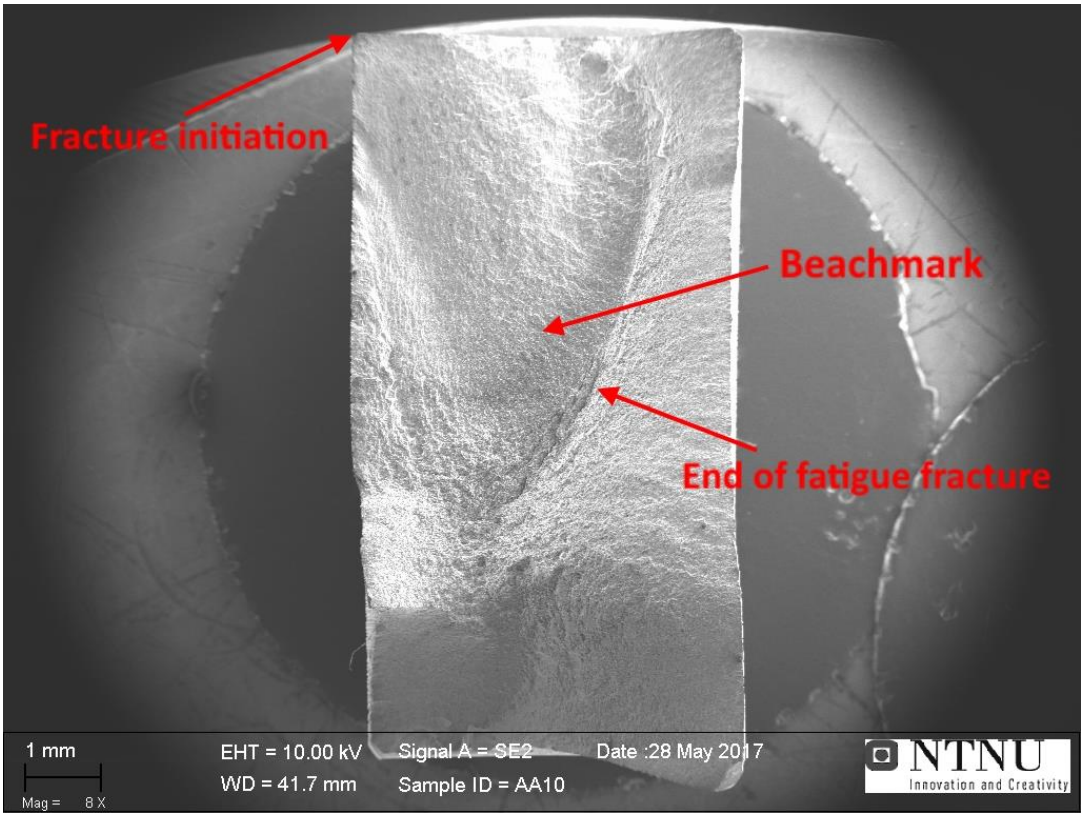

Figure 62: Overview micrograph of AA10 (σ_a = 99MPa) with arrows showing a beachmark, fracture initiation and end of fatigue fracture.

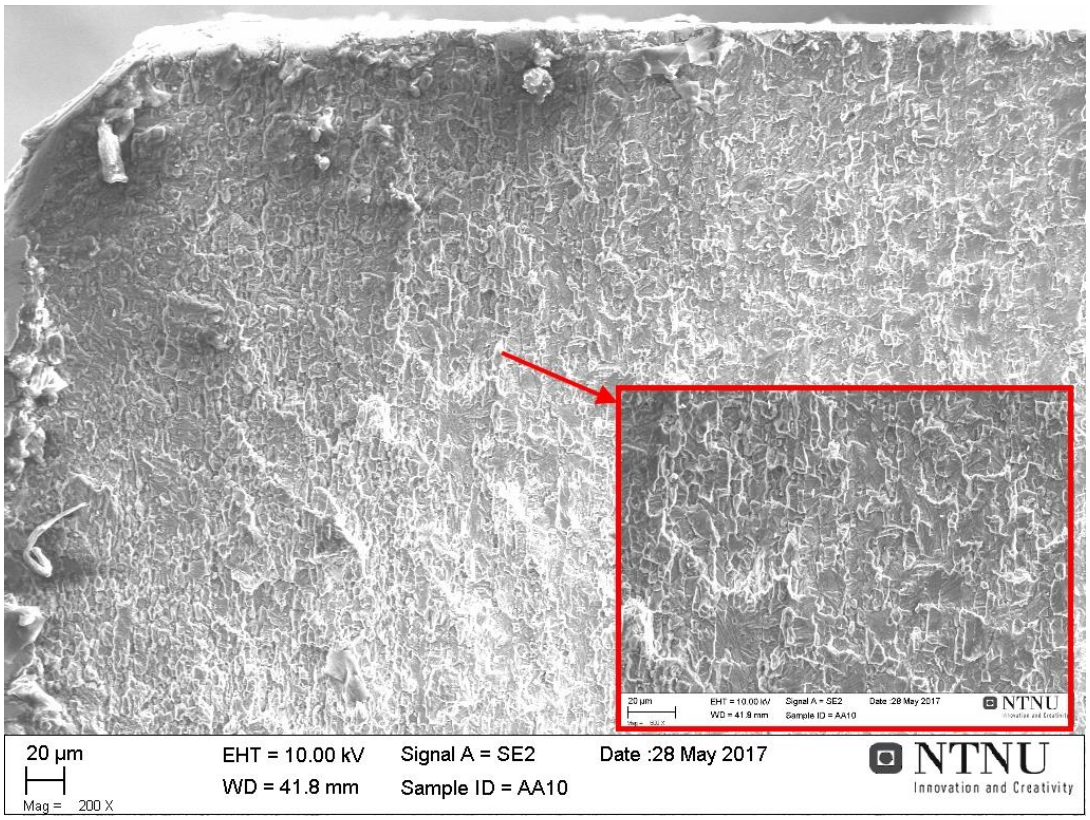

Figure 63: 200x and 600x of fracture initiation site of sample AA10 (σ_a = 99MPa).

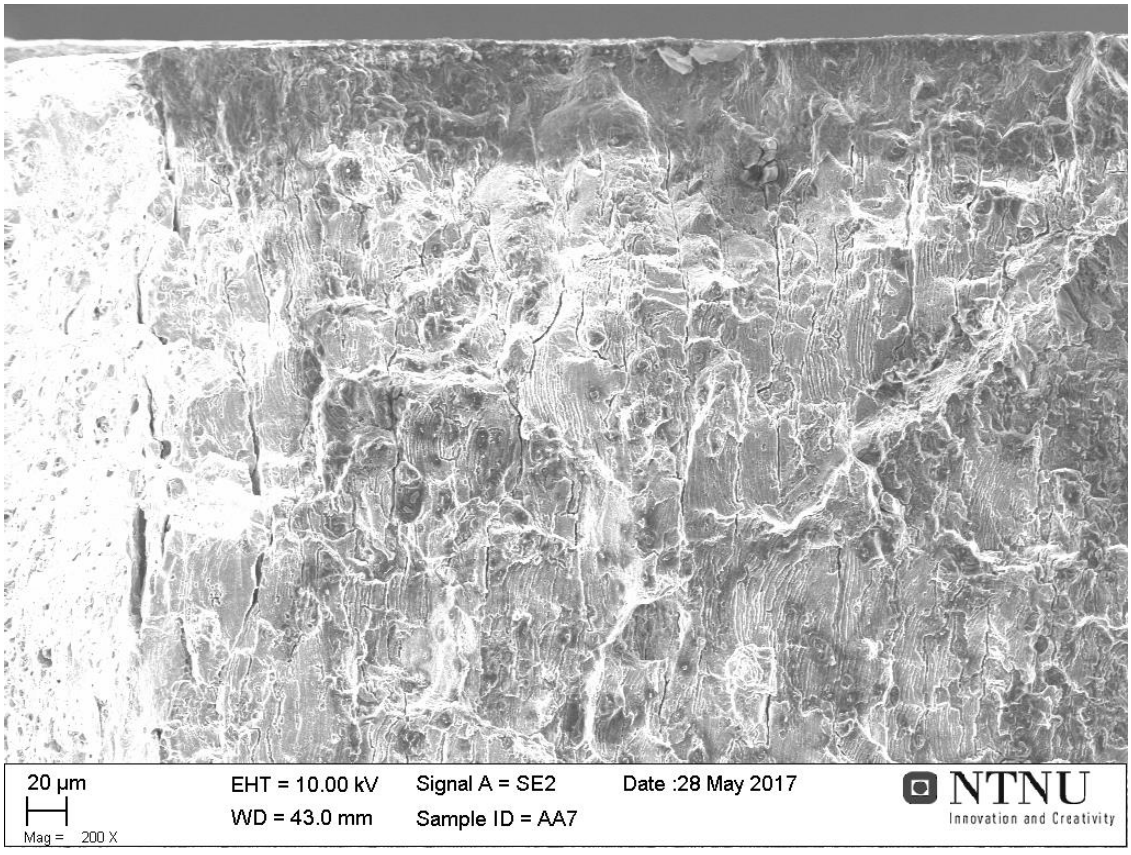

Figure 64: 200x micrograph of AA7 (σ_a = 99MPa). This is taken towards the end of the fatigue fracture zone. It shows the grain boundaries which have been corroded making them visible. It also shows fatigue fracture propagation lines towards the right where fracture initiation was found.

4.6.2 B-series (SEM)

The micrographs of this series all indicate a fracture initiation originating either from or close to, the wound created during punching. B14 has been taken as an example. This sample was tested with a stress amplitude equal to 72MPa. B14 is shown in Figure 65 and Figure 66. The other samples had similar fractures. The grain structure is quite clear at higher magnifications. It is important not to confuse these with crack propagation lines or striations. The crack propagation lines are seen within the grains. Figure 67 shows a sample tested in air. Here the grain structure is not nearly as visible. Figure 68 shows a different sample, and how visible the grain structure could be become (look Figure 36 for comparison).

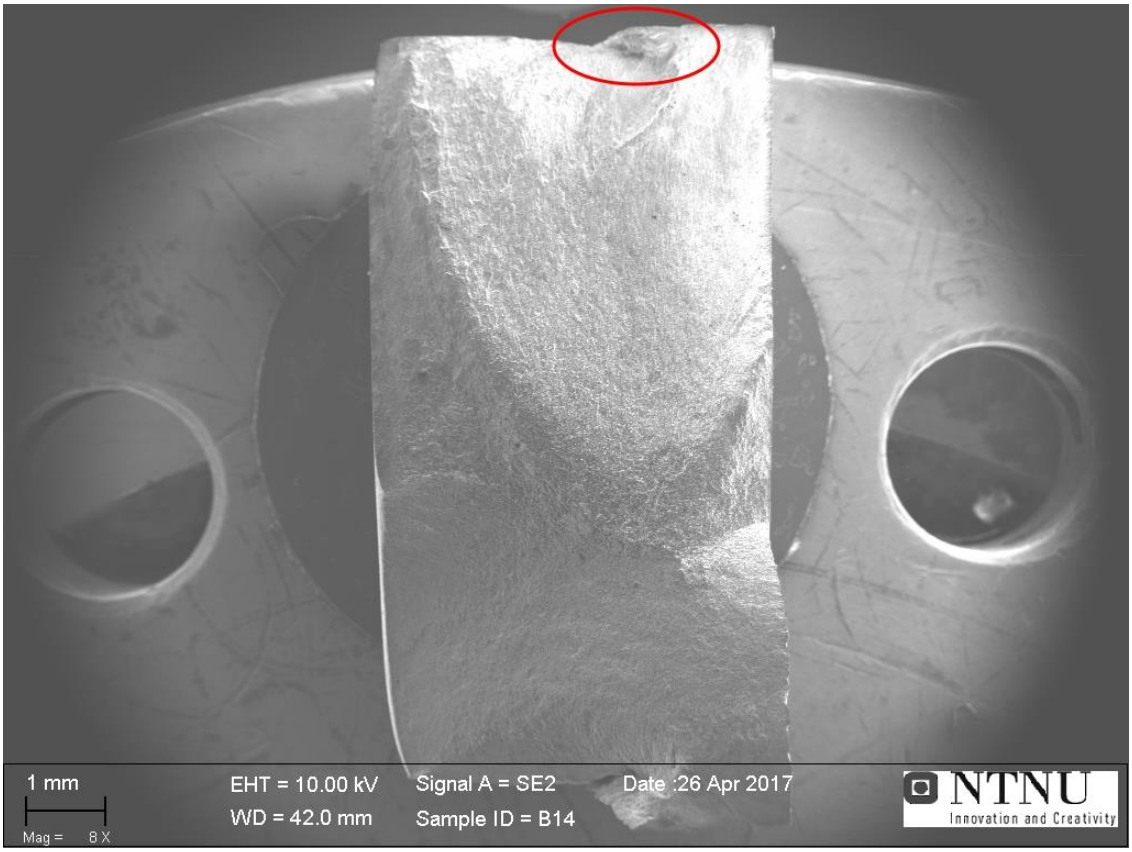

Figure 65: Overview micrograph of B14 (σ_a = 72MPa).

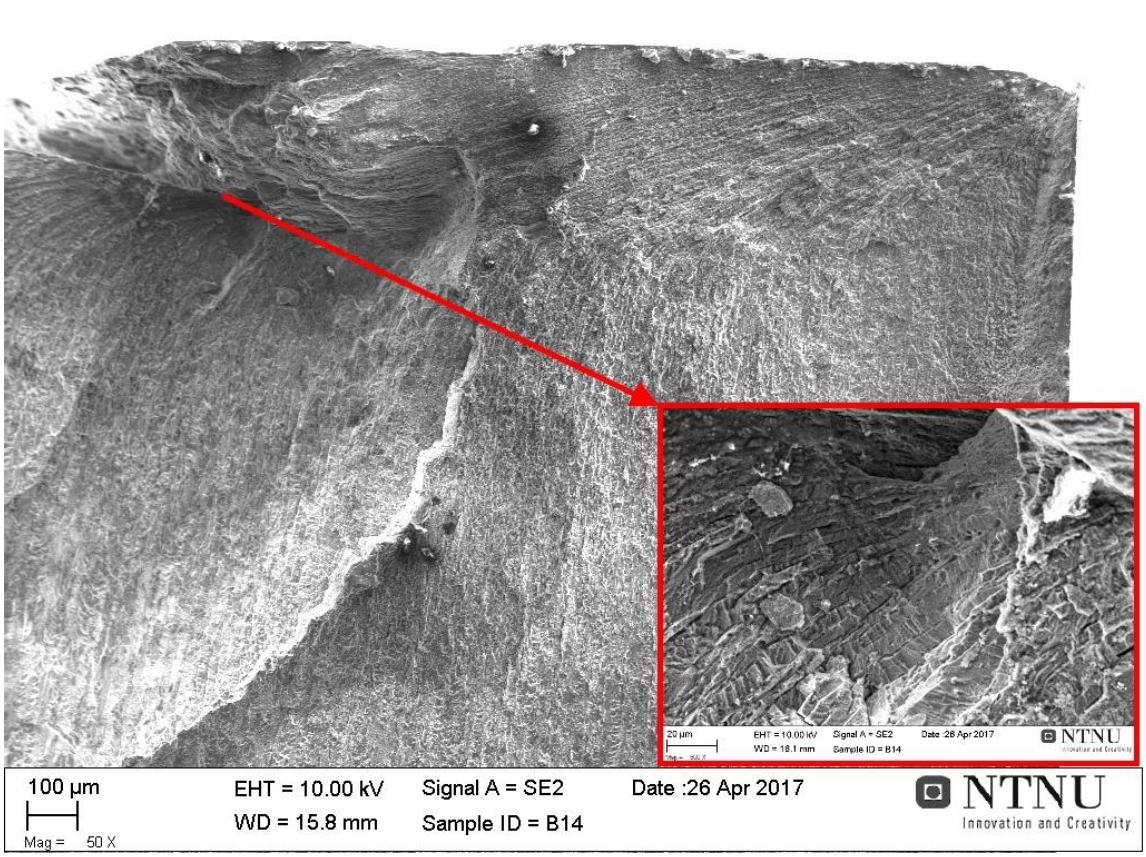

Figure 66: 50x micrograph of the fracture initiation site of B14 (σ_a = 72MPa). And a 600x enhancement showing fracture propagation lines.

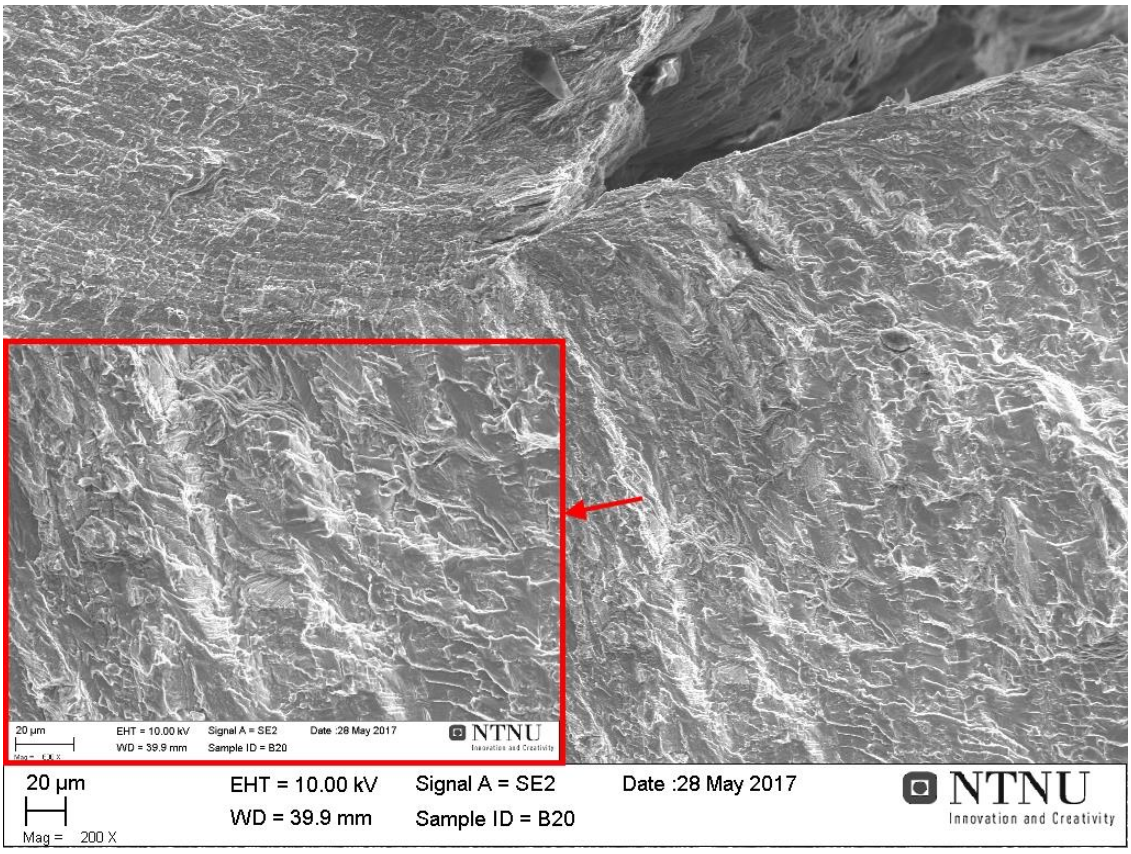

Figure 67: Micrograph at 200x and one part enhanced to 600x of sample B20 (σ_a = 99MPa). B20 was tested in air.

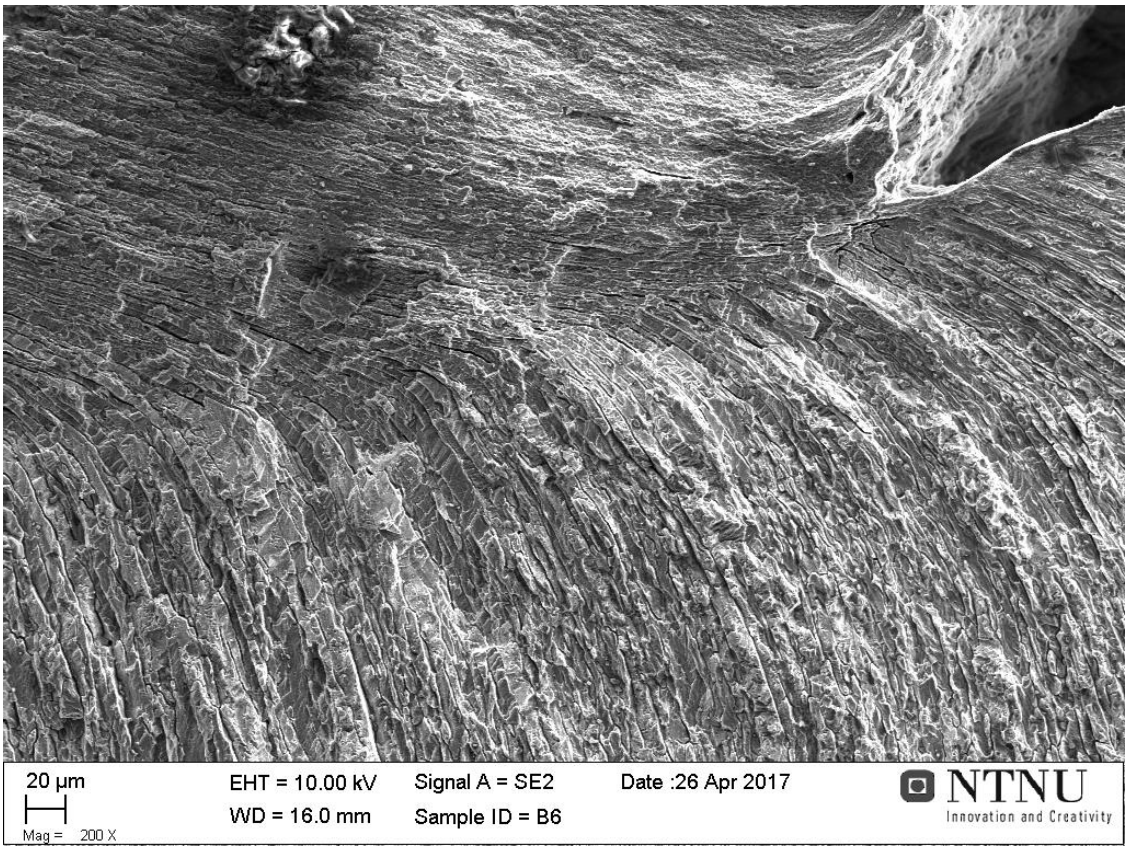

Figure 68: Micrograph at 200x of B6 (σ_a = 72MPa). Here the grain structure is very apparent. Fracture propagation lines can be seen within the grains.

4.6.3 D-series (SEM)

The D-series also showed fracture initiation either at the wound or the surrounding area. Figure 69 shows an overview micrograph of D24. There are quite clear beachmarks below this circle, which are originating from the marked area. Enhancements of the fracture initiation site showing the crack propagation lines, are shown in Figure 70. Further enhancement proved to not give any further details as the corrosion had deeply affected the fractured surface. Figure 72 show a sample which was immediately removed from the corrosive environment after fracture initiation. Figure 72 displays a D-series sample tested in air.

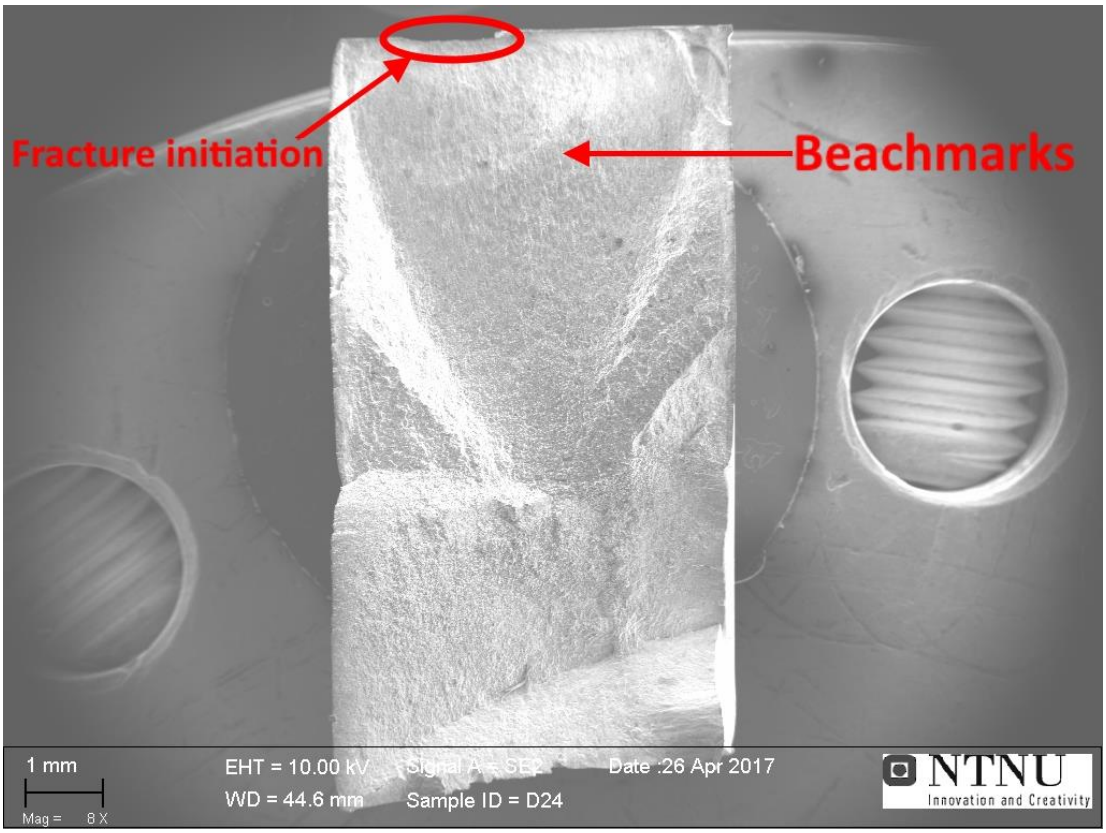

Figure 69: Overview micrograph of D24 (σa= 72 MPa). The red circle indicates the fracture initiation area.

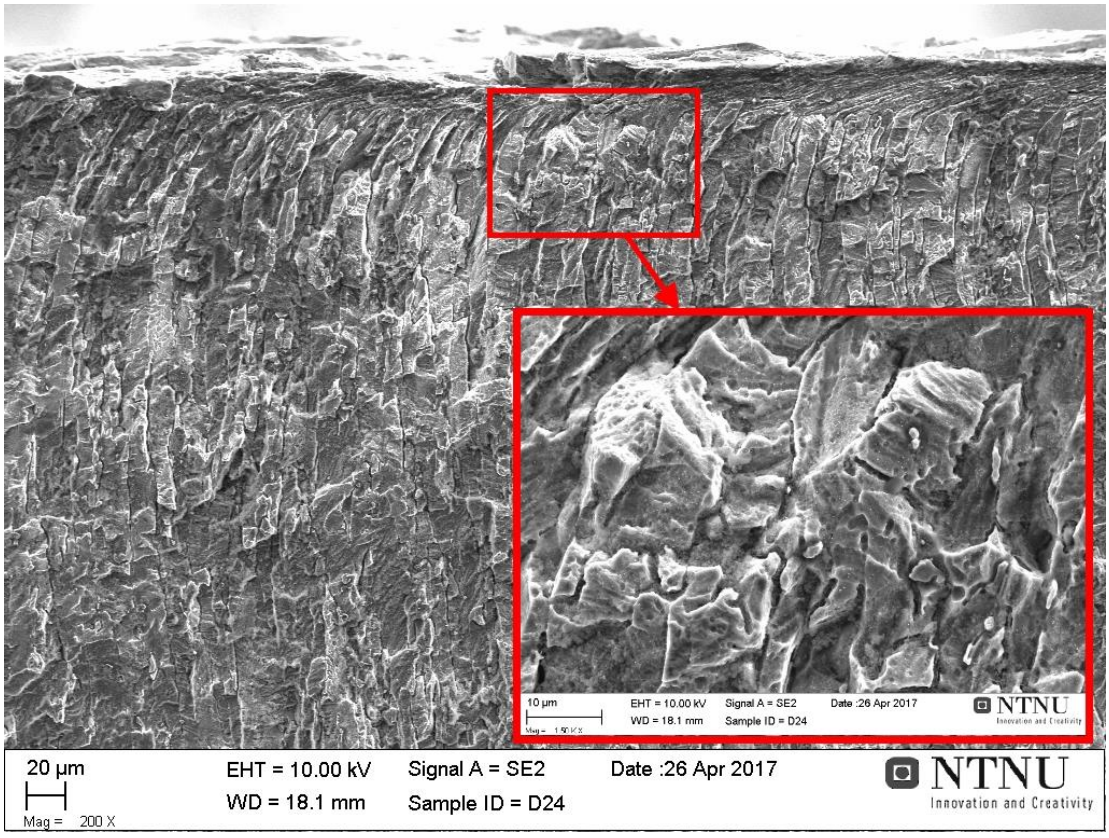

Figure 70: Fracture initiation site for D24 (σ_a = 72MPa) with an enhanced area (1500x) of crack propagation lines clearly originating from the punched surface.

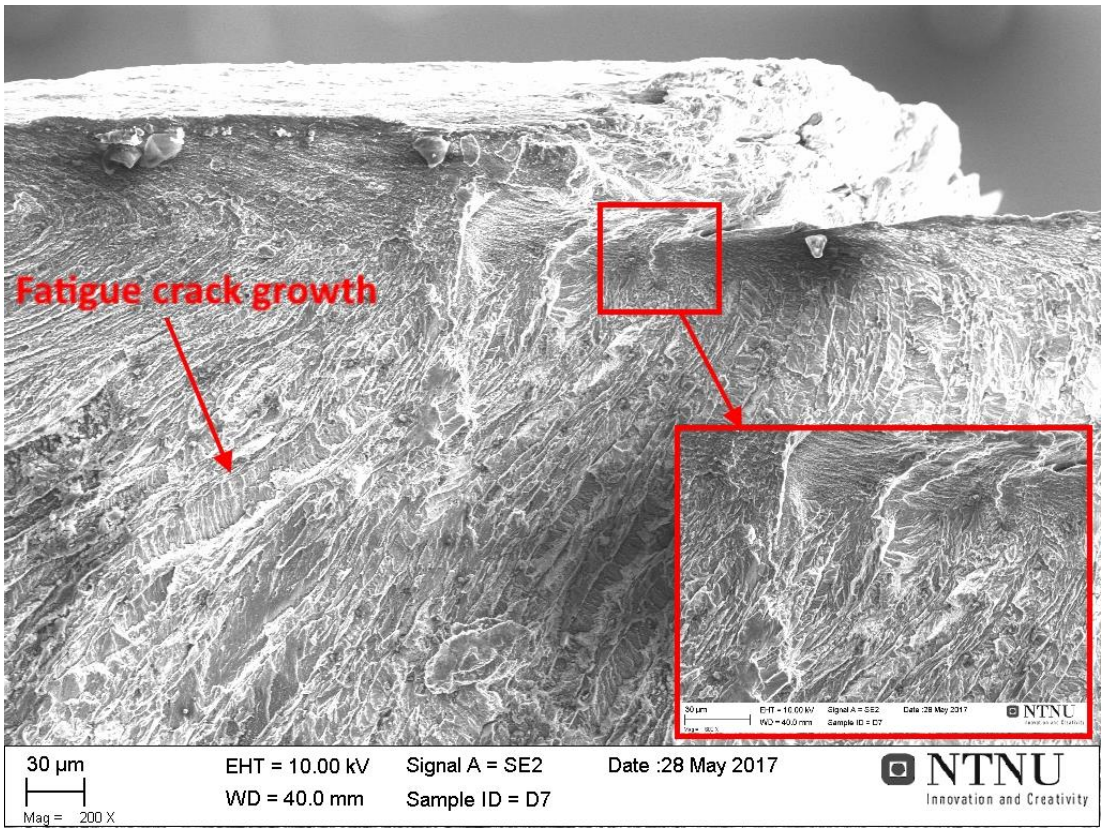

Figure 71: A 200x and 600x micrograph of D (σ_a = 99MPa) which was removed immediately after fracture initiation.

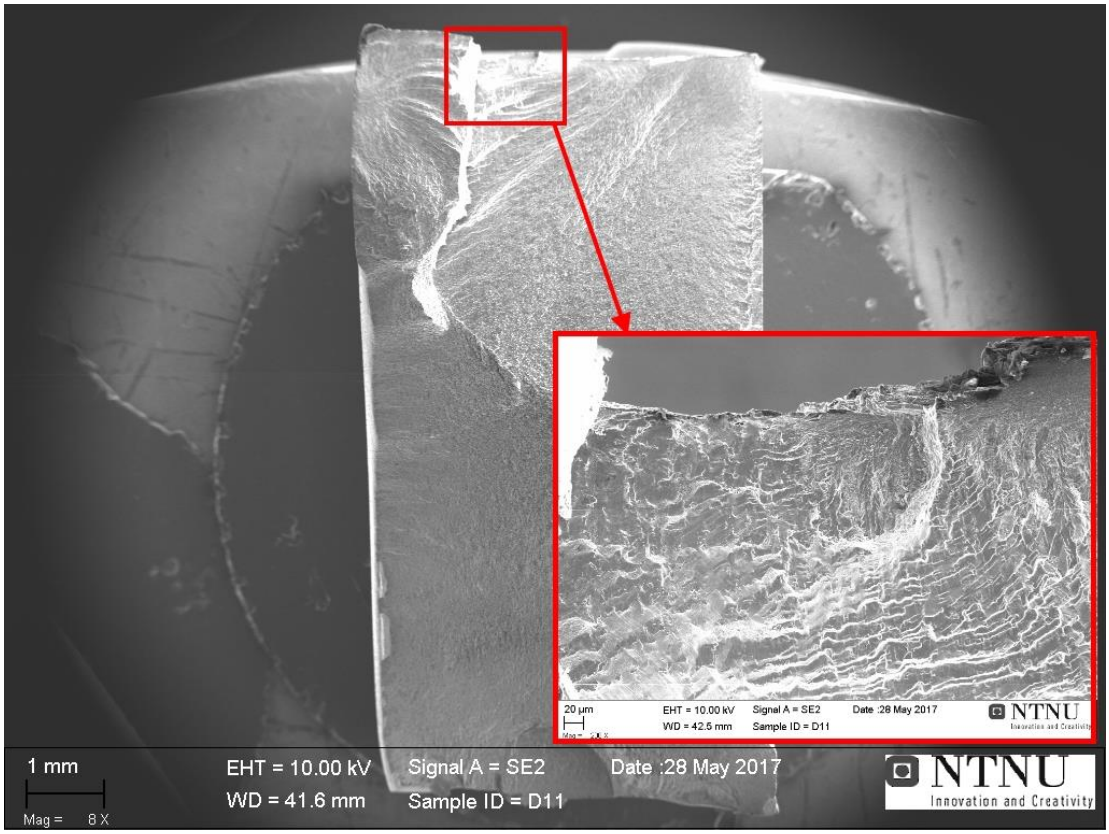

Figure 72: 8x and 200x micrographs of D11 (σ_a = 99MPa) which was tested in air. The fracture initiation site is the part which is enhanced.

4.7 Artificial Ageing curve at 180°C

The initial goal with performing these tests were to find T6 and T7. Then performing fatigue tests at these temper states. Time did not allow for these fatigue tests to be performed. This ageing curve is therefore rather irrelevant. This is because every other sample tested in fatigue was artificial aged at 140-150°C. Also, there were some complications with some tests which should have been retested. Once again, time did not allow for retesting. These results are therefore given in the Appendix E: Artificial ageing curve at 180°C.

4.8 Temperature and humidity

The temperature in the water surrounding the samples tested in corrosion fatigue was checked to see if it increased during testing. This test was done in distilled water and not saltwater. Thermometer used was an *Omega HH1384 datalogger thermometer*. Table 14 shows the results. Please note the long time between measurement five and six. The bottle with distilled water was measured to be at 23.1°C. T(reference) was an extra thermometer in the room used to doublecheck these results. Temperature in the chamber and in the room, appear to be approximately the same after a long period of time.

Table 14: Temperature measurements in chamber compared to room. Sample was tested at 5Hz, R = 0.1, σa = 99MPa, and σmax = 220MPa. T(reference) is measured by a thermostat in the room.

N(cycles)	T(chamber) (°C)	T(room) (°C)	T(reference) (°C)
45000	23.2	23.8	24.2
56000	23.5	23.4	24.1
62000	23.7	23.7	24.1
70000	23.8	23.7	24.3
78000	23.9	23.7	24.3
320000	25.0	24.1	24.4
360000	24.6	24.0	24.7
400000	25.0	24.6	24.7

Another device called; *USB Temperature and Humidity Data Logger*, was used to measure the relative humidity and temperature over time in the laboratory. This data logger took a measurement every 30min for the whole testing time. This graph can be seen in Figure 92. Table 22 shows the humidity for the samples tested in air. Both can be found in the Appendix F: Temperature and humidity.

5. Discussion

This chapter will concern itself with evaluating the experimental results. Both theory and observations will be taken in consideration. It will be divided into three sections with different focuses: Topography and surface roughness, corrosion fatigue results, and fractography. They will overlap, as they are all relevant for each other. Error sources will be discussed in the end.

The aim of this study was to investigate the corrosion fatigue properties of AA6082, which were shaped through machining, punching, and counter trimming. The difference seen in the experimental results will be the focus of this discussion. This discussion will also try to relate these results to how the punching process can be improved with regard to fatigue life.

Understanding of how and why high cycle fatigue fracture initiate is important in order to improve fatigue life. This study has considered the topography, fractography, fatigue life (S-N curves), corrosion rate, grain structure, and surface roughness of the different shaped samples to understand this phenomenon.

5.1 Topography and surface roughness

While studying the surface roughness there are several values which are used. Some common values are: Ra, Rt and Rz (see Table 3 for definitions). However, using the basic concept of fatigue fracture initiation, the value Rv (maximum valley height of roughness profile) seem to be the most relevant. The basic concept of fatigue fracture initiation is that it is a weak spot phenomenon. Studying this value, you could predict the fracture side quite accurately. This will be discussed in this section. Rmax (maximum peak to valley height of roughness profile within a sampling length) also does seem to be quite relevant for fracture initiation, but would be inaccurate for the D-series which showed peaks in the middle of the sample. Rv is not seen much in literature, so any comparisons are hard to make.

The areal roughness (Sa and Sz) will not be discussed to any detail in this work. This value was simply added because the Alicona manual claimed this was the future within surface roughness measurements. It is not commonly used yet. By adding the value, it could therefore be relevant for any further work which uses the data in this study.

The A-series

Looking at the primary profile in Figure 39 you can see how very small the variations are in this series. The surface varies over a mere 5µm in height. Using Table 7, you can see that the average for every value is very small, especially compared to the other two series. Rt, Rz, Ra, and Rv are: 4.9µm, 3.0µm, 0.658µm, 2.1µm respectively. The same alloy in another study, was found to have the following values on an extruded surface: 11µm, 8 µm, and 2µm for Rt, Rz, and Ra, respectively [8]. This is the main explanation to why the A-series has such a superior fatigue life. Rv had an average of 2.1µm with a standard deviation of 0.9.

Figure 40 shows a more detailed height difference in a section of the test area. A pattern is clearly visible; a square-net like pattern. This is due to the machining process. Though this looks severe because of major color difference, keep in mind that green signify +1µm and purple -2.5µm. This has a general effect on the fatigue life. But remember that the fractography of the A-series showed that initiation was at a corner. The corner, being between

the extruded and machined edge, is the weak link in this series. It would also be the most exposed spot for corrosion, considering the corrosive medium would come from both sides. The machined surface would be so flat that there would practically no increase in corrosion exposure due to surface roughness. As shown through the empirical data collected in this thesis, this series also has the greatest difference in fatigue results. This is probably because the machining can create a single small notch at this corner. Even though the rest might be prefect, a single notch would be a weakened fracture initiation site and thus ruin the samples potential fatigue life. The presence of small notches or defects on the corner determines the fatigue life of this series. Presence and severity of notches varies greatly from sample to sample. Thus, fatigue life varies from sample to sample.

B-series

Figure 41 shows a single sample from the B-series. This sample alone shows two very different topographies. The punching parameters are clearly not perfect. The two wounds you see in B15 side 1 is probably due to a fracture beginning at the punch and one at the hold. Theory suggests that when the parameters are optimized these two fractures should match up creating one continuous fracture. A close to optimized punched surface is shown in B15 side 2. The bottom part of this side is correct, though it still has some small wounds which should be avoided. Not unexpectedly, fracture occurred at side 1 in this sample. This can be seen in Figure 44, where the fracture propagation path is recreated.

Looking at Table 8, you can see how 8 out of 10 samples had fracture on the side with the highest Rv value. As mentioned in the introduction to this section, this seems to be the most relevant value for fatigue fracture initiation. This is especially true, if you just consider a deep valley as the beginning of a crack already present before testing. This is a weak spot. That is what Rv measures; the crack already present (in a way). Now let us study these two samples which do not follow this trend. B14 is one. Here both values are well above the average Rv value (83.7μm). Side 1 has 146.3 μm and side two, where fracture occurred, has 122.9μm. With such high values for Rv it means that both sides are accommodating for fracture initiation.

The other sample, B26 has a low value where the other is significantly bigger in comparison. B26 side 1 had Rv equal to 78.4μm and B26 side 2, where fracture occurred, had 41.8μm. Studying the profiles and topography for these two sides, the reason to why this fractured on the other side cannot be explained by measurements performed. Do remember that the wounds might go far deeper than what the machine registered. There also many other factors taking part. Profiles of this sample can be seen in Appendix A: Topography. If we accept the B14 explanation, the Rv-prediction holds true for 90% of the samples.

D-series

Figure 46 shows sample D2 from the D-series. Just like the B-series, this series show two very different sides on one single sample. Keep in mind that this series was counter trimmed. Studying the D2 side 1 it is possible to determine the punching directions. The initial punch was upwards (in relation to Figure 46) and the secondary punch was downwards. Looking at Figure 47 which shows the profiles, you can see how the top part of D2 is relatively flat. Therefore, it must be the starting point for the secondary punch. Looking at the B-series

surface there is always a flat area like this one where the punch starts. Using theory of how a punched surface should look (2.4 Punching) it is evident that the punch which was performed last would get this flat side. This is because it is the punch which had the tightest dimensions.

The area which is squeezed upwards in the middle almost reach an altitude of +50μm in comparison to the local reference plane. Which is the flat area. To explain how this peak was created, let us use the regular punched surface shown in Figure 41. Imagine that after the first punch, D2 side 1, looked like B15 side 1. Now the punching direction for B15 side 1 is downwards in relation to the picture. This means that the next punch would go upwards for it to be counter trimmed. This second punch has new parameters which punches to a slightly tighter dimension than the first punch. The end of the wound is not only work hardened, but also in an incline. Both factors make it more likely for the punch to go over the wound. This creates circumstances which allows for peaks.

Side two, which quite fittingly, probably comes from a similar side to B15 side 2. It could be explained by imagining that the new parameters of the second punch would be sufficient to reach the lowest part of the fractured zone. It would then rip off the surface like a regular punch and overcome the work hardened surface.

Once again, the Rv value proves the most useful to predict which side will have fracture initiation. The values are close to the half of what it was for the B-series. Table 10 shows that 8 out of 10 samples had fracture on the side with the highest Rv value. The samples which deviate are D7 and D24. D7 has 0.3μm difference in Rv, meaning there is practically no difference between the sides. Remember that the vertical resolution is 0.1μm, meaning that this difference is on the limit of what the scan can distinguish.

D24 however, has side 1 where fracture occurred with Rv equal to 51.1μm and the other 58.1μm. These are also quite similar. In Figure 73 you can see the primary profiles of D24. Looking how the surfaces varied from side to side you can see a similar shape to the one shown of D2. Looking at these two surface profiles, side 1 might have a lower Rv value but the shape of it is much more rugged and chances of local stress concentrations are greater than with the type of profile we see on side 2. The increased Rv value probably comes due to a higher total height difference. In the primary profile for side 2, it is a gradually descending height which appears rather smooth. Do keep in mind that these profiles are the average of 2000 measurements. If we except both explanations, then the Rv-prediction would hold true a 100% of the time for the D-series.

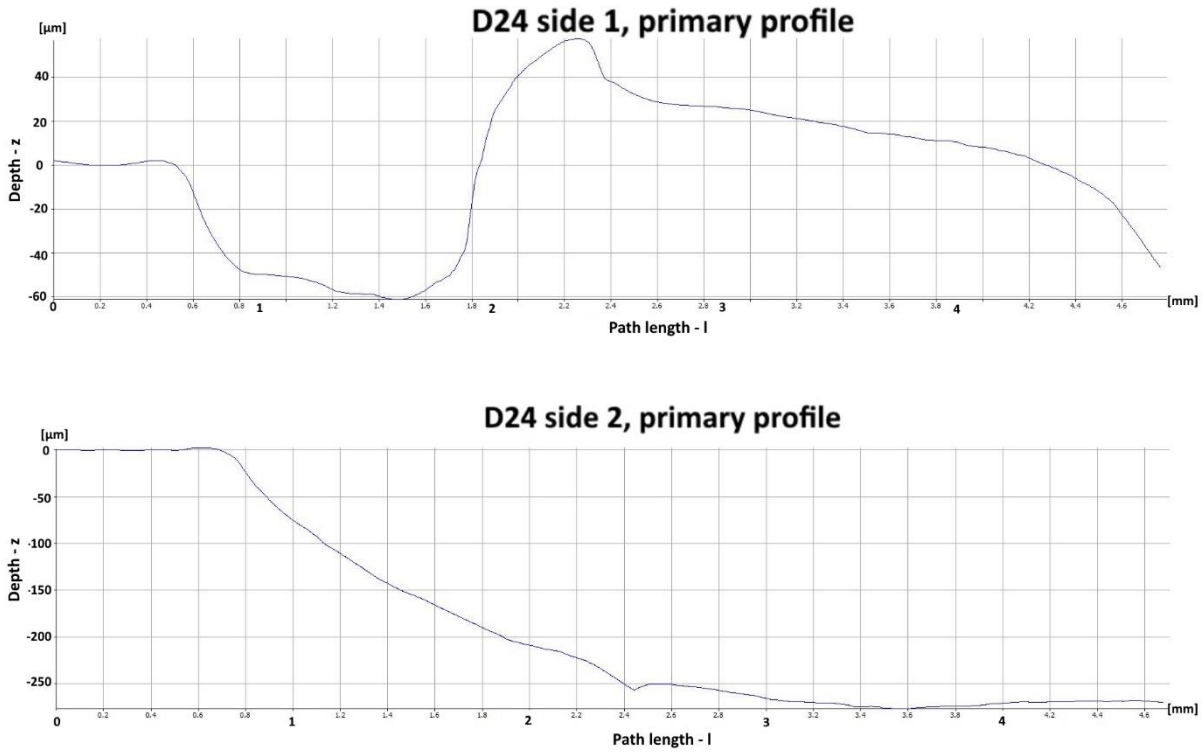

Figure 73: Primary profiles of sample D24. Fracture occurred at side 1, the top graph.

Local fracture path

Table 9 and Table 11 show the surface roughness where the cracks were recreated. These yielded no definitive result. The difference in Rv is sometimes close to zero, sometimes highly positive, and sometimes highly negative. There is no pattern which emerged. The fact that Rv proved so helpful predicting the side, but does not show a local increase where the fracture propagated, can be explained rather simply. An average of a whole side tells you how it compares to the other side on a general level. Thus, the side with the highest Rv value will have a greater chance of having an accommodating fracture initiation site. But the specific location where the fracture will initiate cannot be determined so easily. It could be a deeper wound than registered (see Figure 23), or more exposed to corrosion, a material defect, just to mention a few reasons why it could fail at the exact spot.

Rv vs Nf (fatigue life)

To study this, the Rv found for the side which had fracture was used. This was plotted against the fatigue life of that sample. The results are shown in Figure 45 and Figure 50. It appears to be no direct correlation between fatigue life and the Rv value. As with the local fracture path, this is probably because the fracture process is so complex. There are many variables determining the fatigue life and Rv alone cannot predict it. In Appendix A: Topography, you can see Ra/Rt/Rz vs Nf as well. None of which gave any conclusive link between the two.

Using the corrosion rate to calculate surface deformation

The difference in corrosion rates were used to calculate the amount of deformation that occurred due to punching. First the A-series was assumed to have the correct corrosion rate. Then how much weight was lost due to everything but the punched/machined surface with the

A-series was calculated. This gram lost per area from the A-series was applied to every surface, except the punched surfaces, for the B- and the D-series. Then we can find out how much extra area the punched surfaces must have created to compensate for the increase in corrosion rate. Table 15 shows the calculations correcting for the increase in area due to punched surfaces.

It shows that the B- and the D-series have its punched surface area increased by 2.55 and 2.41 times the corresponding machined surface of the A-series. This is a huge deformation that has occurred for such an increase in surface to occur. This corresponds well with the pictures and profiles of these two series. The new corrosion rates all seem to be rather similar, which it should be. After all, it is the same material and the corrosion resistance should be the same.

Table 15: Calculations of increased new surface due to punching. A, WL, O, and P stands for: Area, Weight Loss, Other than punched surfaces, and Punched surfaces, respectively.

Subject	**AA8**	**B34**	**D8**	**Units**
A(Total from measurements)	**6041.09**	**5888.05**	**6109.78**	**mm^2**
A(P)	553.22	554.42	554.42	mm^2
A(P)	0.0005532	0.0005544	0.0005544	m^2
A(P)	9.16	9.42	9.07	%
WL(Total)	0.0062	0.0072	0.0073	gr
WL(O)	1.026	1.026	1.026	gr/m^2
WL(O) Using AA8 gr/m^2	0.0056	0.0055	0.0057	gr
WL(P)	0.0006	0.0017	0.0016	gr
WL(P)	9.16	23.97	21.90	%
Calculated surface area	553.22	1411.55	1337.88	mm^2
Calculated surface area	0.0005532	0.0014116	0.0013379	m^2
Increased area due to punching	0	857.14	783.47	mm^2
Increased area due to punching	0	0.0008571	0.0007835	m^2
Increased area due to punching	1	2.55	2.41	Multiplier
A(Total with correction)	**6041.09**	**6745.19**	**6893.24**	**mm^2**
New corrosion rates:				
Corrosion rate (linear area)	0.0359	0.0374	0.0371	mm/yr
Corrosion rate (last measurement)	0.0289	0.0271	0.0268	mm/yr
Old corrosion rates:				
Corrosion rate (linear area)	0.0359	0.0428	0.0418	mm/yr
Corrosion rate (last measurement)	0.0289	0.0311	0.0302	mm/yr

Potential improvements to the punching parameters

Figure 54 shows how the 0.16mm cutting clearance had superior fatigue life to 0.42mm, representing the B-series and the C-series, respectively. Smaller cutting clearance seemed to help, but the B-series showed a far from perfect surface. To improve the punched surface, an even tighter cutting clearance (>0.16mm) should be attempted. Since so far, the lowest cutting clearance appeared to be superior. If this does not yield a theoretical punched surface, with a single burnish and fracture zone, it should be experimented with a wider cutting clearance as well. A better fatigue life should be expected when the “wounds” are gone. The counter

trimmed surfaces also have a great potential for improvement. Beginning with a good initial punch would probably be the best way to improve the D-series. Since every sample had its fracture originating from a wound or the zone around it, improving the punching parameters should yield a significant increase in fatigue life for both series.

5.2 Fatigue life (S-N curves)

Difference between air and saltwater

A-, B-, and the D-series all had reduced fatigue life while testing in the saltwater (5wt% NaCl). This was expected, as corrosion is well known to reduce fatigue life. Corrosion reduces surface roughness, as seen in Table 13. Corrosion also creates a weak point for a fracture to initiate. Therefore, it was thought that the difference between the series would be reduced when exposed to a corrosive medium. It would be reduced because of two reasons: First reason being that the B- and D-series would get a greater reduction in surface roughness than the A-series due to much higher surface roughness values. The B-series with the highest surface roughness should be the most affected. Second reason being that the punched surfaces and the counter trimmed surfaces would already be such a suitable place for fracture initiation. The saltwater would not have time to have a severe effect on the fatigue life. The A-series with its rather unflawed surface however, would greatly be affected by the corrosive medium and a potential weak spot.

This is what we see in the experimental results as well. The B- and D-series do clearly have a reduced fatigue life in the corrosive medium, but the A-series does appear to be more affected. In both distilled water and air, the A-series reached runout at one million cycles at σ_a = 99MPa. In saltwater, though having one sample which reached runout at σ_a = 72MPa, it still had two samples failing within the range (only three samples were tested due to time restrictions). At σ_a = 99MPa it had an Nf around 150k cycles. This reduction in fatigue life is quite severe. By assuming the air samples in the A-series would have failed at 1000k cycles (which it most likely wouldn't have) this is a reduction of 850k cycles due to the corrosion medium. That is a decrease equal to a factor of 6.7 (Nf(air) / Nf(saltwater). The B- and D-series at the same stress amplitude only have a reduction equal to around 20k and 80k cycles, respectively. That is a factor 1.5 and 2.6, respectively. Looking at the individual graphs for the different series (Figure 56, Figure 57, Figure 58), the gap between air and saltwater tested samples are far greater in the A-series than the D-series. And the B-series having even less of a difference.

Difference between air and distilled water

The A-series reached runout in both air and distilled water and is therefore irrelevant for this section. Distilled water does have an effect on fatigue life, because it increases the amount of hydrogen present. Distilled water decreases fatigue life was also seen in a master thesis conducted by Nanninga [8].

The B-series displayed no difference (Figure 57) between distilled water and air. Looking at Figure 67, which shows a sample from the B-series tested in air, it also had fracture initiation at a wound just like the samples tested in saltwater. Taking the topography, microstructure, and surface roughness of the B-series in account as well, the severity of these wounds created

during punching are quite clear. This could explain the absence of a difference between air and distilled water. As discussed earlier, there is but only a small difference between saltwater and air (and distilled water) in this series. This is probably because of very rapid fracture initiation originating from the wounds. This leads to rather small exposure time to the aqueous solutions. And the increase in hydrogen concentration because of the distilled water, does not have time to affect the fatigue life. The chlorides in the saltwater does manage to affect the fatigue life, but only to a small degree. This is because of the high concentration (5wt% NaCl) which is a harsh chemical environment.

The D-series displays a significant difference in fatigue life in air and distilled water. They show a difference equal to 30k and 320k cycles at σ_a = 99MPa and σ_a = 72MPa, respectively. This equals a factor of 1.3 and 2.0, respectively. Air being the superior one. Just like the B-series, this series showed fracture initiation at the same location for air and saltwater. Figure 52 and Figure 53 clearly show a greater difference between the B-series and the D-series in air, than in distilled water. The topography, microstructure, and surface roughness of the D-series, show a smoother surface than the B-series (though still flawed). However, with its general longer fatigue life than the B-series in air and distilled water, it is probable that the increased concentration of hydrogen will affect the D-series and results in more rapid fracture initiation. This effect is also enhanced when the number testing cycles increases (σ_a decreases).

Effect of stress ratio (R) and fatigue life estimations using SWT

Going from R = -1 to R = 0.1 with the same σ_{max}, does however greatly change the σ_a. The common σ_{max} used in the results from the specialization project and this thesis is 220MPa and 160MPa. Any higher max stress would be too close to the yield strength. While at R = -1 this is equal to σ_a = 220MPa and 160MPa. It only equals σ_a = 99MPa and σ_a = 72MPa, respectively, at R = 0.1. This is a huge difference in the sheer amount of energy being forced upon the material. Even though at R = -1, half of the stress will be in compression instead of tension, it will still affect the material. Comparing Figure 51 and Figure 54, there is a severe reduction in fatigue life for every series tested at R = -1, which should be expected with this difference in stress amplitude.

The relationship between which series have the superior fatigue life remains the same: A > D > B (> C). This suggests R = -1 could be used instead of R = 0.1 without corrupting the results. However, the difference between the series are greatly reduced at R = -1. This should be expected as fracture initiation would be much faster (higher stress amplitude). The machined series and counter trimmed surface would have such an increased fracture initiation speed that it would “catch up” some of the difference to the punched series. The fractography conducted for the R = -1 showed the same fracture initiation sites as it did at R = 0.1 (wounds and corners). The fracture looked different though. This is due to the tension part of the cycles at R = -1. The tension smashes the fracture together for every cycle, while at R = 0.1 the fracture will only keep opening for every cycle.

Relating the tests done at R = -1 to R = 0.1 was done through SWT. In Figure 74 you can see how the SWT estimates relate to the actual results. The D-series estimate appears to be rather spot on, while the A-series had its fatigue life underestimated and the B-series had it

overestimated. The A-series was underestimated with a factor of 2.9 at σ_a = 99MPa. The B-series was overestimated with a factor of 2.4 and 3.0 for σ_a = 99MPa and 72MPa, respectively. That is not a horrible estimate. In order to a proper estimate for such complex surfaces, many factors need to be accounted for.

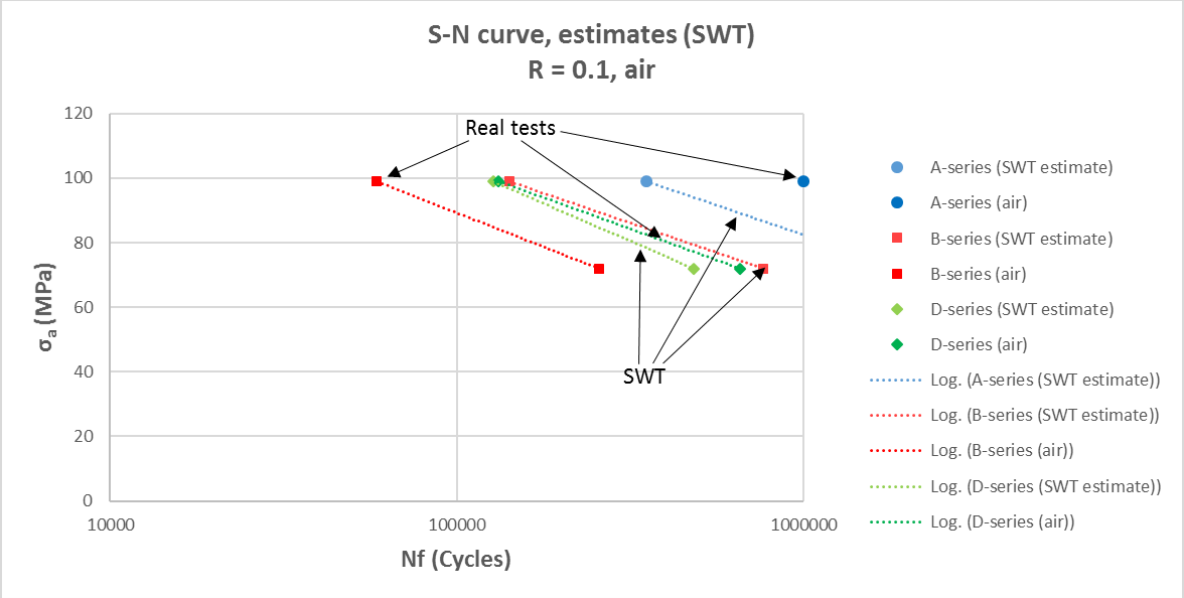

Figure 74: Comparing the SWT estimated fatigue life at R = 0.1 based on previous results with actual tests at R = 0.1. The intense colors represent the real tests, and the faded colors represent the corresponding estimates.

Effect of temperature and humidity

Table 14 shows that the temperature in the aqueous solution in the chamber was the same as the environment. The temperature in the environment was quite stable around 24°C, as seen in Figure 92. This should not have had any significant effect. Humidity in the corrosion fatigue testing is irrelevant, since the samples were emerged in saltwater.

For the samples tested in air, the humidity varied as shown in Table 22. RH varied from 20-36%. None of which are significantly high. The same stress levels for the different series had the same RH range. Meaning the difference between the series was not affected. This difference in RH would have had a neglectable effect.

5.3 Fractography

The fractography used to find fracture initiation for the different series are quite clear. The A-series has fracture initiation in the corners, the B-series and D-series had fracture initiation at the wounds or the immediate surrounding area around a wound. Enough samples were checked to say that this is the general case.

Figure 70 (D-series) shows how the grain boundaries are clearly visible in the micrograph. At the beginning of studying these fracture surfaces, these lines were thought to be fracture propagation lines. But they made no sense in how the crack then would have propagated. After investigating further, the actual propagation lines, sometimes going in completely different directions, appeared. The comparison between the microstructure (4.2 Microstructure) was made, and it was clear that this is the actual grain structure. This was

seen in every series tested in corrosion fatigue.

To see the actual crack propagation lines, you must look within the grains. Though it did vary to what degree this was visible. This is probably because the samples were not always taken out directly after testing. The time spent idle in the saltwater post fracture initiation varied. Which means that the amount of corrosion varied.

Figure 72 is of a D-series sample tested in air. Here you cannot see the grain structure. It might be possible to see indications of it, if you know what to look for. But nonetheless, it is much more evident in the corrosion fatigue tested samples. The grain structure must therefore be enhanced by corrosion.

Intergranular corrosion (IGC) appear to have taken place. It is thought that it is the IGC which makes the grain boundaries so visible. It is probable that it is IGC, because it attacks the grain boundaries in specific. If these grain boundaries are much more corroded than the surroundings, it would be natural for the boundaries to become more visible. It was thought that maybe there were some stress corrosion cracking occurring as well, but this is not known to happen in this alloy. Therefore, it was debunked. Figure 71 shows a sample which was removed immediately after testing. This micrograph also shows the grain boundaries. This means that the corrosion effect which makes the grain boundaries visible happens immediately. Though they do appear more vividly in the samples which stayed longer in the saltwater, like in Figure 68. More micrographs and fractography can be found in Appendix C: SEM micrographs.

Pitting corrosion happens at open surfaces as explained in the 2.7.2 Pitting corrosion (Pitting). In SEM, they should appear round and at an open surface. That would be in the middle of grain. It is possible that this is what we see in some of fracture surfaces (the black circles in Figure 64). However, this was not to the same extent as the corrosion of the grain boundaries. It might also have happened at the surfaces of the punched series.

5.4 Error sources

Corrosion fatigue testing

The machine seen in Figure 30 could have affected the corrosion of the saltwater. The top part, made from steel, could have had a galvanic effect on the corrosion happening during testing. To which extent this happened is uncertain. Separate tests to specifically study this effect must have been executed to identify the severity of it. The effect should be the same for all samples.

The punched series have a surface roughness which makes it hard to accurately measure the cross-section test area. It was also measured by hand. Both could have created an inaccurate measurement. Meaning the samples would have been tested with slightly wrong stress amplitudes.

Topography and surface roughness

As shown in Figure 23, the actual depth of the wounds was not always accurately measured. This affects both the surface roughness values and the understanding of the crack propagation paths. Several samples had fractures at the end of the test area. Right where the samples start to bend. This area was not considered when measuring the surface roughness. It might be elevated at that point due to imperfect punching. It could also be a stress concentration here because of the sample geometry.

The vertical resolution was more than sufficient for the B- and D-series. The A-series however, were on the verge of what the 10x lens could handle. Higher magnification on the lenses could not be used due to the geometry of the samples. This means the A-series might have slightly wrong values. However, it still showed a greatly improved surface to the other series.

Fractography

The microstructure seen in the SEM was thought to have become visible because of IGC. This is simply due to the nature of IGC. However, it is possible that it is due to another corrosion phenomenon, or simply appears because of an aqueous solution present.

Stress corrosion cracking was debunked because it is not known to happen in this alloy. Corrosion fatigue and stress corrosion are two very similar fracture mechanisms. They are hard to separate. It is therefore a possibility that there was some stress corrosion cracking.

6. Conclusion

Corrosion fatigue of extruded AA6082 has been investigated. Three different surfaces were compared; Machined, punched, and counter trimmed surfaces. Testing was done at R = 0.1, the corrosive medium was 5wt% NaCl, and runout was defined as one million cycles (10^6). The topography of each series was thoroughly studied with the use of an optical scanner based on focus-variation. Fractography was done in SEM.

- Fatigue life in both air and corrosive environment, ranked: A-series (Machined) > D-series (Counter trimmed) > B-series (Punched).

- Corrosion affects the fatigue life of smooth surfaces more than it does rough surfaces.

- Fractography revealed that the machined series have fracture initiation at the edges. The punched and counter trimmed surface had fracture initiation at the wounds created during shaping. The sample side with the highest Rv value (deepest valley) proved most likely to have fracture initiation in the B- and D-series. Fractography also revealed that this alloy is susceptible to IGC (or some other form of grain boundary corrosion) during corrosion fatigue testing.

- The corrosion rates of the samples showed that punched surface area must have been increased with a factor of 2.55 and 2.41 in the B- and D-series, respectively, compared to a machined surface.

- Topography analysis revealed that the that the surface roughness values varied as follows: A-series >> D-series > B-series. A direct link between surface roughness values and fatigue life within a series could not be found. It also revealed that the punching parameters were not ideal. The punched and counter trimmed surfaces greatly varied from each other.

- Further work:
    - Experimenting with punching parameters for both regular punching and counter trimming. And testing these in fatigue and corrosion fatigue.

    - Closer study of the corrosion effects. Study IGC depth etc.

    - Testing T6 and T7 in fatigue and corrosion fatigue. Checking if temper states change the corrosion effect on fatigue life.

    - Identify fatigue-coefficients to estimate fatigue life more accurately.

7. References

1. Schütz, W., *A history of fatigue.* Engineering Fracture Mechanics, 1996. **54**(2): p. 263-300.
2. Dowling, N.E., *Mechanical behavior of materials : engineering methods for deformation, fracture, and fatigue*. Prentice-Hall international editions. 1993, Englewood Cliffs, N.J: Prentice Hall.
3. Scott, P.M., *8.6 - Corrosion Fatigue**, in *Corrosion (Third Edition)*. 1994, Butterworth-Heinemann: Oxford. p. 8:143-8:183.
4. Rowe, J., *Advanced Materials in Automotive Engineering*. Woodhead Publishing in Materials. 2012, Cambridge, UK: Woodhead Publishing.
5. Zhang, K., Q. Wang, and Z. Ding, *Influence of relative clearance to hole quality in punching process.* Advanced Materials Research, 2014. **1004-1005**: p. 1365-1368.
6. The Library of Manufacturing. *Sheet metal cutting*. [cited 2016 19th of November]; Available from: http://www.thelibraryofmanufacturing.com/sheetmetal_cutting.html.
7. Suresh, S., *Fatigue of Materials*. 2nd ed. ed. Fatigue of Materials, Second Edition. 1998, Cambridge: Cambridge University Press.
8. Nanninga, N.E., *High cycle fatigue of AA6082 and AA6063 aluminum extrusions [Master thesis]*. 2008, Michigan Technological Universty.
9. Callister, W.D. and D.G. Rethwisch, *Materials science and engineering*. 8th ed., SI version. ed. 2011, Hoboken, N.J: Wiley.
10. The University of Liverpool. *AluSelect Wrought Alloy Compositons*. 2011 [cited 2016 September 5th]; Available from: http://dev.aluminium.matter.org.uk/aluselect/06_wrought_comp.asp.
11. Solberg, J.K., *Teknologiske metaller og legeringer*. 2002, Trondheim: Institutt for materialteknologi, Norges teknisk-naturvitenskapelige universitet.
12. Cuniberti, A., et al., *Influence of natural aging on the precipitation hardening of an AlMgSi alloy.* Materials Science and Engineering: A, 2010. **527**(20): p. 5307-5311.
13. Herring, D., *Temper Designations for Aluminum Alloys: What They Are and Why We Need to Know.* Industrial Heating, 2012. **80**(2): p. 20.
14. Brynjulfsen, M., H.J. Roven, and T. Furu, *Fatigue of Extruded AA6082 and AA7108 Alloys - The Effects of Natural Ageing Compared to Artificial Ageing [Master thesis]*. 2015, NTNU.
15. Almar-Næss, A., *Metalliske materialer : struktur og egenskaper*. 3. utg., 5. [rev.] oppl. ed. 1993, Trondheim: Tapir.
16. Campbell, F.C., *Elements of metallurgy and engineering alloys*. 2008, Materials Park, Ohio: Materials Park, Ohio : ASM International.
17. Dieter, G.E. and D. Bacon, *Mechanical metallurgy*. SI metric ed. ed. McGraw-Hill series in materials science and engineering. 1988, London: McGraw-Hill.
18. Hjelen, J. and Sintef, *Scanning elektron-mikroskopi compendium*. 1989, Trondheim: SINTEF.
19. Anderson, T.L., *Fracture mechanics : fundamentals and applications*. 3rd ed. ed. 2005, Boca Raton, Fla: Taylor & Francis.
20. Davis, J.R., *Corrosion of aluminum and aluminum alloys*. 1999, Materials Park, OH: Materials Park, OH : ASM International.
21. Elayaperumal, K. and V.S. Raja, *Corrosion Failures : Theory, Case Studies, and Solutions*. Wiley Series in Corrosion. 2015, Hoboken: Wiley.
22. Burt, V., *Corrosion in the Petrochemical Industry (2nd Edition)*. ASM International.
23. Rajakumar, S., C. Muralidharan, and V. Balasubramanian, *Predicting tensile strength, hardness and corrosion rate of friction stir welded AA6061-T6 aluminium alloy joints.* Materials & Design, 2011. **32**(5): p. 2878-2890.
24. Feidenhans'l, N.A., et al., *Comparison of optical methods for surface roughness characterization.* Measurement Science and Technology, 2015. **26**(8): p. 085208.

Appendix A: Topography

The B- and D-series have very different surfaces. Some extra surfaces are shown here to help show the diversity. Only the height filtered photos are shown.

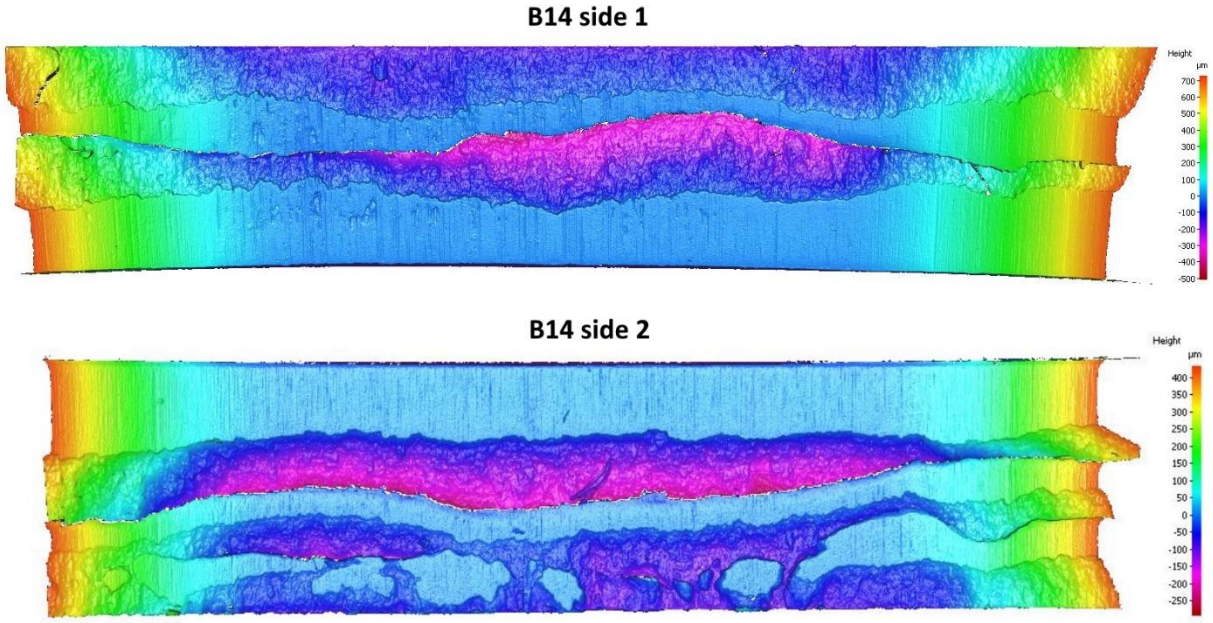

Figure 75: Topography picture of B14.

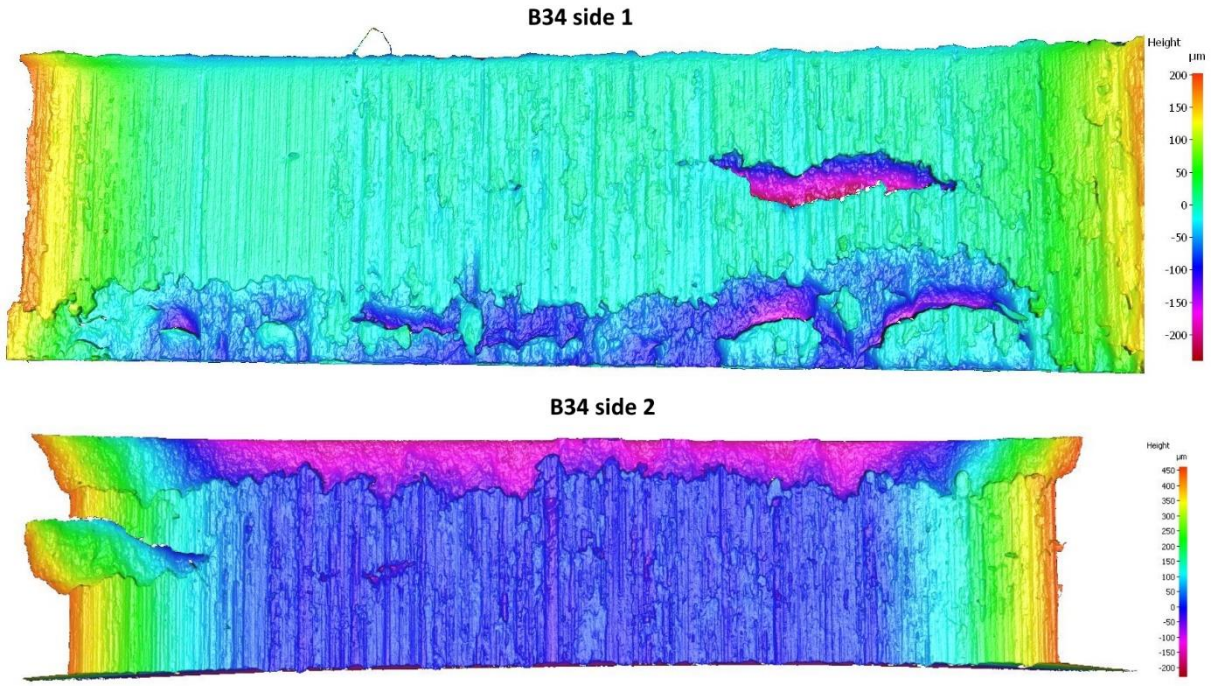

Figure 76: Topography picture of B34.

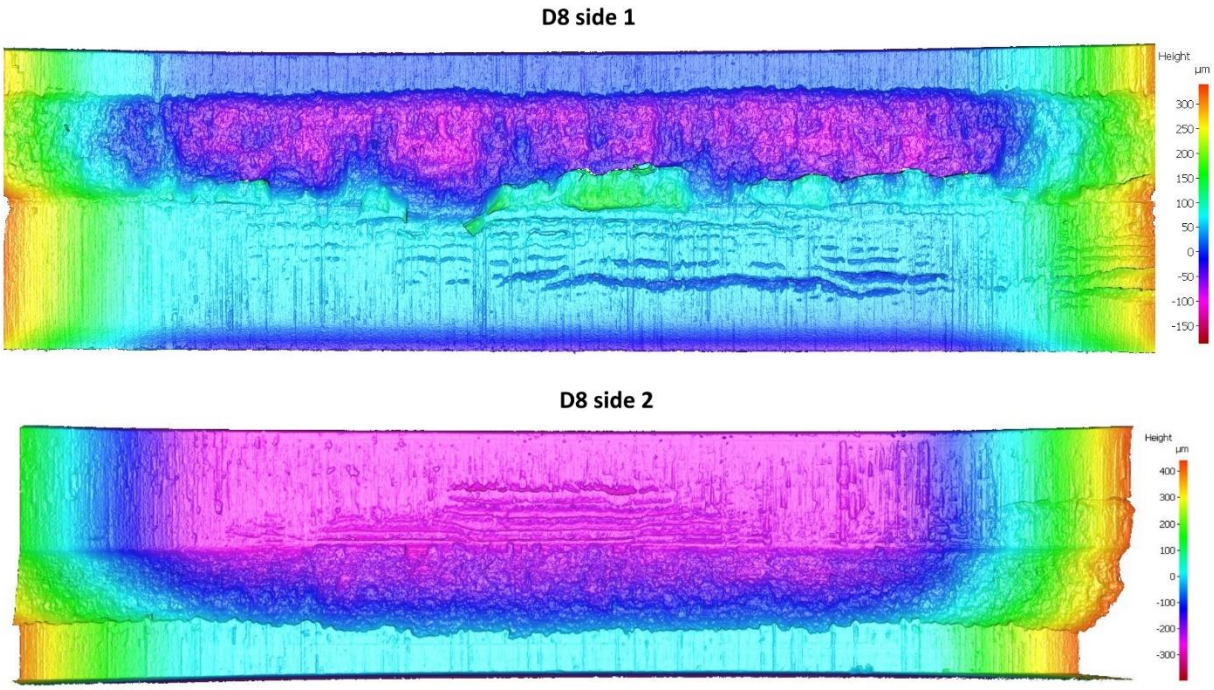

Figure 77: Topography picture of D8.

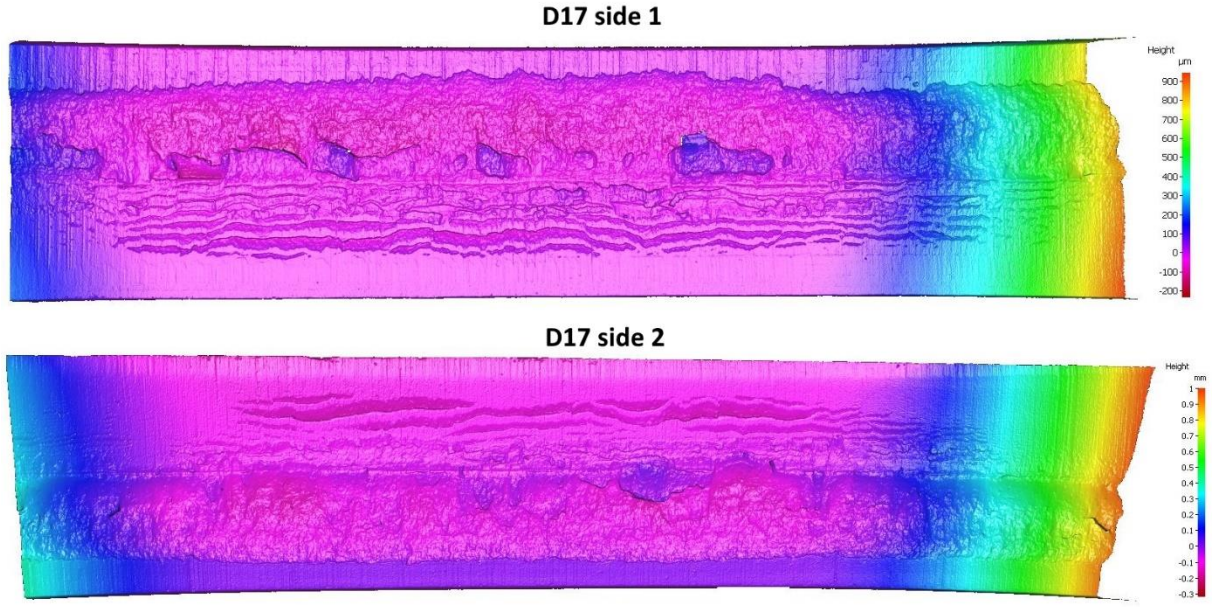

Figure 78: Topography picture of D17.

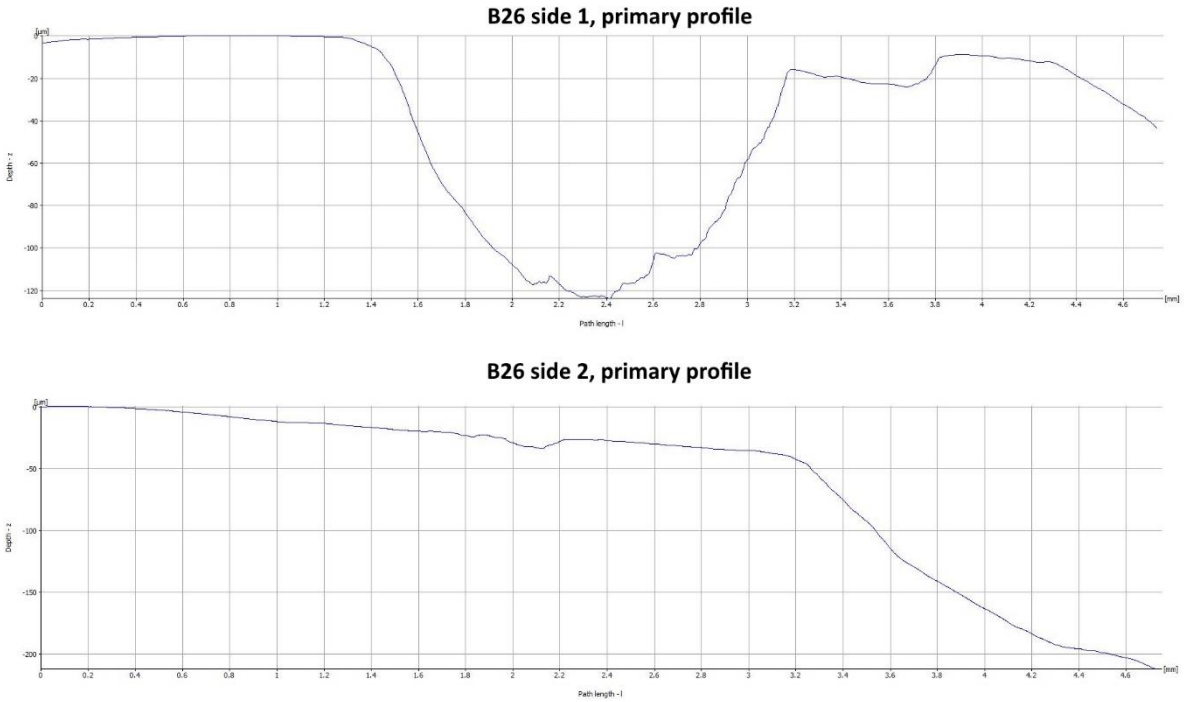

Figure 79: Primary profiles of B26.

The surface roughness data found in this thesis have been compared with fatigue life to look for any links between the two. Below are the graphs showing Ra/Rt/Rz vs Nf for both the B- and D-series. The average surface roughness value for the sides which had fracture initiation are the values compared to its fatigue life.

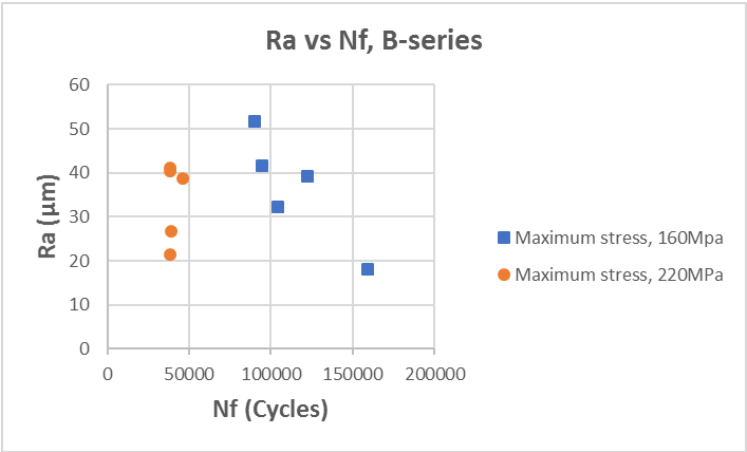

Figure 80: Ra vs Nf for the B-series.

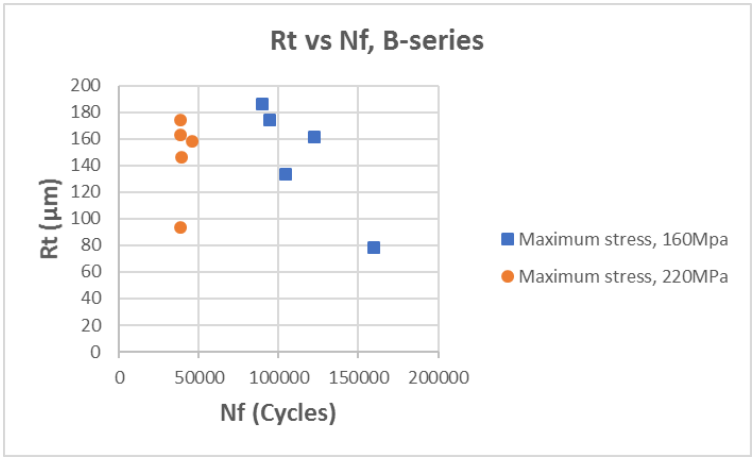

Figure 81: Rt vs Nf for the B-series.

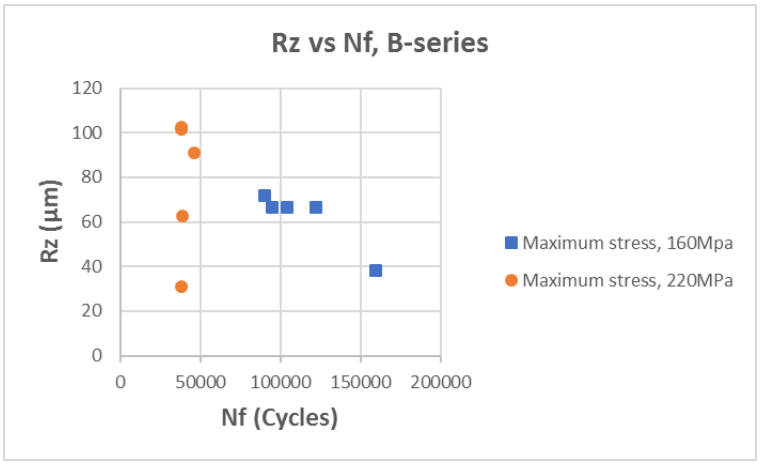

Figure 82: Rz vs Nf for the B-series.

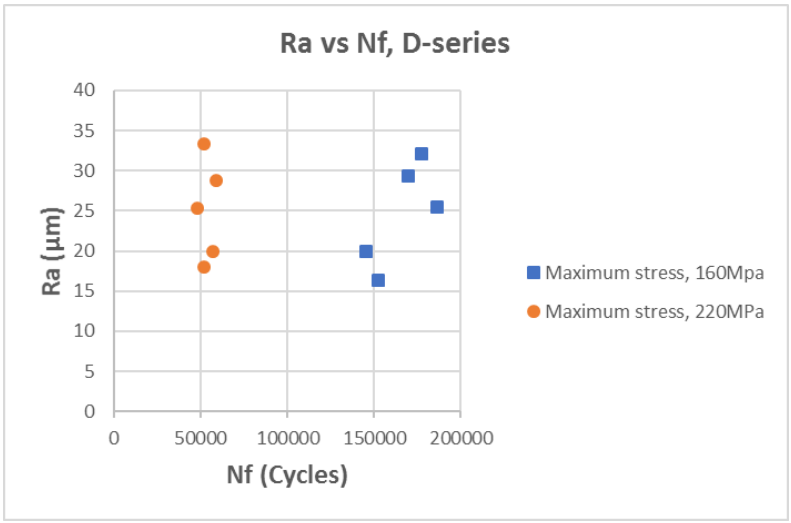

Figure 83: Ra vs Nf for the D-series.

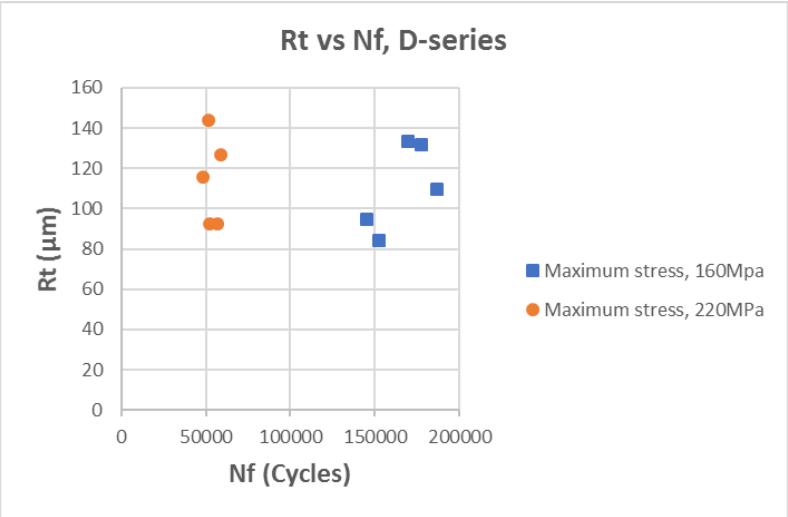

Figure 84: Rt vs Nf for the D-series.

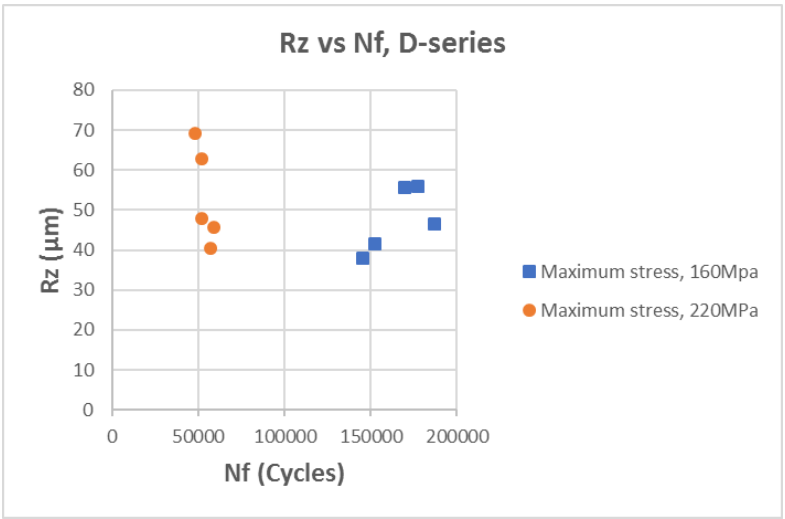

Figure 85: Rz vs Nf for the D-series.

Appendix B: Fatigue data

This appendix will give the raw data from the fatigue testing. It will also include standard deviation calculations of the fatigue data. They also show a lot of samples which weren't discussed or shown in the results. This is because these tests were invalid. This could be because of where fracture occurred, or that they were an experiment with different frequency.

Table 16: Raw fatigue data for the A-series. Please note that standard deviation is only calculated for the valid tests.

Sample	Frecuency (Hz)	Scanned	σa (MPa)	Type	Nf (cycles)	testing time (h)	Stdev	Notes
A24	5	yes	99	Dis.water	1000000	55.6		
A34	4	yes	99	Salt Water	346519	24.1		Fracture outside test area
A20	4	yes	99	Salt Water	295282	20.5		Fracture outside test area
A15	5	yes	99	Salt Water	189977	10.6		Fracture outside test area
A13	5	yes	99	Salt Water	356845	19.8		Fracture outside test area
A22	3	yes	99	Salt Water	177642	16.4		Fracture outside test area
A30	5	no	99	Salt Water	114623	6.4		Fracture outside test area
A16	5	no	99	Air	613665	34.1		Severe notch before testing
unmarked	5	no	99	Air	1000000	55.6		
A28	5	no	72	Salt Water	162863	9.0		Fracture outside test area
A7	5	no	72	Salt Water	366937	20.4	325156	
AA3	5	no	72	Salt Water	554616	30.8	325156	
AA2	5	no	72	Salt Water	959373	53.3		Fracture outside test area
AA1	5	no	72	Salt Water	1000000	55.6	325156	
AA10	5	no	99	Salt Water	161612	9.0	23984	
AA9	5	no	99	Salt Water	118233	6.6	23984	
AA7	5	no	99	Salt Water	173651	9.6	23984	
AA6	5	no	99	Salt Water	196233	10.9		Fracture outside test area
AA5	5	no	99	Salt Water	122893	6.8	23984	
A9	5	no	99	Salt Water	145754	8.1	23984	

Table 17: Raw fatigue data for the B-series.

Sample	Frecuency (Hz)	Scanned	σa (MPa)	Type	Nf (cycles)	testing time (h)	Stdev
B6	5	yes	72	Salt water	104449	5.8	28166
B14	5	yes	72	Salt water	94639	5.3	28166
B21	5	yes	72	Salt water	122401	6.8	28166
B25	5	yes	72	Salt water	159411	8.9	28166
B31	5	yes	72	Salt water	90029	5.0	28166
B32	5	yes	99	Salt water	38508	2.1	3342
B18	5	yes	99	Salt water	38264	2.1	3342
B26	5	yes	99	Salt water	38226	2.1	3342
B19	5	yes	99	Salt water	38794	2.2	3342
B23	5	yes	99	Salt water	45903	2.6	3342
B27	0.3	yes	99	Salt water	35449	32.8	
B15	3	yes	99	Salt water	37352	3.5	
B20	5	no	99	air	58742	3.3	
B29	5	no	72	air	256225	14.2	
B35	5	no	99	distilled water	59792	3.3	
B46	5	no	72	distilled water	242408	13.5	

Table 18: Raw fatigue data for the D-series.

Sample	Frecuency (Hz)	Scanned	σa (MPa)	Type	Nf (cycles)	testing time (h)	Stdev
D17	5	yes	72	Saltwater	152601	8.5	17148
D24	5	yes	72	Saltwater	186642	10.4	17148
D26	5	yes	72	Saltwater	169710	9.4	17148
D34	5	yes	72	Saltwater	177364	9.9	17148
D5	5	yes	72	Saltwater	145308	8.1	17148
D39	5	yes	99	Saltwater	48170	2.7	4342
D30	5	yes	99	Saltwater	58990	3.3	4342
D32	5	yes	99	Saltwater	57014	3.2	4342
D2	5	yes	99	Saltwater	51795	2.9	4342
D7	5	yes	99	Saltwater	52200	2.9	4342
D11	5	yes	99	air	131684	7.3	
D4	5	no	72	air	656084	36.4	
D29	5	no	72	distilled water	330254	18.3	
D16	5	no	99	distilled water	101814	5.7	
D9	0.3	no	99	saltwater	76859	71.2	

Appendix C: SEM micrographs

Several micrographs are shown in 3.6 Fractography (SEM). Micrographs of one sample from each series will be added here. These micrographs are taken of samples tested in corrosion fatigue (5wt% NaCl), with R = 0.1 and room temperature (ca 24°C). The stress amplitude varies and is given in the figure caption. Micrographs were chosen based on which stress amplitudes were not represented in the results.

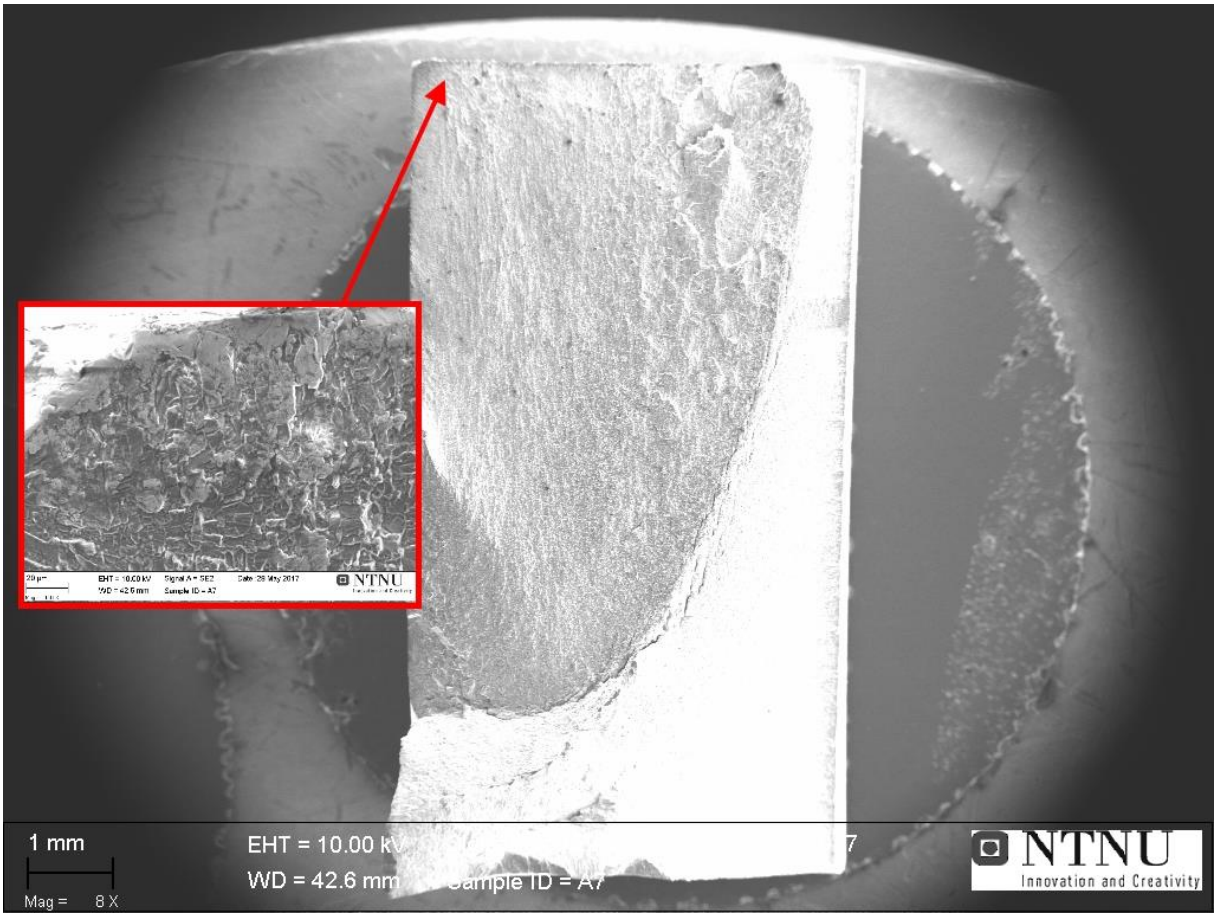

Figure 86: Overview micrograph of A7 (σ_a = 72MPa.). Fracture initiation is enhanced at 600x.

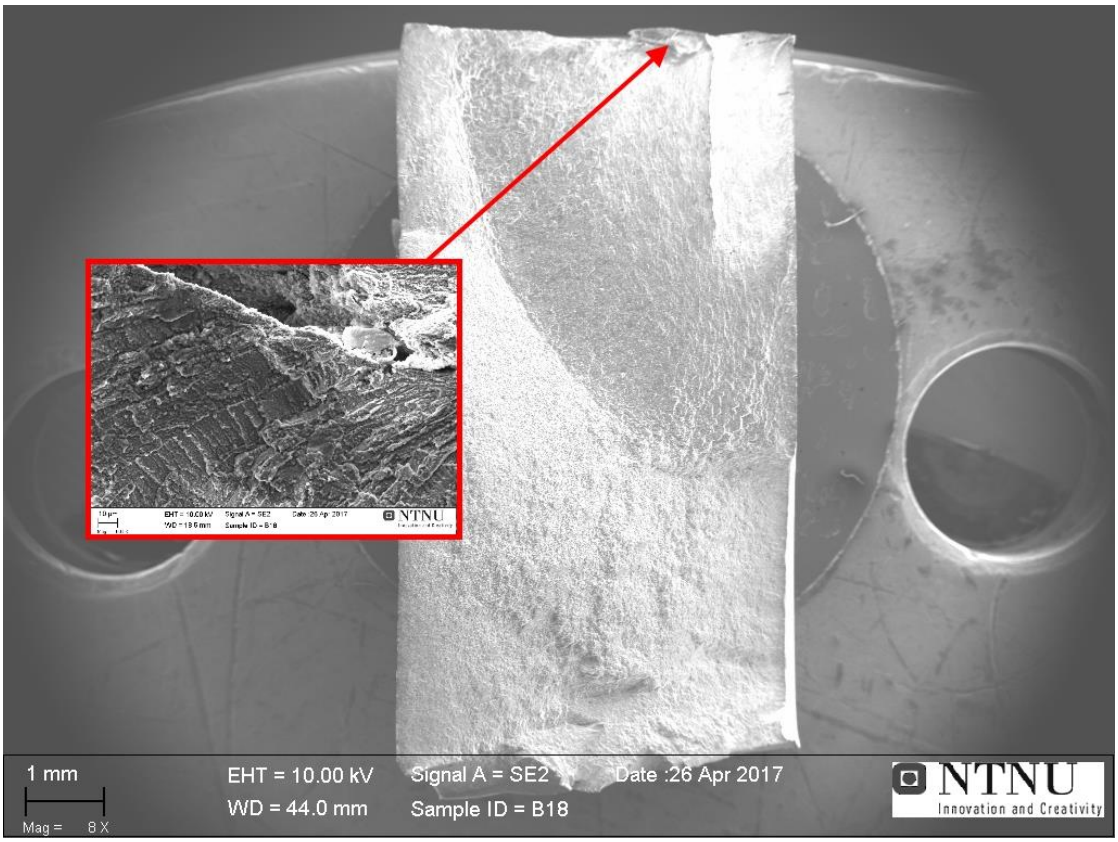

Figure 87Overview micrograph of B18 (σa = 99MPa.). Fracture initiation is enhanced at 600x.

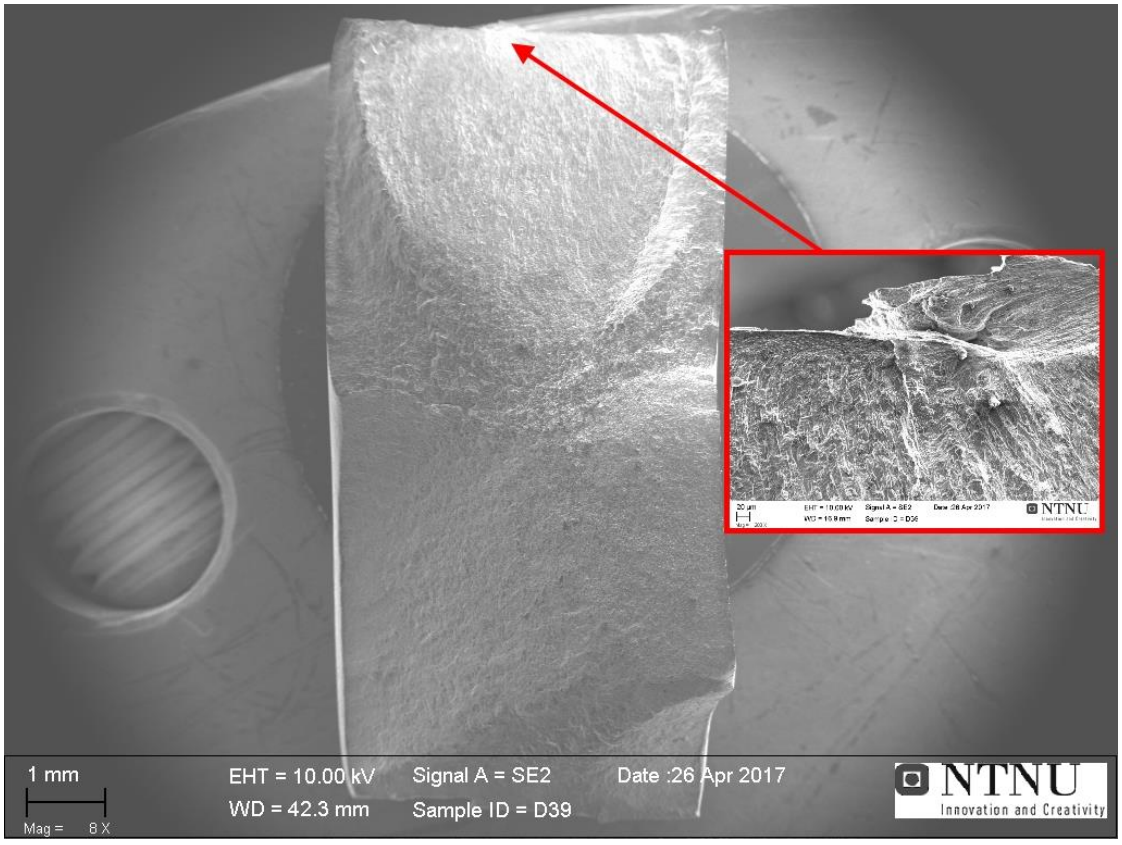

Figure 88: Overview micrograph of D39 (σa = 99MPa.). Fracture initiation is enhanced at 200x.

Appendix D: Corrosion rate calculations

To understand the section abbreviations please use Figure 89. SL and SR means side left and side right, respectively. These are the two end sides which are not shown in the figure. Some of the samples had holes in the sample's heads, these were taken in account as shown in. The surface MT1, MT2 and MT was for the initial corrosion rate calculations considered to be completely flat. This was discussed and corrected for (see 5.1 Topography and surface roughness). The clearly damaged surface in the B- and D-series was not accounted for while calculating the surface area shown below.

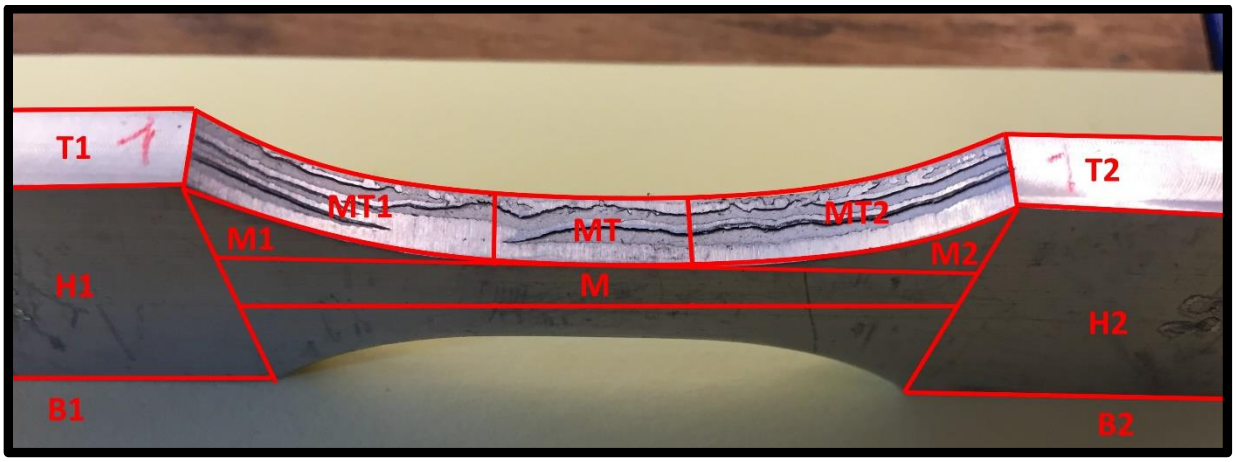

Figure 89: Showing how the samples were divided into sections to calculate the surface area.

Table 19: Showing the areas for AA8 used in the corrosion rate calculations.

AA8			
Section	**mm^2**	**Multiplies**	**sum (mm^2)**
M	240.24	4	960.96
MT1 / MT2	106.50	8	852.03
M1 / M2	42.67	4	170.67
MT	63.60	2	127.20
SL	132.61	1	132.61
T1	157.68	1	157.68
B1	157.68	1	157.68
H1	744.35	2	1488.69
SR	132.55	1	132.55
T2	162.71	1	162.71
B2	162.71	1	162.71
H2	767.81	2	1535.61
Hole area missing	0	4	0
New area in hole	0	2	0
Total area:	6041.09	mm^2	
Total area:	60.41	cm^2	
Total area:	0.6041	dm^2	
Total area:	0.006041	m^2	

Table 20: Showing the areas for B34 used in the corrosion rate calculations.

B34			
Section	**mm^2**	**Multiplies**	**sum (mm^2)**
M	239.52	4	958.08
MT1 / MT2	106.50	8	852.03
M1 / M2	42.67	4	170.67
MT	64.20	2	128.40
SL	125.19	1	125.19
T1	166.33	1	166.33
B1	160.93	1	160.93
H1	715.69	2	1431.38
SR	124.87	1	124.87
T2	169.76	1	169.76
B2	160.34	1	160.34
H2	720.04	2	1440.08
Hole area missing	-30.19	4	-120.76
New area in hole	104.21	2	208.41
Total area	5888.05	mm^2	
Total area	58.88	cm^2	
Total area	0.5888	dm^2	
Total area	0.00589	m^2	

Table 21: Showing the areas for D8 used in the corrosion calculations

D8			
Section	**mm^2**	**Multiplies**	**sum (mm^2)**
M	239.76	4	959.04
MT1 / MT2	106.50	8	852.03
M1 / M2	42.67	4	170.67
MT	64.20	2	128.40
SL	134.02	1	134.02
T1	165.10	1	165.10
B1	167.46	1	167.46
H1	778.55	2	1557.11
SR	134.02	1	134.02
T2	160.66	1	160.66
B2	163.50	1	163.50
H2	758.89	2	1517.78
Hole area missing	-30.19	4	-120.76
New area in hole	104.21	2	208.41
Total area:	6109.7759	mm^2	
Total area:	61.097759	cm^2	
Total area:	0.6109776	dm^2	
Total area:	0.0061098	m^2	

Appendix E: Artificial ageing curve at 180°C

Figure 90 and Figure 91 show the artificial ageing curves based on hardness and yield strength respectively. Please note that at maximum yield strength only one sample measured the given value. As stated in the results, there were complications and further investigation or retesting should have been executed. However, there was no time. Therefore, these results are shown in the appendix. Both hardness and yield strength showed a peak around three hours (180min).

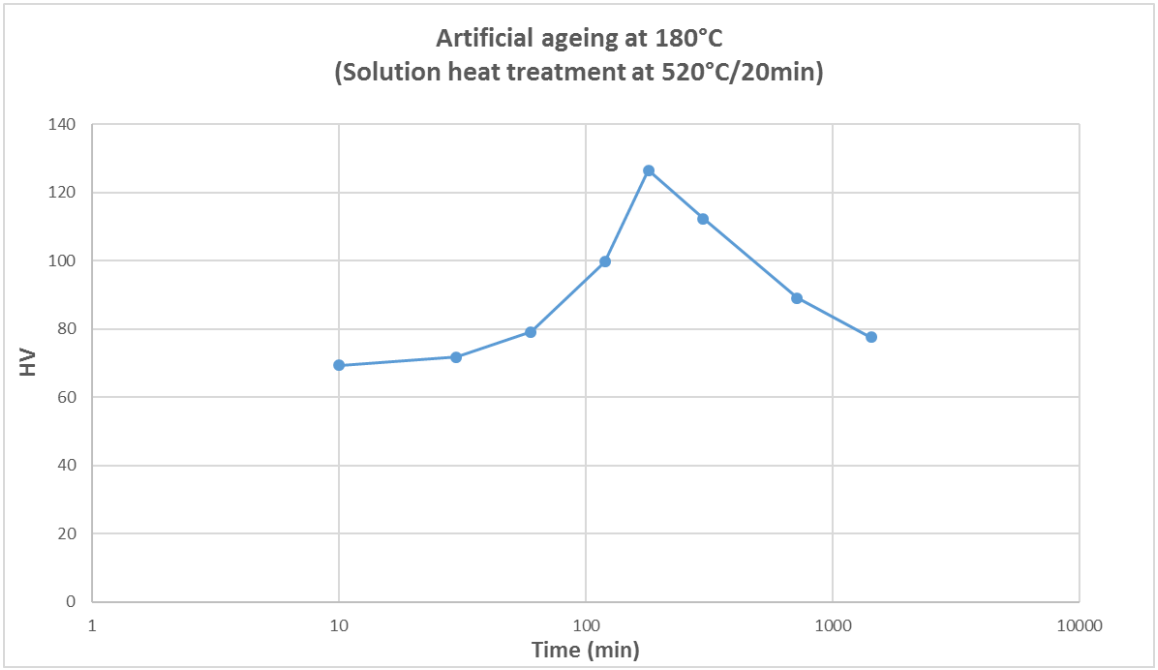

Figure 90: Artificial ageing curve. HV (Vickers) as function of being artificially aged at 180°C.

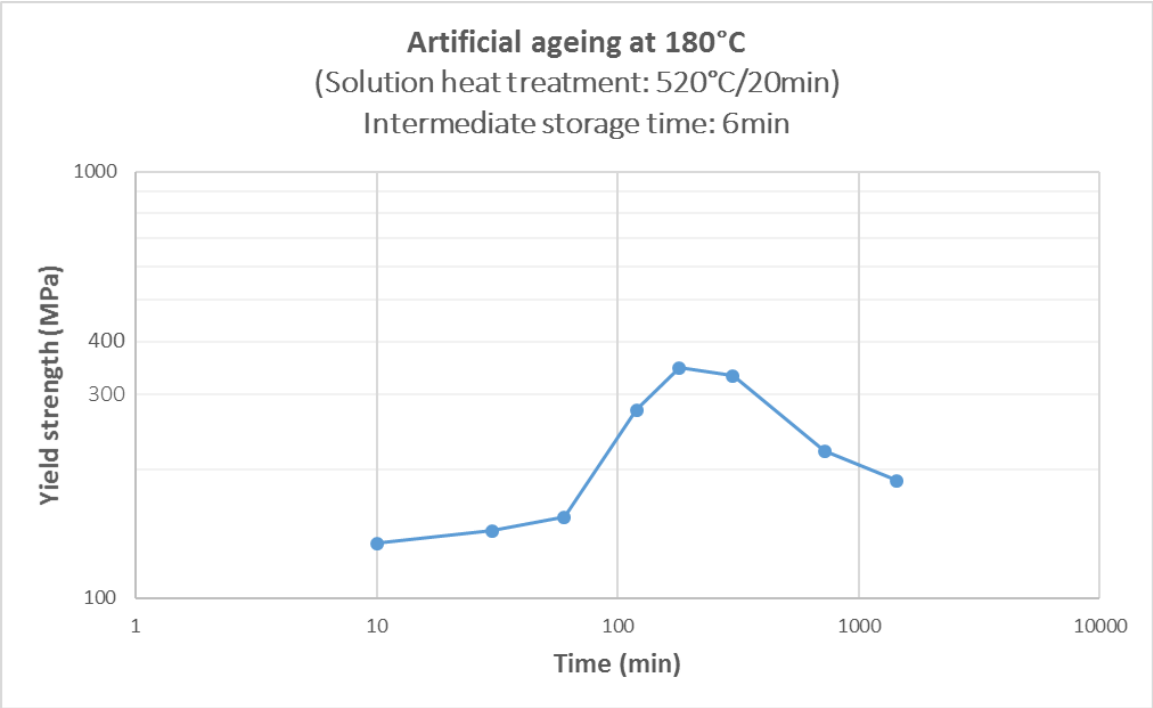

Figure 91: Artificial ageing curve. Yield strength as a function of being artificially aged at 180°C. Peak yield strength was 346.5MPa found at 3hours.

Appendix F: Temperature and humidity

Figure 92 shows the relative humidity and temperature of the laboratory where the corrosion fatigue testing was executed. Temperature appears to be quite stable around 24°C. Relative humidity had a great increase towards the end. The low and high alarms are of no relevance. Humidity measurements are only relevant for the days when samples were tested in air. Table 22 shows the relative humidity for the samples tested in air. Please note that these samples were tested when it was the most efficient to perform a time-consuming test.

Table 22: Relative humidity for the samples tested in air. The RH is given in a range because these tests usually took more than one day.

Series	Date	σ_a	σ_{max}	RH (%)
A-series	05.02.2017	99	220	20-24
B-series	05.23.2017	72	160	32-36
B-series	05.01.2017	99	220	20-24
D-series	05.24.2017	72	160	32-36
D-series	04.26.2017	99	220	20-24

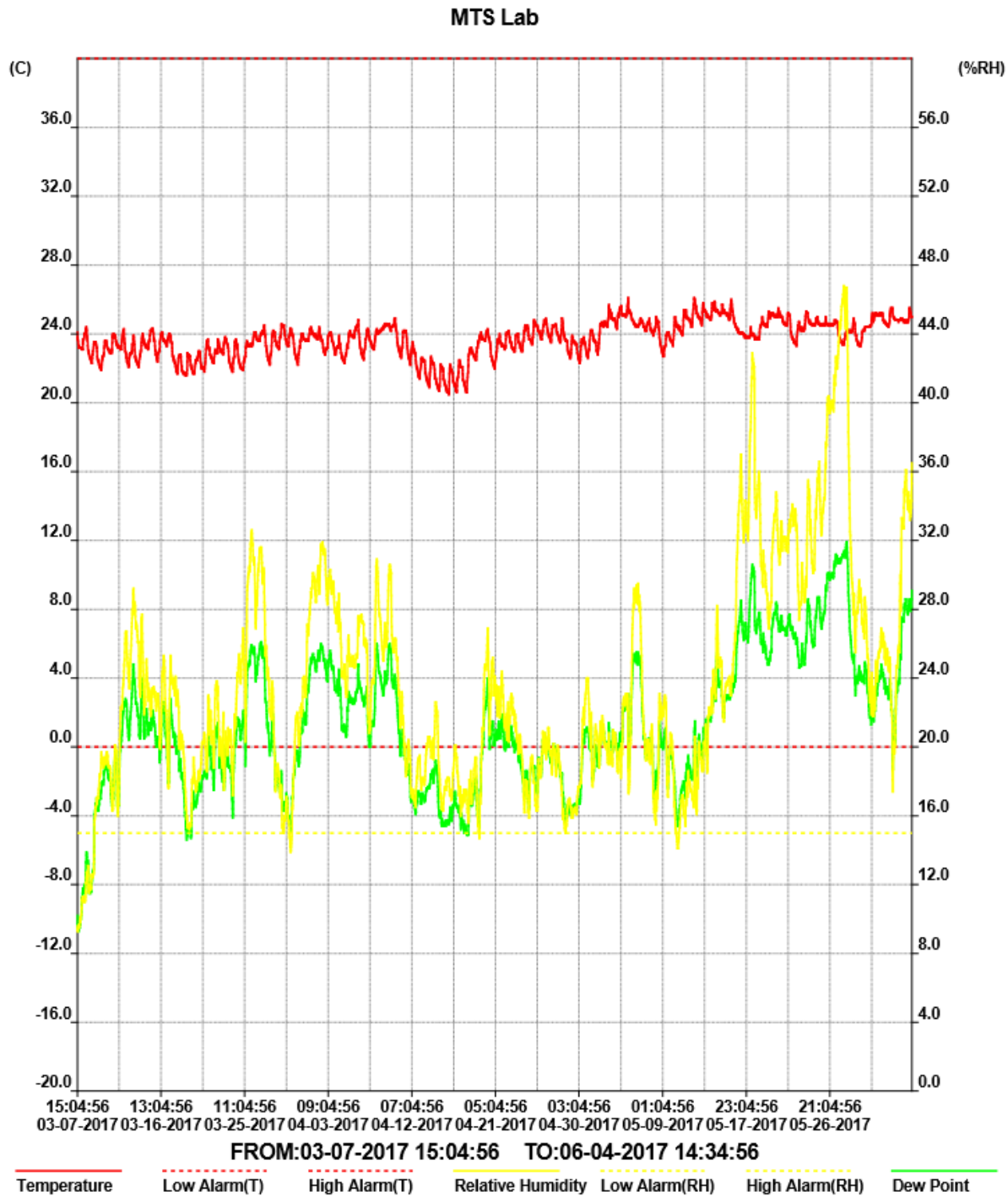

Figure 92: Temperature and humidity throughout the fatigue testing period.